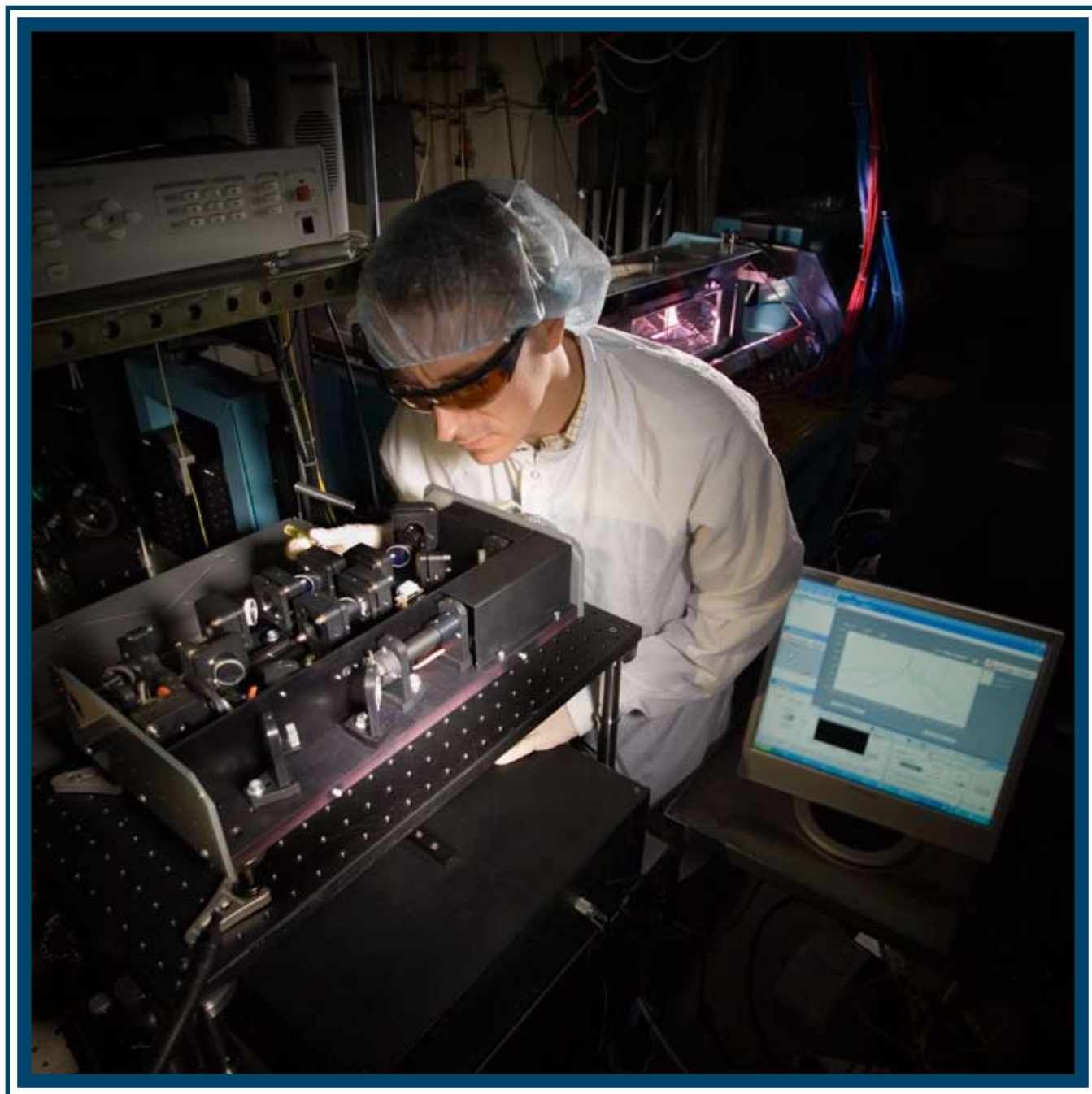


# LLE Review



## Quarterly Report



## About the Cover:

The nonlinear scanning cross-correlator is the main instrument used to measure the temporal contrast of the laser pulse in the Multi-Terawatt (MTW) Laser Facility at the Laboratory for Laser Energetics (see “Pump-Induced Temporal Contrast Degradation in Optical Parametric Chirped-Pulse Amplification: Analysis and Experiment” on p. 135). The cross-correlator is being aligned by LLE Scientist Christophe Dorrer. A cross-correlation between the  $1\omega$  pulse under test and a frequency-doubled  $2\omega$  pulse is obtained after the recombined pulses pass through a frequency-tripling crystal. The energy of the  $3\omega$  pulse measured as a function of the delay between the  $1\omega$  and  $2\omega$  pulses is a representation of the intensity of the pulse under test. Third-order-scanning cross-correlations of the optical parametric chirped-pulse–amplifier (OPCPA) output pulse are seen on the adjacent computer screen. This diagnostic is used to study and improve the temporal contrast of the MTW Laser Facility. The influence of the pump-intensity noise on the temporal contrast of the OPCPA pulses has been experimentally shown and reduced by using a newly demonstrated pump-filtering architecture. The glass-slab amplifier used for high-energy full-system shots is illuminated in the background.



The entire MTW Laser Facility is depicted from both ends of the system. The photo on the left shows the seed laser and grating-based pulse stretcher enclosed with clear plastic. The pump laser and OPCPA are located beyond Laboratory Engineer Jay Brown, who is adjusting controls. The right-hand photo shows the open-vacuum grating compressor chamber (to the left) and the target chamber (to the right). Jay Brown positions the lead shielding used to protect an adjacent area from high-energy x rays produced during some target shots. Research Engineer Ildar Begishev is shown working in the background in both photographs. Starting with a 1-nJ seed pulse, a full-system shot routinely produces 5-J, subpicosecond pulses with a high-order super-Gaussian square spatial profile on a 20-min shot cycle.

This report was prepared as an account of work conducted by the Laboratory for Laser Energetics and sponsored by New York State Energy Research and Development Authority, the University of Rochester, the U.S. Department of Energy, and other agencies. Neither the above named sponsors, nor any of their employees, makes any warranty, expressed or implied, or assumes any legal liability or responsibility for the accuracy, completeness, or usefulness of any information, apparatus, product, or process disclosed, or represents that its use would not infringe privately owned rights. Reference herein to any specific commercial product, process, or service by trade name, mark, manufacturer, or otherwise, does not necessarily con-

stitute or imply its endorsement, recommendation, or favoring by the United States Government or any agency thereof or any other sponsor. Results reported in the LLE Review should not be taken as necessarily final results as they represent active research. The views and opinions of authors expressed herein do not necessarily state or reflect those of any of the above sponsoring entities.

The work described in this volume includes current research at the Laboratory for Laser Energetics, which is supported by New York State Energy Research and Development Authority, the University of Rochester, the U.S. Department of Energy Office of Inertial Confinement Fusion under Cooperative Agreement No. DE-FC03-92SF19460, and other agencies.

For questions or comments, contact Tanya Z. Kosc, Editor, Laboratory for Laser Energetics, 250 East River Road, Rochester, NY 14623-1299, (585) 273-3185.

Worldwide-Web Home Page: <http://www.lle.rochester.edu/>

Printed in the United States of America

Available from

National Technical Information Services

U.S. Department of Commerce

5285 Port Royal Road

Springfield, VA 22161

Price codes: Printed Copy A04

Microfiche A01

# LLE Review

## Quarterly Report



### Contents

In Brief .....	iii
Pump-Induced Temporal Contrast Degradation in Optical Parametric Chirped-Pulse Amplification: Analysis and Experiment .....	135
Dual Nuclear Product Observations of Shock Collapse in Inertial Confinement Fusion .....	148
Equation-of-State Measurements in Ta <sub>2</sub> O <sub>5</sub> Aerogel .....	154
EXAFS Measurements of Quasi-Isentropically Compressed Vanadium Targets on the OMEGA Laser .....	167
The Effect of Resonance Absorption in OMEGA Direct-Drive Designs and Experiments .....	179
Diagnosing Direct-Drive, Shock-Heated, and Compressed Plastic Planar Foils with Noncollective Spectrally Resolved X-Ray Scattering .....	191
Publications and Conference Presentations	



## In Brief

This volume of the LLE Review, covering April–June 2007, features “Pump-Induced Temporal Contrast Degradation in Optical Parametric Chirped-Pulse Amplification: Analysis and Experiment,” by C. Dorrer, A. V. Okishev, I. A. Begishev, and J. D. Zuegel along with V. I. Smirnov (OptiGrate) and L. B. Glebov (College of Optics and Photonics/CREOL, University of Central Florida). In optical parametric chirped-pulse amplification (OPCPA) systems, the temporal fluctuations of the pump pulse are coupled to the spectrum of the chirped signal by the instantaneous parametric gain and lead to a reduction in the temporal contrast of the recompressed amplified signal (p. 135). The authors derive equations describing the contrast degradation in an OPCPA system due to the pump-amplified spontaneous emission. They also quantify the reduction of the contrast in the amplified pulse both analytically and via simulations for an OPCPA system. The placement of a Bragg grating in the regenerative amplifier produces a simple and an efficient pump-intensity reduction, demonstrating contrast improvements up to 30 dB.

Additional highlights of research presented in this issue include the following:

- J. R. Rygg, J. A. Frenje, C. K. Li, F. H. Séguin, and R. D. Petrasso (Plasma Science and Fusion Center, Massachusetts Institute of Technology) along with J. A. Delettrez, D. D. Meyerhofer, and C. Stoeckl discuss the observations of the collapse of strong convergent shocks at the center of spherical capsules filled with D<sub>2</sub> and <sup>3</sup>He gas, which induces both D-D and D-<sup>3</sup>He nuclear production (p. 148). Temporal and spectral measurements of products from both reactions verify data reliability and allow efficient and insightful alterations in ICF simulations.
- J. E. Miller, T. R. Boehly, and D. D. Meyerhofer, along with J. H. Eggert, S. C. Wilks, J. H. Satcher, and J. F. Poco (LLNL) present work on equation-of-state measurements in Ta<sub>2</sub>O<sub>5</sub> aerogel (p. 154). Highly porous samples of tantalum pentoxide (Ta<sub>2</sub>O<sub>5</sub>) aerogel were compressed from initial densities of 0.1, 0.15, and 0.25 g/cm<sup>3</sup> by shock waves with strengths between 0.3 and 3 Mbar. A comparison of the compression measurements and an available high-energy-density equation-of-state (HED-EOS) model found that the model underestimates the level of compression achieved by shock loading below a Mbar. The thermal measurements also indicate less-significant heating than models predict.
- B. Yaakobi, T. R. Boehly, T. C. Sangster, and D. D. Meyerhofer, along with B. A. Remington, P. G. Allen, S. M. Pollaine, H. E. Lorenzana, K. T. Lorenz, and J. A. Hawreliak (LLNL) discuss EXAFS (extended x-ray absorption fine structure) measurements used to determine the temperature and compression in a vanadium sample quasi-isentropically compressed to pressures of up to ~0.75 Mbar (p. 167). VISAR (velocity interferometer system for any reflector) measurements, with aluminum substituting for the vanadium, are used to calibrate the drive pressure. The experimental results obtained by EXAFS and VISAR agree with each other and with the simulations of a hydrodynamic code. The role of a shield to protect the sample from impact heating and the role of radiation heating from the imploding target and the laser-absorption region are also studied.
- I. V. Igumenshchev, V. N. Goncharov, W. Seka, D. Edgell, and T. R. Boehly report on the effect of resonance absorption in OMEGA direct-drive designs and experiments (p. 179). Simulations demonstrate an important contribution of the resonance absorption during both the short laser picket (~100 ps) and

the first 200 to 300 ps in the long laser pulse. Planar reflection light experiments on OMEGA were conducted to validate the theoretical results.

- H. Sawada, S. P. Regan, D. D. Meyerhofer, I. V. Igumenshchev, V. N. Goncharov, T. R. Boehly, R. Epstein, T. C. Sangster, V. A. Smalyuk, and B. Yaakobi, along with G. Gregori (Rutherford Appleton Laboratory and Clarendon Laboratory, University of Oxford) and S. H. Glenzer and O. L. Landen (LLNL) present the diagnosing of direct-drive, shock-heated, and compressed plastic planar foils with noncollective spectrally resolved x-ray scattering (p. 191). Plastic (CH) and Br-doped CH foils were driven with six beams, having an overlapped intensity of  $\sim 1 \times 10^{14}$  W/cm<sup>2</sup> and generating  $\sim 15$ -Mbar pressure in the foil. The uniformly compressed portion of the target was probed with 9.0-keV x rays from a Zn He $_{\alpha}$  backlighter created with 18 additional tightly focused beams. An examination of the scattered x-ray spectra reveals that an upper limit of  $Z \sim 2$  and  $T_e = 20$  eV can be inferred, since low average ionizations (i.e.,  $Z < 2$ ) cannot be accurately diagnosed in this experiment.

Tanya Z. Kosci  
*Editor*

---

# Pump-Induced Temporal Contrast Degradation in Optical Parametric Chirped-Pulse Amplification: Analysis and Experiment

## Introduction

Laser–matter interactions in new regimes have occurred due to the generation of high-intensity optical pulses using large-scale laser systems.<sup>1</sup> The interaction regime of a laser pulse with a target is basically set by the peak intensity of the pulse, which is fundamentally proportional to the ratio of the pulse energy to the duration of the pulse and surface of the focal spot. Intensities of the order of  $10^{22}$  W/cm<sup>2</sup> have been claimed,<sup>2</sup> and facilities delivering high-energy, high-intensity laser pulses are under operation or construction.<sup>3</sup> The interaction can be detrimentally impacted by light present before the main pulse since absorbed light can lead to physical modification of the target.<sup>4</sup> The temporal contrast of a laser pulse is the ratio of the peak power of the main pulse to the power of the light in some predetermined temporal range before the main pulse. The contrast can be reduced significantly during the generation and amplification of laser pulses, and contrast degradation manifests itself as isolated prepulses or as a slowly varying pedestal. Incoherent laser and parametric fluorescence can significantly impact the contrast of laser pulses and can lead to a long-range pedestal on the recompressed pulse.<sup>4,5</sup> This contrast degradation is fundamental since fluorescence is always present for classical optical amplifiers. The contrast of optical parametric chirped-pulse amplifiers, however, is also detrimentally impacted by temporal variations of the intensity of the pump pulse that induce spectral variations on the stretched amplified signal via the instantaneous parametric gain. This is a practical limitation that can be eliminated or reduced by proper design of the pump pulse and the optical parametric chirped-pulse amplification (OPCPA) system.

The parametric gain induced by a pump pulse in a nonlinear crystal is an efficient process for large-bandwidth, high-energy amplification of chirped optical pulses.<sup>6–8</sup> It is used in stand-alone systems<sup>9–16</sup> or as the front end of large-scale laser facilities.<sup>17</sup> The impact of temporal fluctuations on the contrast of the recompressed signal in an OPCPA system was first identified by Forget *et al.*<sup>18</sup> Simulations of the effect of pump-pulse amplified spontaneous emission (ASE) on an OPCPA system have linked the ASE coherence time to the

temporal extent of the induced pedestal.<sup>19</sup> These publications offer a physical explanation of pump-induced contrast degradation, but an analytical treatment is necessary to quantify the impact of this phenomenon, improve the contrast of existing systems, and design new high-contrast OPCPA systems. This article quantifies the impact of incoherent pump-pulse ASE using an analytic formalism for pump-induced temporal contrast degradation in OPCPA systems and presents an experimental solution to reduce this impact. The impact of incoherent pump ASE is analytically quantified as a function of the operating regime of the OPCPA system. The following sections (1) present the necessary formalism and derive general equations describing the pump-induced contrast degradation in OPCPA systems; (2) compare these analytical derivations with simulations, bringing to light the magnitude of these effects in a typical OPCPA system; and (3) describe an LLE experiment that demonstrates the reduction of pump-induced temporal contrast degradation by filtering the pump pulse with a volume Bragg grating (VBG) in a regenerative amplifier.

## Analysis of Pump-Induced Contrast Degradation in an OPCPA System

### 1. General Approach

The derivations presented in this section assume a one-dimensional representation of the electric field of the signal and pump as a function of time (and equivalently optical frequency), without spatial resolution. Such a model is sufficient to introduce the various aspects of contrast degradation in OPCPA systems. Some of these systems use flattop pumps and signals, in which case the temporal contrast is mostly limited by the contrast obtained in the constant-intensity portion of the beam. For high energy extraction, efficient phase matching, and optimal beam quality, OPCPA systems are usually run in configurations where spatial walk-off and diffraction are not significant. An instantaneous transfer function between the intensity of the pump, the intensity of the input signal, and the intensity of the output signal is used to describe the parametric amplifier. This applies to an amplifier where temporal walk-off and dispersion-induced changes in the intensity of the interacting waves are small compared to the time scales of the

temporal variations of the signal and pump. This also applies to a sequence of amplifiers where scaled versions of the same pump are used in each amplifier with an identical relative delay between the signal being amplified and the pump. Figure 111.1 presents a schematic of an OPCPA system. The short input signal is stretched by a stretcher, amplified by the pump pulse in an optical parametric amplifier (one or several nonlinear crystals properly phase matched), and recompressed. As identified in Refs. 18 and 19, the variations of the parametric gain due to variations in the pump intensity lead to modulations of the temporal intensity of the amplified stretched pulse, which are equivalent to modulations of the spectrum of this pulse. These modulations lead to contrast-reducing temporal features after recompression.

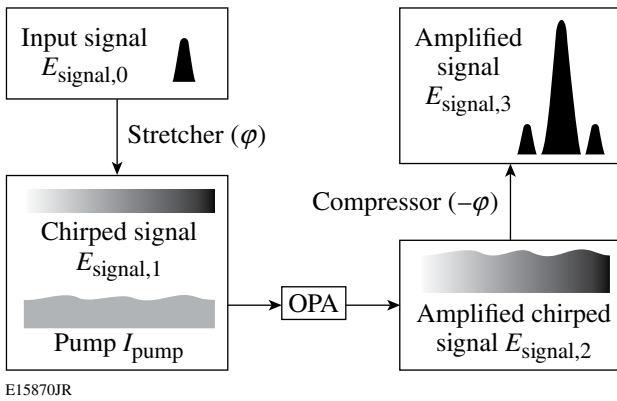


Figure 111.1  
Schematic of an OPCPA system. Pump-intensity modulation gets transferred onto the spectrum of the chirped signal in an optical parametric amplifier (OPA). The modulation of the spectrum of the recompressed signal induces contrast-reducing temporal features on the recompressed signal.

## 2. Contrast Degradation of an OPCPA System in the Presence of Pump Noise

In this article,  $E$  and  $\tilde{E}$  relate to the temporal and spectral representations of the analytic signal of an electric field, and  $I$  and  $\tilde{I}$  relate to the corresponding intensities. The initial signal is described by the spectral field  $\tilde{E}_{\text{signal},0}(\omega)$ . After stretching with second-order dispersion  $\varphi$ , the stretched pulse is described in the time domain by

$$E_{\text{signal},1}(t) = (1/\sqrt{\varphi})\tilde{E}_{\text{signal},0}(t/\varphi)\exp(-it^2/2\varphi)$$

up to some multiplicative constants. The quadratic phase describes the one-to-one correspondence between time and optical frequency in the highly stretched pulse, which is symbolically written as  $t = \varphi\omega$ . The temporal intensity of the signal after parametric amplification is a function of the temporal

intensity of the stretched signal  $I_{\text{signal},1}(t) = (1/\varphi)\tilde{I}_{\text{signal},0}(t/\varphi)$  and the temporal intensity of the pump  $I_{\text{pump}}(t)$ , which can be written as

$$I_{\text{signal},2}(t) = f[I_{\text{signal},1}(t), I_{\text{pump}}(t)]. \quad (1)$$

The function  $f$  depends on the parametric amplifier length and nonlinear coefficient.

Figure 111.2 displays two examples of behavior of the function  $f$  for a given input signal intensity, namely the relation between the output signal intensity and the pump intensity. In Fig. 111.2(a), the amplifier is unsaturated, and there is a linear relation between variations of the pump intensity and variations of the amplified signal intensity around point A. In Fig. 111.2(b), the amplifier is saturated. The output signal intensity reaches a local maximum, and there is a quadratic relation between variations of the pump intensity and variations of the amplified signal intensity around point B. Assuming that the intensity modulation of the pump does not significantly modify the instantaneous frequency of the chirped signal, the intensity of a spectral component of the amplified signal at the optical frequency  $\omega$  is

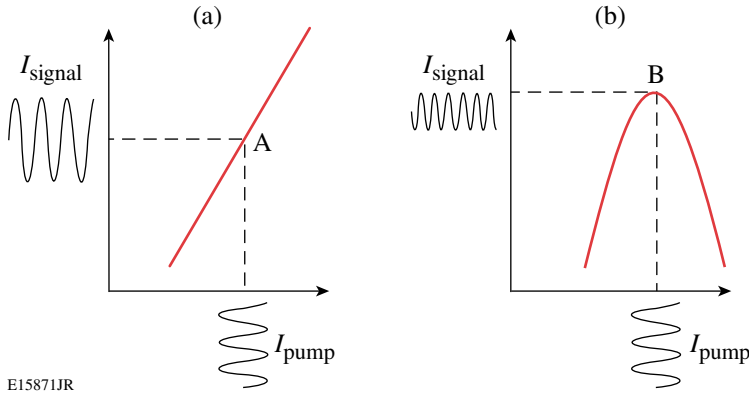
$$f[I_{\text{signal},1}(\varphi\omega), I_{\text{pump}}(\varphi\omega)] = f[\tilde{I}_{\text{signal},0}(\omega)/\varphi, I_{\text{pump}}(\varphi\omega)].$$

The pump-intensity noise  $\delta I_{\text{pump}}(t)$  is introduced by writing the intensity as  $I_{\text{pump}}(t) = I_{\text{pump}}^{(0)}(t) + \delta I_{\text{pump}}(t)$ . Assuming the amplifier is not saturated [Fig. 111.2(a)], the function  $f$  is developed to first order around the operating point set by  $I_{\text{pump}}^{(0)}$  as

$$\begin{aligned} & f[\tilde{I}_{\text{signal},0}(\omega)/\varphi, I_{\text{pump}}(\varphi\omega)] \\ &= f[\tilde{I}_{\text{signal},0}(\omega)/\varphi, I_{\text{pump}}^{(0)}(\varphi\omega)] \\ &+ \delta I_{\text{pump}}(\varphi\omega) \frac{\partial f}{\partial I_{\text{pump}}} [\tilde{I}_{\text{signal},0}(\omega)/\varphi, I_{\text{pump}}^{(0)}(\varphi\omega)]. \quad (2) \end{aligned}$$

The spectral intensity of the amplified recompressed signal is

$$\tilde{I}_{\text{signal},3}(\omega) = \varphi f[\tilde{I}_{\text{signal},0}(\omega)/\varphi, I_{\text{pump}}(\varphi\omega)].$$



E15871JR

Figure 111.2

Representation of the transfer function between output signal intensity and pump intensity around the operating point of a parametric amplifier in the (a) unsaturated and (b) saturated regimes. At point A, there is a linear relation between pump-intensity modulation and amplified-signal-intensity modulation. At point B, there is a quadratic relation between pump-intensity modulation and amplified-signal-intensity modulation.

and one can define

$$\tilde{I}_{\text{signal},3}^{(0)}(\omega) = \varphi f \left[ \tilde{I}_{\text{signal},0}(\omega) / \varphi, I_{\text{pump}}^0(\varphi\omega) \right]$$

as the spectral intensity of the signal amplified by a noiseless pump. The partial derivative of  $f$  with respect to the pump intensity is assumed to be independent of the signal intensity, and one defines the constant

$$f_{(1)} = \frac{\partial f}{\partial I_{\text{pump}}} \left[ \tilde{I}_{\text{signal},0}(\omega) / \varphi, I_{\text{pump}}^0(\varphi\omega) \right].$$

For a compressor matched to the stretcher up to a residual spectral phase  $\varphi_{\text{residual}}(\omega)$ , the electric field of the recompressed signal is simply

$$\begin{aligned} \tilde{E}_{\text{signal},3}(\omega) &= \sqrt{\tilde{I}_{\text{signal},3}^{(0)}(\omega) + \varphi f_{(1)} \delta I_{\text{pump}}(\varphi\omega)} \\ &\times \exp[i\varphi_{\text{residual}}(\omega)]. \end{aligned} \quad (3)$$

A first-order development of Eq. (3) gives a spectral representation of the signal:

$$\begin{aligned} \tilde{E}_{\text{signal},3}(\omega) &= \sqrt{\tilde{I}_{\text{signal},3}^{(0)}(\omega) \exp[i\varphi_{\text{residual}}(\omega)]} \\ &\times \left[ 1 + \frac{\varphi f_{(1)} \delta I_{\text{pump}}(\varphi\omega)}{2\tilde{I}_{\text{signal},3}^{(0)}(\omega)} \right]. \end{aligned} \quad (4)$$

One can define

$$\tilde{E}_{\text{signal},3}^{(0)}(\omega) = \sqrt{\tilde{I}_{\text{signal},3}^{(0)}(\omega) \exp[i\varphi_{\text{residual}}(\omega)]}$$

as the electric field of the recompressed signal in the absence of noise. In the OPCPA process, the spectral density of the amplified signal is usually approximately constant (or slowly varying) because of saturation effects, so that  $\tilde{I}_{\text{signal},3}^{(0)}(\omega)$  is replaced by  $\varphi I_{\text{signal},2}$  in the denominator of Eq. (4). This leads to

$$\tilde{E}_{\text{signal},3}(\omega) = \tilde{E}_{\text{signal},3}^{(0)}(\omega) \left[ 1 + \frac{f_{(1)} \delta I_{\text{pump}}(\varphi\omega)}{2I_{\text{signal},2}} \right]. \quad (5)$$

The Fourier transform of Eq. (5) gives the electric field in the temporal domain:

$$\begin{aligned} E_{\text{signal},3}(t) &= E_{\text{signal},3}^{(0)}(t) + \frac{f_{(1)}}{2I_{\text{signal},2}\varphi} \\ &\times E_{\text{signal},3}^{(0)}(t) \otimes \delta \tilde{I}_{\text{pump}}(t/\varphi). \end{aligned} \quad (6)$$

Further simplification stems from defining

$$f_{(1,N)} = f_{(1)} I_{\text{pump}}^{(0)} / I_{\text{signal},2},$$

which is the change in intensity of the amplified signal normalized to the intensity of the amplified signal for a change in the pump intensity normalized to the pump intensity. The field of

the recompressed signal is

$$E_{\text{signal},3}(t) = E_{\text{signal},3}^{(0)}(t) + \frac{f_{(1,N)}}{2\varphi I_{\text{pump}}^{(0)}} \times E_{\text{signal},3}^{(0)}(t) \otimes \delta \tilde{I}_{\text{pump}}(t/\varphi), \quad (7)$$

and the intensity of the compressed signal is

$$I_{\text{signal},3}(t) = I_{\text{signal},3}^{(0)}(t) + \frac{f_{(1,N)}^2}{4[\varphi I_{\text{pump}}^{(0)}]^2} \times \left| E_{\text{signal},3}^{(0)}(t) \otimes \delta \tilde{I}_{\text{pump}}(t/\varphi) \right|^2, \quad (8)$$

using the fact that the first term in the right-hand side of Eq. (7) is a short pulse while the second term describes the contrast reduction over a large temporal range.

When the amplifier is saturated [Fig. 111.2(b)],  $f_{(1)} = 0$  and Eq. (2) must be replaced by the second-order decomposition of  $f$ , which is

$$\begin{aligned} & f\left[\tilde{I}_{\text{signal},0}(\omega)/\varphi, I_{\text{pump}}(\varphi\omega)\right] \\ &= f\left[\tilde{I}_{\text{signal},0}(\omega)/\varphi, I_{\text{pump}}^{(0)}(\varphi\omega)\right] \\ &+ \frac{1}{2}\left[\delta I_{\text{pump}}(\varphi\omega)\right]^2 \\ &\times \frac{\partial^2 f}{\partial I_{\text{pump}}^2}\left[\tilde{I}_{\text{signal},0}(\omega)/\varphi, I_{\text{pump}}^{(0)}(\varphi\omega)\right]. \end{aligned} \quad (9)$$

Assuming that the second-order derivative of  $f$  with respect to the pump intensity does not depend on the signal intensity, one defines

$$f_{(2)} = \partial^2 f / \partial I_{\text{pump}}^2 \left[ \tilde{I}_{\text{signal},0}(\omega) / \varphi, I_{\text{pump}}^{(0)}(\varphi\omega) \right].$$

Replacing  $\tilde{I}_{\text{signal},3}^{(0)}$  by  $\varphi I_{\text{signal},2}$ , one obtains

$$\tilde{E}_{\text{signal},3}(\omega) = \tilde{E}_{\text{signal},3}^{(0)}(\omega) \left[ 1 + \frac{f_{(2)} \delta I_{\text{pump}}^2(\varphi\omega)}{4I_{\text{signal},2}} \right]. \quad (10)$$

The Fourier transform of Eq. (10) gives the temporal field of the recompressed signal:

$$E_{\text{signal},3}(t) = E_{\text{signal},3}^{(0)}(t) + \frac{f_{(2,N)}}{4[\varphi I_{\text{pump}}^{(0)}]^2} E_{\text{signal},3}^{(0)}(t) \otimes \delta \tilde{I}_{\text{pump}}(t/\varphi) \otimes \delta \tilde{I}_{\text{pump}}(t/\varphi), \quad (11)$$

where  $f_{(2,N)} = f_{(2)} [I_{\text{pump}}^{(0)}]^2 / I_{\text{signal},2}$  is the normalized change in the amplified signal intensity for a normalized change in the pump intensity. Finally, the intensity of the recompressed signal is

$$I_{\text{signal},3}(t) = I_{\text{signal},3}^{(0)}(t) + \frac{f_{(2,N)}^2}{16[\varphi I_{\text{pump}}^{(0)}]^4} \times \left| E_{\text{signal},3}^{(0)}(t) \otimes \delta \tilde{I}_{\text{pump}}(t/\varphi) \otimes \delta \tilde{I}_{\text{pump}}(t/\varphi) \right|^2. \quad (12)$$

Equations (8) and (12) are general expressions linking the variations in pump intensity to the intensity of the recompressed pulse in the two practically relevant cases:  $f_{(1)} \neq 0$  describes the linear modulation regime, with a linear relation between the pump intensity and the amplified stretched signal intensity around the operating point;  $f_{(1)} = 0, f_{(2)} \neq 0$  describe the quadratic modulation regime, with a quadratic relation between the pump intensity and the amplified stretched signal intensity around the operating point. In the next two subsections these general expressions are evaluated when ASE is present on the pump pulse.

### 3. Contrast Degradation of an OPCPA System in the Linear-Modulation Regime due to the Pump-Pulse ASE

The pump-pulse ASE is described as an additive stationary process  $E_{\text{ASE}}$ , and the field of the pump pulse is

$$E_{\text{pump}}(t) = E_{\text{pump}}^{(0)}(t) + E_{\text{ASE}}(t). \quad (13)$$

One has at first order

$$I_{\text{pump}}(t) = I_{\text{pump}}^{(0)}(t) + E_{\text{pump}}^{(0)}(t)E_{\text{ASE}}^*(t) + E_{\text{pump}}^{(0)*}(t)E_{\text{ASE}}(t),$$

which allows one to identify

$$\delta I_{\text{pump}}(t) = E_{\text{pump}}^{(0)}(t)E_{\text{ASE}}^*(t) + E_{\text{pump}}^{(0)*}(t)E_{\text{ASE}}(t).$$

One can use the simplification

$$E_{\text{pump}}^{(0)}(t) = E_{\text{pump}}^{(0)*}(t) = \sqrt{I_{\text{pump}}^{(0)}}$$

over the interval  $[0, T]$ , where the pump has significant intensity, and set the ASE electric field to 0 outside the interval  $[0, T]$ . The electric field of one realization of the ASE restricted to the interval  $[0, T]$  and its Fourier transform are noted  $E_{\text{ASE}, T}$  and  $\tilde{E}_{\text{ASE}, T}$ , respectively. One obtains

$$\delta \tilde{I}_{\text{pump}}(\omega) = \sqrt{I_{\text{pump}}^{(0)}} \left[ \tilde{E}_{\text{ASE}, T}(\omega) + \tilde{E}_{\text{ASE}, T}^*(-\omega) \right]. \quad (14)$$

In the linear modulation regime, the calculation of the intensity of the recompressed pulse using this expression and Eq. (8) leads to

$$I_{\text{signal}, 3}(t) = I_{\text{signal}, 3}^{(0)}(t) + \frac{f_{(1, N)}^2}{4\epsilon_{\text{pump}}} \int I_{\text{signal}, 3}^{(0)}(t - \phi\omega') \times \left[ \tilde{I}_{\text{ASE}, T}(\omega') + \tilde{I}_{\text{ASE}, T}(-\omega') \right] d\omega', \quad (15)$$

where  $\epsilon_{\text{pump}}$  is the energy of the pump pulse. The pump-induced pedestal is therefore given by a convolution of the symmetrized spectrum of the ASE present on the pump pulse with the recompressed pulse intensity. The intensity of the pedestal is proportional to  $f_{(1, N)}^2$ . Proper spectral filtering of the pump pulse reduces the temporal extent of the induced pedestal. In the usual case where the recompressed pulse is significantly shorter than the temporal variations of the induced pedestal, Eq. (15) can be simplified as

$$I_{\text{signal}, 3}(t) = I_{\text{signal}, 3}^{(0)}(t) + \frac{f_{(1, N)}^2 \epsilon_{\text{signal}}^{(0)}}{4\phi\epsilon_{\text{pump}}} \times \left[ \tilde{I}_{\text{ASE}, T}(t/\phi) + \tilde{I}_{\text{ASE}, T}(-t/\phi) \right]. \quad (16)$$

The pedestal due to the ASE present on the pump pulse is therefore directly given by a symmetrized version of the spectrum of the ASE present on the pump pulse. The symmetrized spectrum of the ASE is spread in time proportionally to the second-order dispersion of the chirped pulse. Integration of Eq. (15) gives

$$\epsilon_{\text{signal}} = \epsilon_{\text{signal}}^{(0)} \left[ 1 + f_{(1, N)}^2 \epsilon_{\text{ASE}, T} / 2\epsilon_{\text{pump}} \right],$$

which allows the energy in the pedestal  $\epsilon_{\text{pedestal}}$  normalized to the energy of the signal  $\epsilon_{\text{signal}}^{(0)}$  to be expressed as

$$\frac{\epsilon_{\text{pedestal}}}{\epsilon_{\text{signal}}^{(0)}} = \frac{f_{(1, N)}^2 \epsilon_{\text{ASE}, T}}{2 \epsilon_{\text{pump}}}. \quad (17)$$

The ratio of the pedestal energy to the signal energy,

$$\epsilon_{\text{pedestal}} / \epsilon_{\text{signal}}^{(0)},$$

is directly proportional to the ratio of the energy of the ASE in the temporal range defined by the pump to the energy of the pump. The ratio  $\epsilon_{\text{ASE}, T} / \epsilon_{\text{pump}}$  is called ‘‘fractional ASE energy’’ in the remainder of this article.

#### 4. Contrast Degradation of an OPCPA System in the Quadratic-Modulation Regime due to the Pump ASE

The intensity of the recompressed pulse for an OPCPA system in the quadratic-modulation regime with ASE present on the pump can be calculated using Eqs. (12) and (14):

$$I_{\text{signal}, 3}(t) = I_{\text{signal}, 3}^{(0)}(t) + \frac{f_{(2, N)}^2}{8(\phi\epsilon_{\text{pump}})^2} I_{\text{signal}, 3}^{(0)}(t) \otimes \left[ \tilde{I}_{\text{ASE}, T}(t/\phi) + \tilde{I}_{\text{ASE}, T}(-t/\phi) \right] \otimes \left[ \tilde{I}_{\text{ASE}, T}(t/\phi) + \tilde{I}_{\text{ASE}, T}(-t/\phi) \right]. \quad (18)$$

Equation (18) shows that the pedestal is given by the double convolution of the symmetrized spectrum of the pump ASE

with the recompressed signal in the absence of pump ASE. The convolution of the symmetrized spectrum of ASE with itself is broader than the spectrum of ASE (e.g., by a factor  $\sqrt{2}$  for a Gaussian spectrum). Therefore, the temporal extent of the pedestal is larger than in the linear-modulation regime. In the case where the intensity of the recompressed signal is short compared to the temporal variations of the pedestal, Eq. (18) can be simplified into

$$I_{\text{signal},3}(t) = I_{\text{signal},3}^{(0)} + \frac{f_{(2,N)}^2 \epsilon_{\text{signal}}^{(0)}}{8\varphi^2 \epsilon_{\text{pump}}^2} \times \left[ \tilde{I}_{\text{ASE},T}(t/\varphi) + \tilde{I}_{\text{ASE},T}(-t/\varphi) \right] \otimes \left[ \tilde{I}_{\text{ASE},T}(t/\varphi) + \tilde{I}_{\text{ASE},T}(-t/\varphi) \right]. \quad (19)$$

Finally, integrating Eq. (18) leads to the energy in the pedestal,

$$\frac{\epsilon_{\text{pedestal}}}{\epsilon_{\text{signal}}^{(0)}} = \frac{f_{(2,N)}^2 \epsilon_{\text{ASE},T}^2}{2\epsilon_{\text{pump}}^2}. \quad (20)$$

In the quadratic-modulation regime, the ratio of the energy of the pedestal to the energy of the signal is proportional to the square of the fractional ASE energy. Comparing Eq. (20) with Eq. (17) leads to the conclusion that if  $\epsilon_{\text{ASE},T}/\epsilon_{\text{pump}} < [f_{(1,N)}/f_{(2,N)}]^2$ , there is less energy in the pedestal when the amplifier is run in the quadratic-modulation regime. Operating the OPCPA in the saturation regime locally decreases the modulation of the output intensity and reduces the total energy of the associated temporal pedestal, provided that the previous inequality is verified.

## Simulations of Pump-Induced Contrast Degradation

### 1. Model Description

Simulations of an OPCPA system with parameters similar to those of the OPCPA preamplifier of LLE's Multi-Terawatt laser<sup>10</sup> and the front end of the OMEGA EP Laser Facility<sup>17</sup> have been performed. The signal has a central wavelength equal to 1053 nm. The case of a flat spectral density has been simulated since it corresponds closely to the derivations performed in the previous section. The case of a Gaussian spectral density with a full width at half maximum (FWHM) equal to 6 nm has also been simulated since it is closer to the actual experimental conditions. The stretcher introduces a dispersion equal to 300 ps/nm, i.e.,  $\varphi = 1.76 \times 10^{22} \text{ s}^2$ . The preamplifier

has two lithium triborate (LBO) crystals cut for type-I phase matching at 1053 nm and 526.5 nm in collinear interaction, i.e.,  $\varphi_{\text{LBO}} = 11.8^\circ$  and  $\theta_{\text{LBO}} = 90^\circ$ , with a total length of 59.5 mm. The OPCPA pump at 526.5 nm is obtained by doubling a pump pulse at 1053 nm in an 11-mm LBO crystal. The pump at 1053 nm is a 20th-order super-Gaussian, with a FWHM equal to 2.6 ns. The intensity of the up-converted pump has been obtained using a Runge–Kutta resolution of the corresponding nonlinear equations. Figure 111.3 displays the normalized intensity of the pump and stretched signal in the OPCPA crystal. The operation of the preamplifier was simulated by solving the system of three equations describing the parametric interaction of the electric field of the signal, idler, and pump using the Runge–Kutta method. No spatial resolution or temporal effects have been introduced, for the reasons expressed at the beginning of the previous section. It is straightforward (although computationally more intensive) to introduce these effects. The phase mismatch between the interacting waves was chosen equal to zero. Figure 111.4 displays the amplified stretched signal intensity as a function of the pump intensity for an input stretched signal intensity of 0.1 W/cm<sup>2</sup>, i.e., the function  $I_{\text{signal},2} = f[I_{\text{signal},1}, I_{\text{pump}}]$  used in the previous section for  $I_{\text{signal},1} = 0.1 \text{ W/cm}^2$ . Points A and B correspond to the linear- and quadratic-modulation regimes, respectively. A fit of the curve plotted in Fig. 111.4 around these two points leads to the values  $f_{(1,N)} = 8$  and  $f_{(2,N)} = 66$ . The next two subsections present the contrast degradation results for a pump with ASE and a signal with constant spectral density followed by results for a pump with ASE and a signal with a Gaussian spectral density. For the sake of clarity, the intensity of the recompressed signal is plotted only at negative times (i.e., before the peak of the signal), bearing in mind that the pump-induced contrast degradation is symmetric.

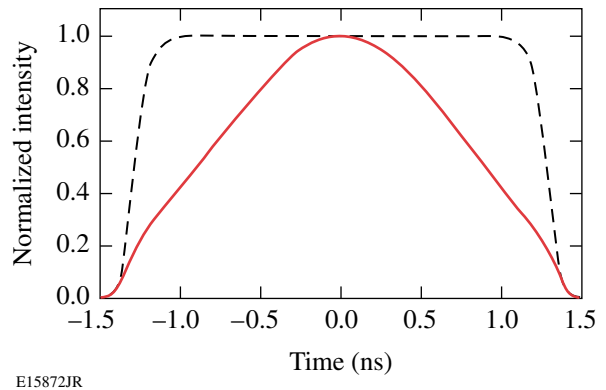


Figure 111.3  
Normalized intensity of the chirped Gaussian signal (solid curve) and pump (dashed curve) in the OPCPA system.

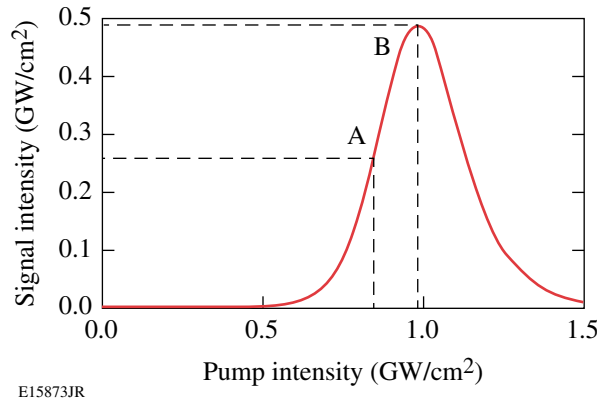


Figure 111.4  
Transfer function of the OPCPA preamplifier for a signal intensity equal to  $0.1 \text{ W/cm}^2$ . Points A and B identify the linear and quadratic regimes of operation, respectively.

## 2. Pump with ASE and Signal with Flat Spectral Density

In this section, the stretched signal has a flat spectral density and an intensity of  $0.1 \text{ W/cm}^2$ . The pump ASE spectrum is assumed Gaussian and centered at the wavelength of the pump pulse. The FWHM of the spectrum is chosen equal to either  $0.14 \text{ nm}$  (which was experimentally measured on the Nd:YLF regenerative amplifier used to generate the pump pulse) or  $0.03 \text{ nm}$  (which corresponds to a hypothetical pump spectral bandpass filtering). Figure 111.5 displays close-ups of the simulated intensity of the pump for an ASE bandwidth of  $0.14 \text{ nm}$  and  $0.03 \text{ nm}$  at various fractional ASE energies  $\varepsilon_{\text{ASE},T}/\varepsilon_{\text{pump}}$ . The homodyne beating of the electric field of the ASE with the electric field of the pump leads to significant pump intensity modulation even at low ASE energy levels. Figure 111.6 displays a comparison of the results of the simulation with the analytical results for the  $0.14\text{-nm}$  bandwidth. The OPCPA is run either in the linear modulation regime [Figs. 111.6(a)–111.6(c)] or in the quadratic-modulation regime [Figs. 111.6(d)–111.6(f)]. The fractional ASE energy is specified as  $10^{-5}$ ,  $10^{-4}$ , and  $10^{-3}$ . Significant pedestal levels are observed, even for relatively low pump intensity modulation, indicating that such contrast degradation can severely limit OPCPA systems, or laser systems that include an OPCPA as one of their amplifiers. Good agreement of the simulations with the analytical predictions is obtained. Discrepancy in the quadratic modulation regime at low fractional ASE energies is attributed to the leading and the falling edge of the pump, for which the amplification process is in the linear regime. The pedestal due to the pump ASE extends at longer times in the case of quadratic modulation, as expected from the double convolution of Eq. (18). The pedestal is typically more intense at short times in the linear regime, and it can also be seen that the total energy in the

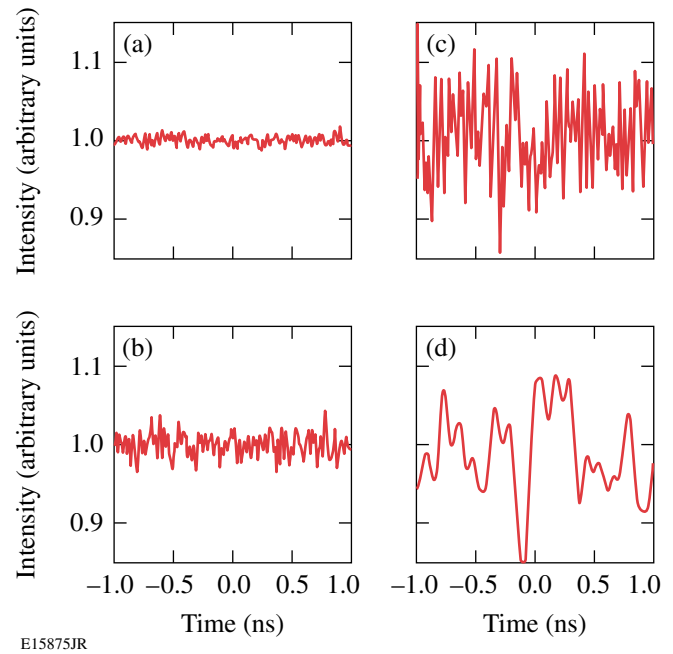


Figure 111.5  
Close-ups of the temporal intensity of the pump for ASE with a Gaussian spectrum with a FWHM equal to  $0.14 \text{ nm}$  and a fractional energy equal to (a)  $10^{-5}$ , (b)  $10^{-4}$ , and (c)  $10^{-3}$ , and (d) for ASE with a Gaussian spectrum with a FWHM equal to  $0.03 \text{ nm}$  and a fractional energy equal to  $10^{-3}$ .

pedestal is smaller in the quadratic modulation regime than in the linear modulation regime {in agreement with the relation  $\varepsilon_{\text{ASE},T}/\varepsilon_{\text{pump}} < [f_{(1,N)}/f_{(2,N)}]^2$ , with  $[f_{(1,N)}/f_{(2,N)}]^2 = 0.014$ }. It should be noted, however, that the two modulation regimes lead to similar pedestal levels around  $-100 \text{ ps}$ . Figures 111.7(a) and 111.7(d) display the intensity of the recompressed signal for an ASE bandwidth of  $0.03 \text{ nm}$  and a fractional ASE energy equal to  $10^{-3}$ , which can be compared to the intensity plotted in Figs. 111.6(c) and 111.6(f). Reduction of the bandwidth of the pump ASE leads to a drastic improvement of the signal temporal contrast. This result shows that a significant increase in the contrast of OPCPA systems can be obtained via proper spectral filtering of the pump pulse, as is discussed in **Experimental Demonstration of Temporal Contrast Improvement of an OPCPA System by Pump Spectral Filtering** (p. 144). While this was expressed previously in terms of the coherence time of the pump ASE,<sup>19</sup> the temporal contrast away from the peak of the signal is influenced mostly by the spectral density of the ASE at optical frequencies significantly different from the central frequency of the pump. A non-zero spectral density at these optical frequencies leads to a finite extinction ratio for the pulse. The coherence time of the ASE describes the variations of the temporal electric field of the ASE due to interference between different optical frequencies in the ASE spectrum.

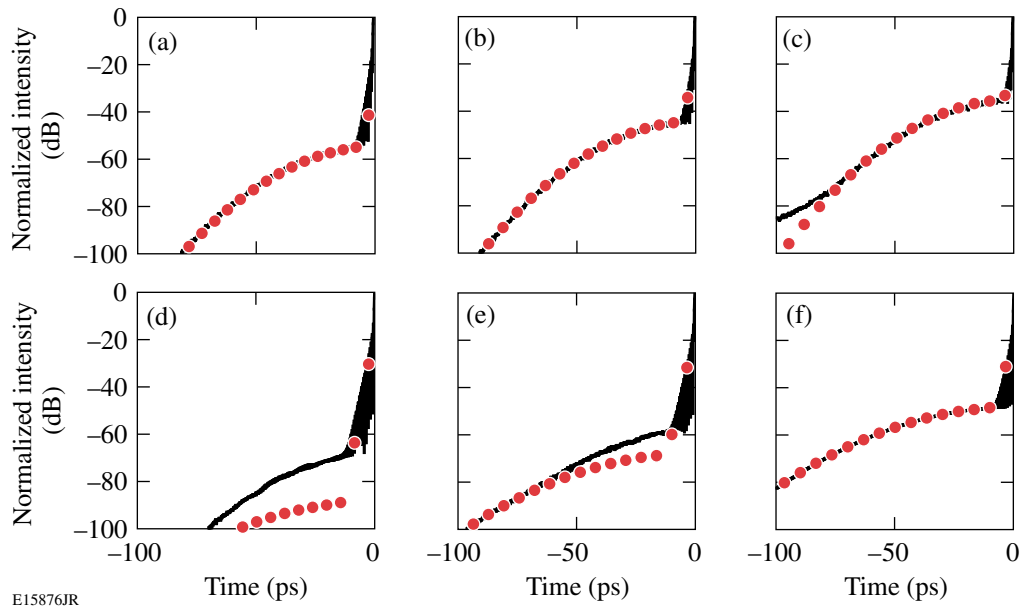


Figure 111.6

Intensity of the recompressed signal for an input signal with a flat spectral density and an ASE Gaussian spectrum with a FWHM equal to 0.14 nm. (a)–(c) correspond to an amplifier run in the linear-modulation regime when the fractional ASE energy is equal to (a)  $10^{-5}$ , (b)  $10^{-4}$ , and (c)  $10^{-3}$ . (d)–(f) correspond to an amplifier run in the quadratic-modulation regime when the fractional ASE energy is equal to (d)  $10^{-5}$ , (e)  $10^{-4}$ , and (f)  $10^{-3}$ . In each case, the simulated intensity is plotted with a continuous line, and the intensity predicted analytically is plotted with solid circles.

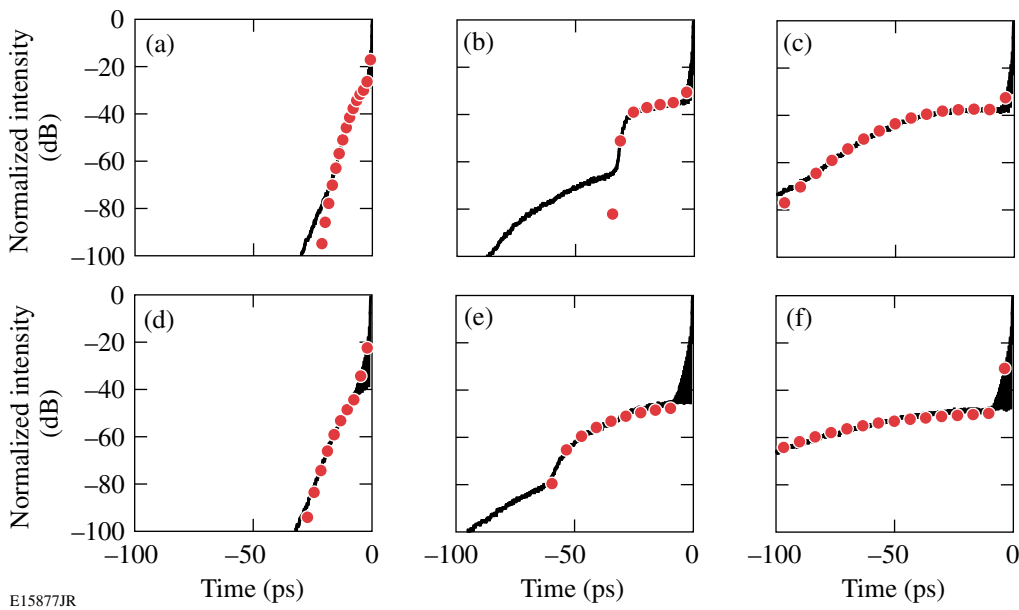


Figure 111.7

Intensity of the recompressed signal for an input signal with a flat spectral density, ASE with various Gaussian spectra, and fractional ASE energy equal to  $10^{-3}$ . (a) and (d) correspond to a FWHM equal to 0.03 nm in the linear and quadratic modulation regimes, respectively. (b) and (e) correspond to a FWHM equal to 0.14 nm filtered by a 0.20-nm FWHM, 20th-order super-Gaussian filter in the linear and quadratic modulation regimes, respectively. (c) and (f) correspond to a FWHM equal to 0.14 nm centered 0.07 nm away from the central wavelength of the pump in the linear and quadratic modulation regimes. In each case, the simulated intensity is plotted with a continuous line, and the intensity predicted analytically is plotted with solid circles.

However, the modulations of pump intensity are mostly due to the interference between optical frequencies of the noiseless pump pulse and optical frequencies of the pump ASE. Figure 111.7 presents simulations and analytic predictions for two different ASE spectra that have a FWHM equal to 0.14 nm, i.e., the same coherence time, for a fractional ASE energy equal to  $10^{-3}$ . In the first case [Figs. 111.7(b) and 111.7(e)], a 20th-order super-Gaussian filter with 0.20-nm FWHM has been used to filter the ASE. A large decrease in the level of the pedestal is observed away from the peak of the pulse, although the pedestal conserved its value closer to the peak, as expected from the dependence of the pedestal to the spectrum of the ASE. In the second case [Figs. 111.7(c) and 111.7(f)], the ASE has a Gaussian spectrum with 0.14-nm FWHM centered 0.07 nm away from the central wavelength of the pump. The contrast is significantly degraded compared to Figs. 111.6(c) and 111.6(f), and an increase of the pedestal intensity by approximately 20 dB is observed. Optimization of the contrast can be performed by proper spectral filtering of the pump. A narrow filter on the pump pulse increases the contrast of the recompressed signal and is not detrimental to the operation of the OPCPA system as long as the pump pulse is not temporally distorted by the spectral filter. Generally speaking, the pedestal shape, extent, and intensity vary significantly with the energy of the ASE, its spectrum, and the regime of operation of the amplifier.

### 3. Pump with ASE and Signal with Gaussian Spectral Density

In this section, the spectral density of the signal is assumed Gaussian, and the intensity of the stretched signal varies significantly as a function of time, taking its maximal value

of  $0.1 \text{ W/cm}^2$  at the peak of the pulse. The condition that the first-order derivative or second-order derivative of the function  $f$  as a function of the intensity of the signal is independent of the signal intensity is not strictly verified. Some temporal components (i.e., spectral components) of the signal have an optical intensity placing them in the quadratic-modulation regime for the OPCPA process, but other components have an optical intensity placing them in the linear-modulation regime. The contrast of the recompressed signal is generally linked in a nontrivial manner to the noise of the pump pulse. Figure 111.8 displays the transfer function between pump intensity and output signal intensity for a signal input intensity equal to  $0.1 \text{ W/cm}^2$  and  $0.05 \text{ W/cm}^2$ . While the pump intensity corresponding to point B ensures that the output signal intensity is approximately the same for these two input signal intensities (i.e., the spectral density of the amplified pulse does not depend on the wavelength at first order), it allows operation only in the quadratic-modulation regime for the highest signal intensity. Figure 111.9 presents the intensities simulated with ASE parameters identical to those of Fig. 111.6. The analytical results plotted on this figure correspond to the stretched signal pulse with a constant intensity of  $0.1 \text{ W/cm}^2$ . For the linear- and quadratic-modulation regimes, no significant difference between the two sets of simulations is observed, and the analytical derivation is still in good agreement with the simulations. In the linear regime for the peak intensity of the stretched pulse, all of the optical frequencies in the pulse are in a similar linear regime, and the resulting contrast is equivalent to the contrast obtained for a constant spectral density. The discrepancy observed for low ASE energy in the quadratic regime is more prevalent in this case, which indicates that additional contribution to the

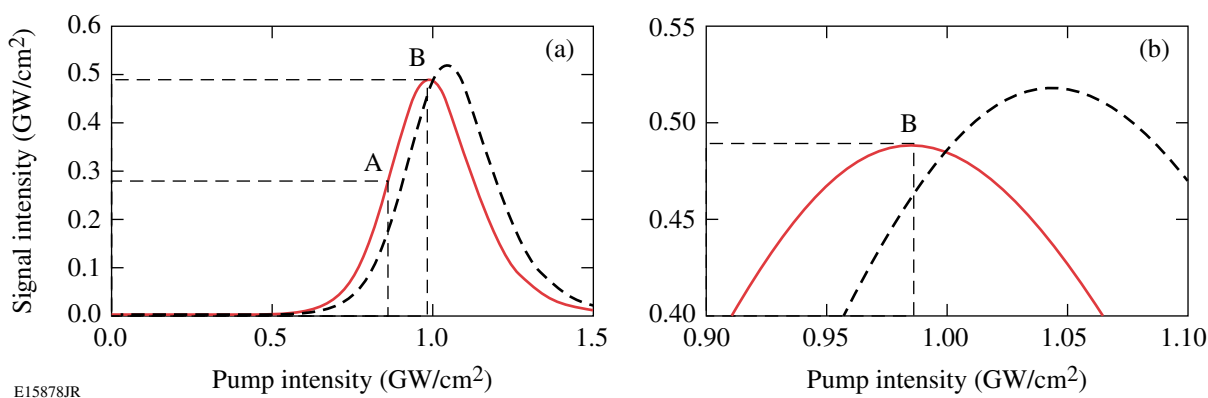


Figure 111.8

Transfer function of the parametric preamplifier for a signal intensity equal to  $0.1 \text{ W/cm}^2$  (solid curve) and  $0.05 \text{ W/cm}^2$  (dashed curve). Points A and B represent the linear- and quadratic-modulation regimes for the OPCPA system for a stretched signal intensity of  $0.1 \text{ W/cm}^2$ . (a) Full transfer function; (b) close-up around point B.

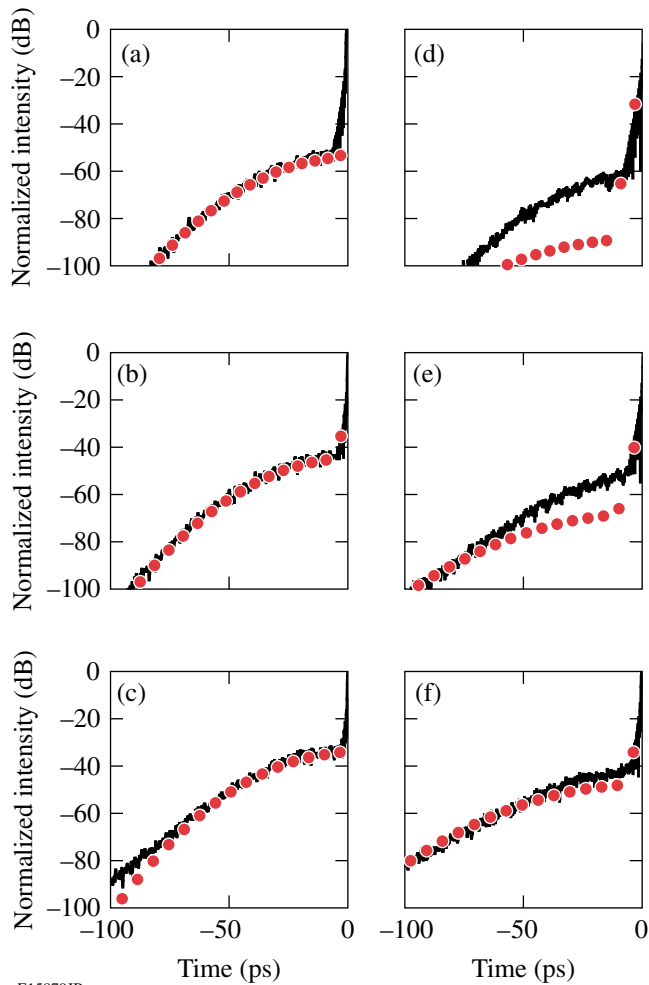


Figure 111.9

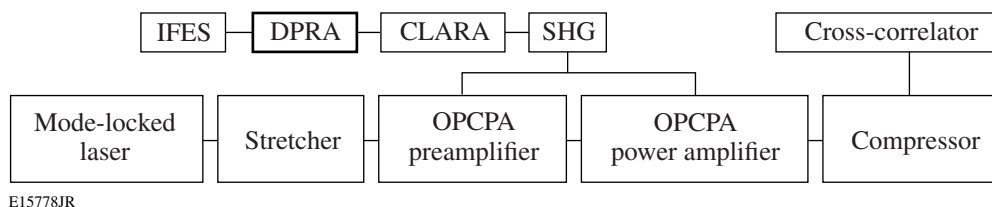
Intensity of the recompressed signal for an input signal with a Gaussian spectral density and ASE with a Gaussian spectrum with a FWHM equal to 0.14 nm. (a)–(c) correspond to an amplifier run in the linear-modulation regime when the fractional ASE energy is equal to (a)  $10^{-5}$ , (b)  $10^{-4}$ , and (c)  $10^{-3}$ . (d)–(f) correspond to an amplifier run in the quadratic-modulation regime when the fractional ASE energy is equal to (d)  $10^{-5}$ , (e)  $10^{-4}$ , and (f)  $10^{-3}$ . In each case, the simulated intensity is plotted with a continuous line, and the intensity predicted analytically is plotted with solid circles.

pedestal is present due to some components of the signal in the linear-modulation regime. The coupling between pump intensity and amplified signal intensity for these wavelengths is smaller than at point A of Fig. 111.4. A fit of the dashed curve of Fig. 111.8 at its intersection with the vertical dashed line representing the pump intensity for these simulations leads to  $f_{(1,N)} = 4$ , which implies a smaller impact of the pump intensity modulation. These results demonstrate that, in the general case, both linear- and quadratic-modulation regimes influence the induced pedestal on an OPCPA system.

## Experimental Demonstration of Temporal Contrast Improvement of an OPCPA System by Pump Spectral Filtering

### 1. Experimental Setup

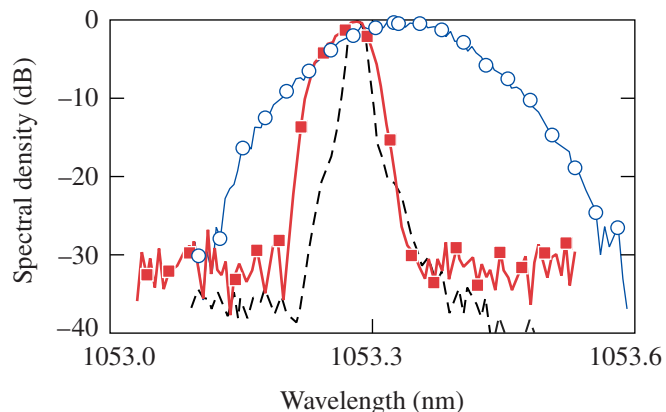
A general approach to significantly improve the contrast of OPCPA systems by spectrally filtering the pump pulse has been experimentally demonstrated. Simple and efficient filtering of the pump pulse is performed in a regenerative amplifier using a VBG, and the bandwidth of the filtering is narrowed significantly by the large number of round-trips in the cavity. Contrast improvement by regenerative spectral filtering was performed on the prototype front end of the OMEGA EP Laser Facility (Fig. 111.10).<sup>10,17</sup> The pump pulse is generated by a fiber integrated front-end source (IFES), where a 2.4-ns pulse around 1053 nm is temporally shaped to precompensate the square-pulse distortion during amplification. This pulse is amplified at 5 Hz from 100 pJ to 4 mJ in a diode-pumped regenerative amplifier (DPRA).<sup>20</sup> One of the flat end-cavity mirrors of the DPRA is replaced by the VBG and a flat mirror, so that the mirror acts as the DPRA end-cavity mirror and the beam is reflected twice per round-trip on the VBG. The incidence angle on the VBG, designed for high reflection at 1057.5 nm at normal incidence, is approximately  $7^\circ$  to provide maximum reflection at 1053 nm. The VBG is a bulk piece of photothermorefractive glass, where a grating is permanently written by UV illumination followed by thermal development.<sup>21</sup> The damage threshold of similar VBG's has been found to be higher than  $10 \text{ J/cm}^2$  in the nanosecond regime. With sol-gel antireflection coating, the VBG has a single-pass reflectivity of 99.4% at 1053 nm, and the slight increase in the DPRA build-up time due to the additional losses was compensated by increasing the diode-pump current. No change in the output beam spatial profile was observed. Without active temperature control of the VBG, the DPRA operated for several days in a temperature-controlled room with no variation in performance. (Additional characterization can be found in Ref. 22.) The bandwidth of the VBG reflectivity around 1057.5 nm is 230 pm, which, assuming a Gaussian shape, should provide a 23-pm bandwidth after 50 round-trips in the DPRA, with two reflections on the VBG per round-trip. With the intracavity VBG, the unseeded DPRA output spectrum shows a reduction of the bandwidth of the DPRA from 146 pm to 41 pm, but is broad enough to amplify the pump pulse without distortion (Fig. 111.11). Subsequent amplification to 2 J is performed by four passes in a crystal large-aperture ring amplifier containing two flash-lamp-pumped Nd:YLF rods, after apodization of the DPRA beam.<sup>23</sup> Frequency conversion to 526.5 nm occurs in an 11-mm LBO crystal with an efficiency of 70%. Filtering in the DPRA decreases the amount of ASE from the IFES and



E15778JR

Figure 111.10

Schematic of the laser system. IFES: integrated front-end source; DPRAs: diode-pumped regenerative amplifier; CLARA: crystal large-aperture ring amplifier; SHG: sum-harmonic generation. Filtering of the pump pulse is performed in the DPRAs (shown above in bold).



E15779JR

Figure 111.11

Optical spectrum of the unseeded DPRAs measured with a mirror in the cavity (thin solid curve with open circles) and with the VBG in the cavity (solid curve with solid squares). The optical spectrum of the signal amplified by the DPRAs (dashed curve) is limited by the resolution of the optical spectrum analyzer and is significantly narrower than the unseeded DPRAs with the intracavity VBG.

from the DPRAs itself (these two high-gain stages having the largest contribution to the pump ASE) and benefits from the large number of reflections on the filter.

The OPCA system is composed of a mode-locked laser operating at 1053 nm, an Öffner-triplet stretcher providing a dispersion of 300 ps/nm, a preamplifier with two 29.75-mm LBO crystals in a walk-off compensating geometry, a power amplifier with one 16.5-mm LBO crystal, and a two-grating compressor in a double-pass configuration. The pump pulse is split to pump the preamplifier and power amplifier. Amplification of the signal to 250 mJ is achieved, and a portion of the amplified pulse is sent to the diagnostic compressor.

## 2. Experimental Results

The temporal contrast was measured using a scanning third-order cross-correlator (Sequoia, Amplitude Technologies).

The dynamic range of the diagnostics is  $10^{11}$  but is limited to  $10^8$  by the parametric fluorescence from the OPCA system. Postpulses are due to multiple reflections in the cross-correlator and are of no practical concern. Figure 111.12 displays the cross-correlations measured (a) when the preamplifier and power amplifier are operated at full energy, (b) when only the preamplifier is operated at saturation, and (c) when only the preamplifier is operated at half its nominal output power. The prepulse contrast is consistently improved with the intracavity VBG. The pump-induced contrast degradation is particularly important in the preamplifier, even when it is run at saturation, and a contrast improvement of the order of 20 dB is observed. When the preamplifier is run at half output power, a larger coupling between the pump intensity and the amplified signal intensity magnifies the impact of the pump noise on the contrast. These two operating points correspond to the linear- and quadratic-modulation regimes for the preamplifier, as identified by points A and B in Fig. 111.4. The choice of the crystals and pump intensities in this system reduces the spatial-intensity modulations in the amplified signal. This decreases the temporal-intensity modulations in the amplified signal and reduces the impact of the pump-intensity variations on the contrast of the recompressed pulse. Most OPCA systems are not designed with these considerations in mind, and the contrast improvement is expected to be significant for these systems.

The optical signal-to-noise ratio (OSNR) of the OPCA pump pulse was reduced by decreasing the average power of the monochromatic source in the IFES from its nominal value of 10 mW to 2 mW, 0.4 mW, and 0.1 mW, and compensating the reduced output energy by increasing the DPRAs diode pump current. The reduced OSNR is due to the reduced seed level in both the IFES fiber amplifier and the DPRAs. Figure 111.13 displays the cross-correlations measured when the preamplifier and power amplifier are operated in nominal conditions [the cross-correlations measured for the nominal value of 10 mW can be seen in Fig. 111.12(a)]. Without spectral filtering, a large increase in the temporal pedestal is observed, and the contrast

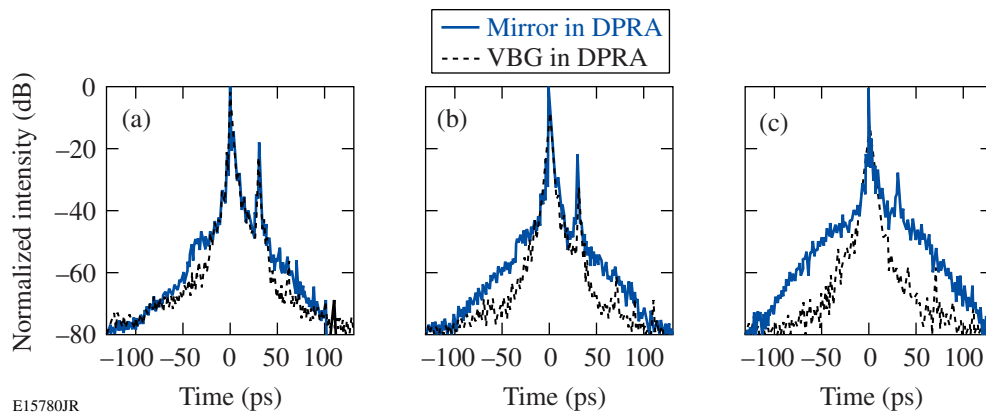


Figure 111.12

Third-order scanning cross-correlation of the OPCPA output pulse (a) when the preamplifier and power amplifier are operated at full energy, (b) when only the preamplifier is operated at saturation, and (c) when only the preamplifier is operated at half its nominal output power. In each case, the cross-correlation measured with the mirror in the DPRA is plotted with a solid line, and the cross-correlation measured with the VBG in the DPRA is plotted with a dashed line.

50 ps before the peak of the pulse is 54 dB, 46 dB, and 35 dB, respectively, for a 2-mW, 0.4-mW, and 0.1-mW average power. No contrast degradation is observed with the filtered DPRA, and the contrast 50 ps before the peak of the pulse is consistently equal to 68 dB.

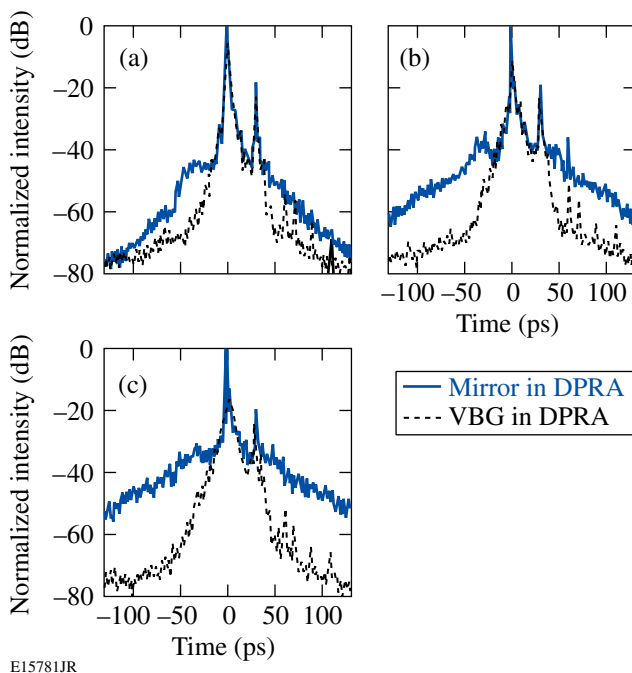


Figure 111.13

Third-order scanning cross-correlation of the OPCPA output pulse when the average power of the monochromatic laser of IFES is reduced from 10 mW to (a) 2 mW, (b) 0.4 mW, and (c) 0.1 mW. In each case, the cross-correlation measured with the mirror in the DPRA is plotted with a solid line, and the cross-correlation measured with the VBG in the DPRA is plotted with a dashed line.

## Conclusions

An analysis of pump-induced contrast degradation in an OPCPA system has been performed. The general link between pump modulation and the contrast of the recompressed pulse has been derived in the two cases of practical interest, for which pump-intensity modulation couples either linearly or quadratically to the amplified signal intensity during the parametric process. Analytical expressions linking the spectrum of the ASE present on the pump pulse to the temporal pedestal of the signal amplified in the OPCPA system have been derived and compared to simulations. Significant reduction of the induced temporal pedestal was experimentally demonstrated in an OPCPA system by filtering the pump pulse during its amplification in a regenerative amplifier. The general expressions of the contrast degradation should prove useful for understanding the contrast limitation of current OPCPA systems and predicting the performance of future systems. The demonstrated solution is simple to implement and is applicable to most OPCPA systems.

## ACKNOWLEDGMENT

This work was supported by the U.S. Department of Energy Office of Inertial Confinement Fusion under Cooperative Agreement No. DE-FC52-92SF19460, the University of Rochester, and the New York State Energy Research and Development Authority. The support of DOE does not constitute an endorsement by DOE of the views expressed in this article.

## REFERENCES

1. D. Umstadter, *Phys. Plasmas* **8**, 1774 (2001).
2. S.-W. Bahk *et al.*, *Opt. Lett.* **29**, 2837 (2004).
3. J. D. Zuegel, S. Borneis, C. Barty, B. LeGarrec, C. Danson, N. Miyanaga, P. K. Rambo, C. LeBlanc, T. J. Kessler, A. W. Schmid,

- L. J. Waxer, J. H. Kelly, B. Kruschwitz, R. Jungquist, E. Moses, J. Britten, I. Jovanovic, J. Dawson, and N. Blanchot, *Fusion Sci. Technol.* **49**, 453 (2006).
4. M. Nantel *et al.*, *IEEE J. Sel. Top. Quantum Electron.* **4**, 449 (1998).
5. V. Bagnoud, J. D. Zuegel, N. Forget, and C. Le Blanc, *Opt. Express* **15**, 5504 (2007).
6. A. Dubietis, G. Jonusauskas, and A. Piskarskas, *Opt. Commun.* **88**, 437 (1992).
7. I. N. Ross *et al.*, *Opt. Commun.* **144**, 125 (1997).
8. A. Dubietis, R. Butkus, and A. P. Piskarskas, *IEEE J. Sel. Top. Quantum Electron.* **12**, 163 (2006).
9. H. Yoshida *et al.*, *Opt. Lett.* **28**, 257 (2003).
10. V. Bagnoud, I. A. Begishev, M. J. Guardalben, J. Puth, and J. D. Zuegel, *Opt. Lett.* **30**, 1843 (2005).
11. N. Ishii *et al.*, *Opt. Lett.* **30**, 567 (2005).
12. I. Jovanovic *et al.*, *Opt. Lett.* **30**, 1036 (2005).
13. S. Witte *et al.*, *Opt. Express* **13**, 4903 (2005).
14. V. V. Lozhkarev *et al.*, *Opt. Express* **14**, 446 (2006).
15. O. V. Chekhlov *et al.*, *Opt. Lett.* **31**, 3665 (2006).
16. D. Kraemer *et al.*, *J. Opt. Soc. Am. B* **24**, 813 (2007).
17. J. H. Kelly, L. J. Waxer, V. Bagnoud, I. A. Begishev, J. Bromage, B. E. Kruschwitz, T. J. Kessler, S. J. Loucks, D. N. Maywar, R. L. McCrory, D. D. Meyerhofer, S. F. B. Morse, J. B. Oliver, A. L. Rigatti, A. W. Schmid, C. Stoeckl, S. Dalton, L. Folsbee, M. J. Guardalben, R. Jungquist, J. Puth, M. J. Shoup III, D. Weiner, and J. D. Zuegel, *J. Phys. IV France* **133**, 75 (2006).
18. N. Forget *et al.*, *Opt. Lett.* **30**, 2921 (2005).
19. I. N. Ross, G. H. C. New, and P. K. Bates, *Opt. Commun.* **273**, 510 (2007).
20. A. V. Okishev and J. D. Zuegel, *Appl. Opt.* **43**, 6180 (2004).
21. L. B. Glebov *et al.*, in *Laser Weapons Technology III*, edited by W. E. Thompson and P. H. Merritt (SPIE, Bellingham, WA, 2002), Vol. 4724, pp. 101–109.
22. A. V. Okishev, C. Dorrer, V. I. Smirnov, L. B. Glebov, and J. D. Zuegel, *Opt. Express* **15**, 8197 (2007).
23. V. Bagnoud, M. J. Guardalben, J. Puth, J. D. Zuegel, T. Mooney, and P. Dumas, *Appl. Opt.* **44**, 282 (2005).

---

# Dual Nuclear Product Observations of Shock Collapse in Inertial Confinement Fusion

The speed and heating of convergent shocks are of fundamental importance for the design of high-gain implosions in inertial confinement fusion (ICF).<sup>1,2</sup> Strong, spherically convergent shocks are formed by the rapid deposition of energy in the form of lasers (direct drive) or x rays (indirect drive) on the surface of a spherical capsule. Current ICF ignition designs include a sequence of up to four convergent shocks that must be precisely timed to coalesce at the inner shell surface in order to obtain maximal shell compression,<sup>3,4</sup> a necessity for high fusion gain. All shocks formed after the first must propagate through hot, already-shocked material, which introduces uncertainty into the shock speed and strength. A thorough understanding of shock speeds in cold and heated material, and in planar and convergent geometries, will be vital for satisfactory ICF implosion performance.

Previous studies of shock propagation relevant to ICF have focused largely on planar geometry.<sup>5,6</sup> The planar approximation works well for the propagation of converging shocks in the shell at early times, but it breaks down as the shock approaches the center of collapse. Nuclear measurements of some aspects of shock collapse using a single nuclear product have also recently been reported.<sup>7,8</sup>

This article presents the first results of temporal and spectral measurements of products from two nuclear reaction types induced by the central collapse of convergent shocks. Observations of these products provide information about the speed and heating of the shocks, as well as the state of the imploding capsule at the time of shock collapse, which, in the experiments discussed here, occurs immediately before the onset of the deceleration phase and the final stages of compression. The dual nuclear reaction measurements act as a powerful constraint and verification of observable and inferred values of shock collapse.

Direct-drive implosions were conducted on the OMEGA laser<sup>9</sup> with 60 beams of ultraviolet (351 nm) light in a 1-ns flattop pulse, a total energy of 23 kJ, and full single-beam smoothing.<sup>10</sup> The spherical capsules had diameters between

860 and 880  $\mu\text{m}$ , plastic (CH) shell thicknesses of 20, 24, or 27  $\mu\text{m}$ , and a flash coating of 0.1  $\mu\text{m}$  of aluminum. The capsules were filled with an equimolar (by atom) mixture of  $\text{D}_2$  and  $^3\text{He}$  gas with a total fill pressure ( $P_0$ ) of 3.6 or 18 atm at 293 K, corresponding to initial fill mass densities of 0.5 and 2.5  $\text{mg}/\text{cm}^3$ , respectively.

Three distinct primary nuclear reactions proceed during capsule implosions with  $\text{D}_2$  and  $^3\text{He}$  fuel:  $\text{D} + \text{D} \rightarrow ^3\text{He} + n$ ;  $\text{D} + \text{D} \rightarrow \text{T} + p$ ; and  $\text{D} + ^3\text{He} \rightarrow ^4\text{He} + p$ . The neutron and proton branches of the D-D reaction have nearly equal probabilities over temperatures of interest. The D- $^3\text{He}$  reaction depends much more strongly on temperature due to the doubly charged  $^3\text{He}$  reactant.<sup>11</sup>

Nuclear products were observed by using the proton and neutron temporal diagnostics (PTD and NTD)<sup>8,12</sup> to measure the D- $^3\text{He}$  and DD- $n$  reaction histories; multiple wedged-range-filter (WRF) proton spectrometers<sup>13</sup> to measure the D- $^3\text{He}$  proton yield and spectrum; and a magnet-based charged-particle spectrometer<sup>13</sup> to measure D-D protons emitted at shock-bang time. The birth energies of D- $^3\text{He}$  and D-D protons are 14.7 and 3.0 MeV, respectively.

Experimental results were compared with numerical simulations performed using *LILAC*,<sup>14</sup> a one-dimensional (1-D) Lagrangian hydrodynamic code, which includes laser-beam ray-tracing, a tabular equation of state, and multigroup diffusion radiation transport. The electron thermal energy is transported using a flux-limited diffusion model in which the effective energy flux is defined as the minimum of the diffusion flux and a fraction  $f$  of the free-streaming flux. The flux limiter  $f = 0.06$  unless otherwise specified.

The D- $^3\text{He}$  reaction rate history shows two distinct times of nuclear production [Fig. 111.14(a)]: “shock burn” begins shortly after shock collapse and ends near the beginning of the deceleration phase; “compression burn” begins near the onset of the deceleration phase and lasts approximately until stagnation of the imploding shell. For ordinary D $^3\text{He}$  mixtures, the DD- $n$

reaction rate during the shock burn is below the diagnostic detection threshold.

The shock and compression components can often be distinguished in  $D^3He$  proton spectra [Fig. 111.14(b)].<sup>7</sup> The protons emitted at shock-bang time experience relatively little downshift ( $\sim 0.4$  MeV) due to the low total capsule areal density ( $\rho R$ ) at that time. The shell continues to compress after shock burn ends, and by compression-bang time the  $\rho R$  has increased enough to downshift the  $D^3He$  protons by several MeV.

The  $\rho R$  during the shock burn is low enough to also allow nascent 3.0-MeV DD protons to escape the capsule [Fig. 111.14(c)]. Measurement of DD protons emitted during shock burn provides a valuable and sole measurement of the D-D shock yield when the reaction rate is below the NTD threshold. Measurement of their downshift can also provide a double check on the  $\rho R$  at shock-bang time inferred using the  $D^3He$  proton spectra, or the sole measurement in cases where the shock component of the  $D^3He$  proton spectrum cannot be separated from the compression component.

Observed and simulated shock-bang times and  $D^3He$  and DD- $p$  shock yields are shown in Fig. 111.15 as functions of shell thickness for implosions of capsules with different  $P_0$ . The shock-bang time is the time of peak  $D^3He$  nuclear production during the shock-burn phase, the  $D^3He$  shock yield includes only the contribution from the higher-energy “shock” component of the  $D^3He$ -proton spectrum, and the DD- $p$  shock yield includes only that part of the spectrum above the high-energy cutoff of ablator protons<sup>15</sup> [seen at 0.8 MeV in Fig. 111.14(c)].

The figure plots the mean and the standard error of the mean for shot ensembles of each capsule configuration. Summaries of experimental results are included in Tables 111.I and 111.II.

Experiments show that shock-bang time is linearly delayed with increasing shell thickness [Fig. 111.15(a)], corresponding to a shock speed of  $\sim 30$  km/s in the shell. No difference in shock-bang time was observed for capsules with different  $P_0$ . Simulations predict shock-bang time to occur much later than is consistent with experiments,<sup>16</sup> as well as a strong dependence on fill pressure.

Observations show that both  $D^3He$  and D-D shock yields decrease for implosions of targets with thicker shells and lower  $P_0$ . The reduction factor for lower fill pressures has a lower value (3 to 5), however, than that expected (25) due only to the density dependence of the nuclear fusion rate; the lower density also results in less-efficient thermal coupling between ions and electrons, so that the ion temperature, and consequently the nuclear fusion rate, stays higher.

The average ion temperature at shock-bang time  $\langle T_i \rangle_{sh}$  can be inferred using the measured yields of the two different nuclear reactions, based on the ratio of their respective thermal reactivities.<sup>17</sup> Figure 111.16 demonstrates the anticipated higher  $\langle T_i \rangle_{sh}$  for 3.6-atm implosions. The shock temperature of  $5.4 \pm 0.4$  keV for 24- $\mu\text{m}$ -thick, 18-atm implosions compares favorably with the value of  $6 \pm 1$  keV obtained by a fit to the shock line width, assuming only thermal broadening, reported by Petrasso *et al.*<sup>7</sup>

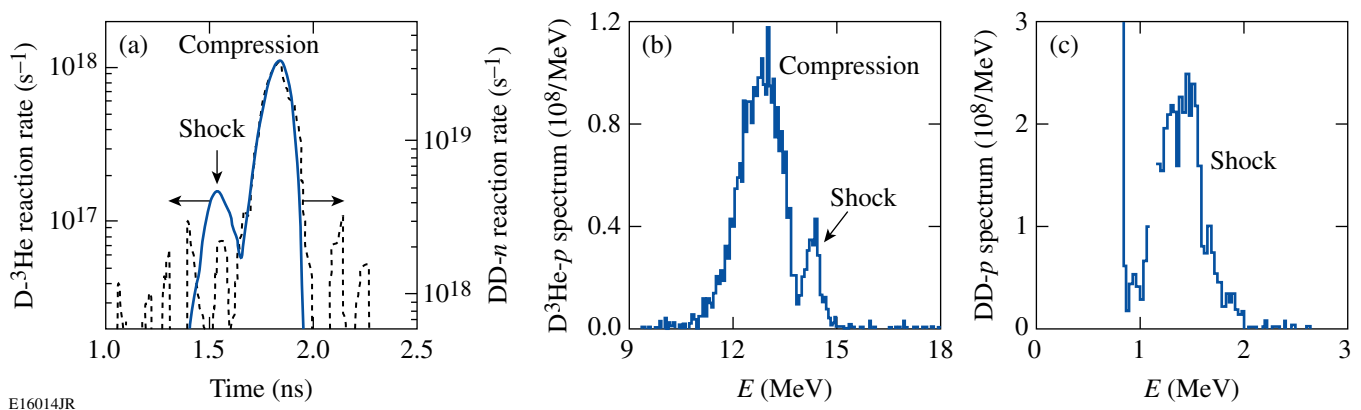
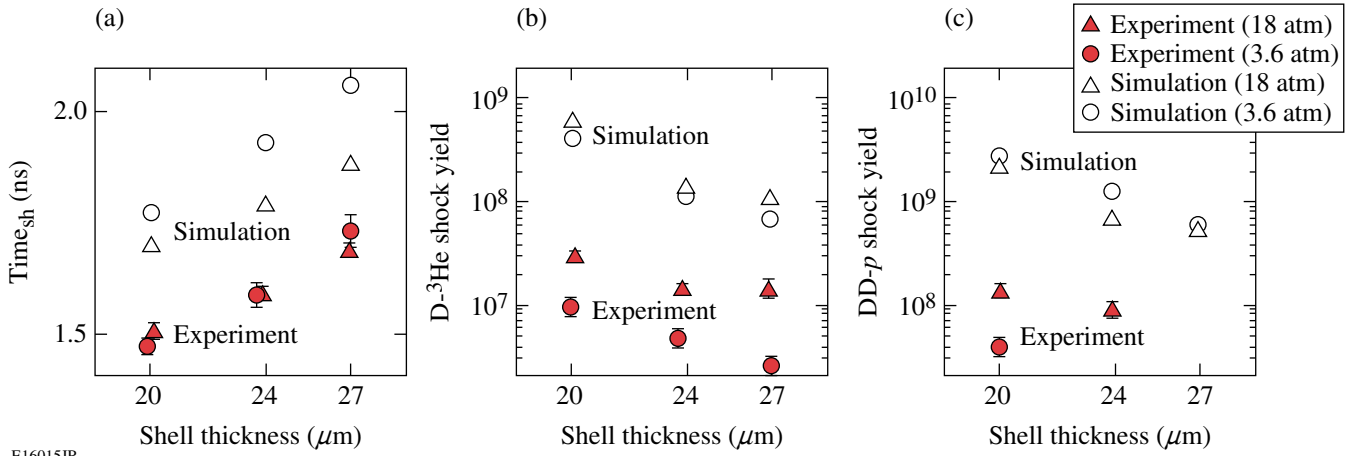


Figure 111.14

Representative experimental observations of D-D and  $D^3He$  nuclear products emitted at shock- and compression-bang time from an implosion of a 24- $\mu\text{m}$ -thick CH capsule shell filled with 18 atm of  $D^3He$  gas (OMEGA shot 38525). (a)  $D^3He$  (solid) and DD- $n$  (dashed) reaction rate histories; (b)  $D^3He$ -proton spectrum; (c) DD-proton spectrum.



E16015JR

Figure 111.15

Experimental observations (solid) and 1-D simulations (open) of (a) shock-bang time, (b)  $D-^3\text{He}$  shock yield, and (c)  $DD-p$  shock yield as a function of capsule shell thickness for ensembles of capsules filled with 18 atm (triangles) or 3.6 atm (circles) of  $D^3\text{He}$  gas.

Table 111.I: Mean and error of measured values of shock-bang time,  $D-^3\text{He}$  shock yield, and  $\rho R$  at shock time for implosions with different shell thicknesses and fill pressures. The  $D-^3\text{He}$  shock yield is shown as both an absolute yield and a percentage of the total  $D-^3\text{He}$  yield.

$P$ (atm)	$\Delta R$ ( $\mu\text{m}$ )	$N$	$t_{\text{sh}}$ (ps)	$Y_{p-s}$ ( $\times 10^7$ )	err (%)	$Y_{p-s}$ (% $Y_p$ )	$\rho R$ ( $\text{mg}/\text{cm}^2$ )
3.6	19.9	8	$1470 \pm 16$	—	—	—	—
3.6	23.7	6	$1585 \pm 27$	0.48	9	$10.6 \pm 0.9$	$9.8 \pm 0.4$
3.6	27.0	4	$1731 \pm 39$	0.25	20	$12.2 \pm 1.7$	$12.0 \pm 0.9$
18	20.1	8	$1506 \pm 16$	3.09	7	$6.2 \pm 0.5$	$8.2 \pm 1.0$
18	23.9	9	$1591 \pm 12$	1.45	9	$9.3 \pm 0.6$	$8.9 \pm 0.7$
18	26.9	6	$1690 \pm 11$	1.44	18	$19.8 \pm 2.5$	$9.4 \pm 1.2$

Table 111.II: Mean and error of measured values of  $DD-p$  shock yield, shock  $T_i$ , and  $\rho R$  at shock time inferred from the downshift of  $DD-p$ , for implosions with different shell thicknesses and 18-atm fill pressure. The  $DD-p$  shock yield is shown as both an absolute yield and a percentage of the total  $DD-n$  yield.

$P$ (atm)	$\Delta R$ ( $\mu\text{m}$ )	$N$	$\langle T_i \rangle_{\text{sh}}$ (keV)	$Y_{DD-s}$ ( $\times 10^7$ )	err (%)	$Y_{DD-s}$ (% $Y_n$ )	$\rho R$ ( $\text{mg}/\text{cm}^2$ )
3.6	19.9	5	$7.9 \pm 0.9$	4.2	10	$1.5 \pm 0.2$	$8.3 \pm 0.7$
18	20.2	3	$5.9 \pm 0.4$	14.1	13	$1.2 \pm 0.2$	$9.3 \pm 0.6$
18	23.9	3	$5.4 \pm 0.4$	9.2	20	$1.9 \pm 0.3$	$10.0 \pm 0.7$
18	27.1	2	—	—	—	—	$11.1 \pm 1.0$

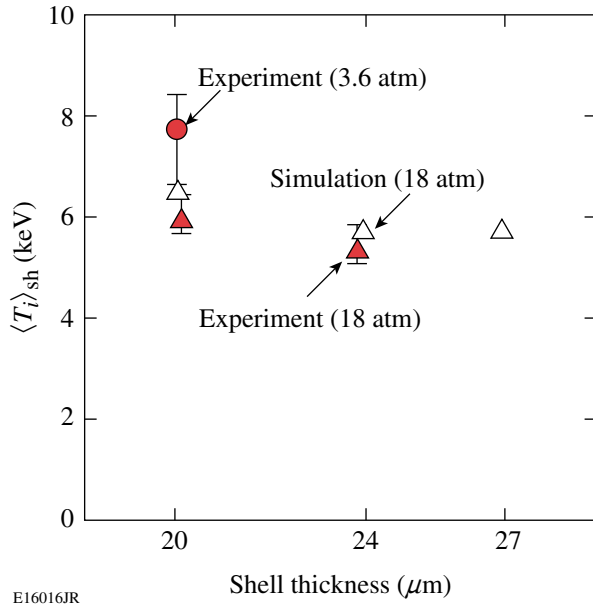


Figure 111.16 Shock-burn-averaged ion temperature, calculated using the ratio of the DD- $p$  to D- $^3\text{He}$  shock yields from experiments (solid) and from 1-D simulations (open) for capsules filled with 18 atm (triangles) and 3.6 atm (circles) of D $^3\text{He}$  gas.

One-dimensional simulations grossly overestimate the experimentally observed D- $^3\text{He}$  and DD- $p$  shock yields. The experimental yield over the calculated yield (YOC) is 3%–4% for 3.6-atm fills and 5%–15% for 18-atm fills. These higher predicted yields combined with only slightly higher values of  $\langle T_i \rangle_{sh}$  indicate that simulations calculate that, compared to experiment, capsules at shock-bang time are more highly compressed.

The compression of the capsule at shock-bang time can be quantified by the shock-burn-averaged areal density,  $\rho R_{sh}$ . Experimentally,  $\rho R_{sh}$  is inferred from the measured mean energy downshift from the birth energy of DD protons or D $^3\text{He}$  protons in the shock line, using a theoretical formalism to relate their energy loss to plasma parameters.<sup>13,18</sup> The inferred  $\rho R_{sh}$  value is insensitive to the exact values assumed, particularly when using the downshift of 14.7-MeV protons; a CH plasma density of 3 g/cm $^3$  and a temperature of 0.3 keV were used to derive the quoted  $\rho R_{sh}$  values. The simulated  $\rho R_{sh}$  is calculated as the  $\rho R$  weighted by the D- $^3\text{He}$  reaction rate over the shock burn.

Excellent agreement is observed between  $\rho R_{sh}$  inferred from spectral results obtained using both DD and D $^3\text{He}$  protons, as shown in Fig. 111.17 and Tables 111.I and 111.II. Compared to

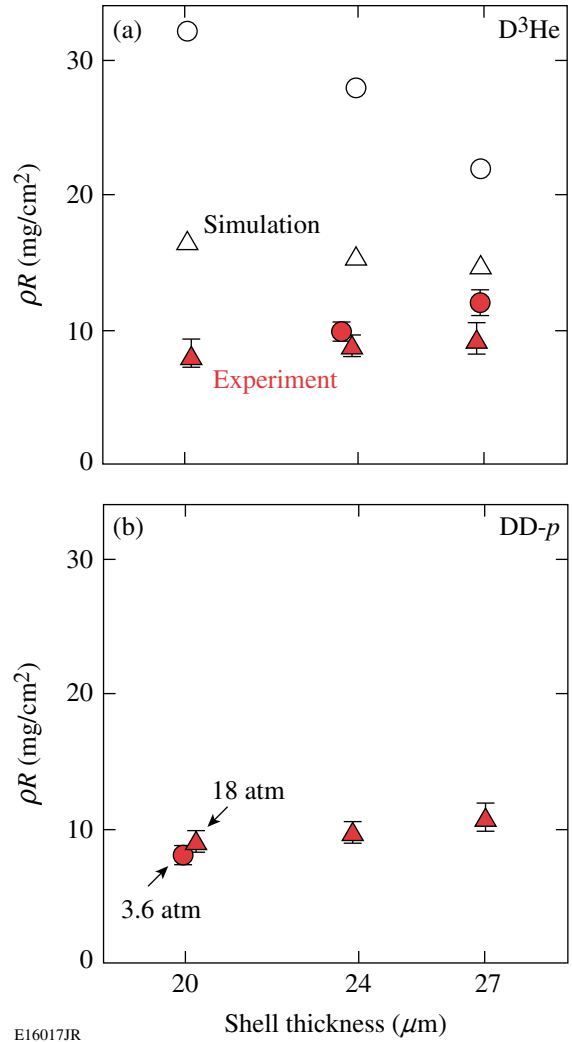


Figure 111.17 Shock  $\rho R$ 's for 18-atm (triangles) and 3.6-atm (circles) D $^3\text{He}$  fills of capsules as functions of shell thickness. The experimental  $\rho R_{sh}$  is inferred from the downshift of nascent (a) 14.7-MeV D $^3\text{He}$  protons and (b) 3-MeV DD protons from their birth energy. Markers show mean and standard error. The simulated  $\rho R$  [open markers in (a)] is the  $\rho R$  of the implosion weighted by the D- $^3\text{He}$  reaction rate over the shock burn.

experiments, 1-D simulations predict much higher  $\rho R_{sh}$  and show an opposing trend of  $\rho R_{sh}$  as a function of shell thickness and a very strong dependence of  $\rho R_{sh}$  on  $P_0$ . A higher predicted  $\rho R_{sh}$  is consistent with the expectation of higher compression discussed above.

On the basis of physical principles,  $\rho R_{sh}$  should be nearly independent of  $P_0$  since the trajectory of the shell will not be affected by the fill gas until the deceleration phase, well after shock-bang time. Scrutiny of the simulated reaction rate histo-

ries for low- $P_0$  implosions reveals additional nuclear production caused by a reflection of the outgoing shock from the imploding shell. This shock reverberation explains the larger discrepancy for the yields, shock-bang times, and  $\rho R_{\text{sh}}$ 's seen for low- $P_0$  simulations; however, no evidence of heating due to the shock reverberation is seen in the observed reaction rates.

Several competing shell-thickness-dependent effects could alter  $\rho R_{\text{sh}}$ . For the same laser drive, the same amount of shell mass gets ablated, which for thicker shells results in more remaining mass (which tends to increase  $\rho R_{\text{sh}}$ ) and lower implosion velocity (which tends to decrease  $\rho R_{\text{sh}}$ ). The opposing trends of  $\rho R_{\text{sh}}$  with shell thickness for experiments and simulations demonstrate that the simulations are improperly treating these competing effects.

The overprediction of shock yields,  $\rho R_{\text{sh}}$ 's, and time until shock collapse by 1-D simulations might at first indicate the need for 2-D or 3-D simulations to capture the complete physics of collapsing shocks. Indeed, theoretical analysis suggests that converging shocks are weakly unstable to initial asymmetries;<sup>19</sup> however, experiments have demonstrated that the observables are highly robust to drive asymmetries<sup>20</sup> and that the growth of asymmetries due to hydrodynamic instabilities is insufficient to mix the shell with the fill gas at shock collapse time.<sup>21</sup> The collapse and resulting nuclear production of converging shocks can thus be well approximated as a 1-D situation; more computationally intensive 2-D or 3-D simulations are unnecessary.

One-dimensional simulations can be adjusted to match experimental timing by increasing the flux limiter  $f$ ; however, increasing  $f$  will also push the shock yield and  $\rho R$  into further disagreement with experiments. No value of the flux limiter can match both the shock timing and yield simultaneously, suggesting a limitation of handling shock collapse using only a hydrodynamic treatment. The fuel plasma during the shock burn is hotter and sparser than it is during the compression burn, which results in lower collision frequency and ion mean free paths that are comparable to the size of the plasma. Comparison of hydrodynamic and kinetic simulations<sup>22</sup> shows that the kinetic treatment results in a weaker reflected shock and a nuclear production substantially lower during the shock burn.

In summary, nuclear production induced by the collapse of strong, spherically convergent shocks was observed using temporal and spectral measurements of products from two distinct nuclear reactions. The dual nuclear observations create a comprehensive description of the state of the implosion

at shock-collapse time, which, temporal measurements show, occurs immediately before the onset of the deceleration phase. Measuring both DD and D<sup>3</sup>He nuclear products acts as a powerful constraint and verification of data reliability; observations of their yields and spectra are used to infer temperatures and areal densities at shock-bang time near 6 keV and 10 mg/cm<sup>2</sup>, respectively. Comparison of the experimental results to predictions made by 1-D hydrodynamic simulations revealed numerous differences, including earlier time of shock collapse, lower nuclear production and fill-gas temperature, and lower capsule compression at shock-bang time. Given the importance of shock timing and heating to the success of ignition in ICF, it is worthwhile to re-examine the treatment of shocks in current hydrodynamic codes; the constraints imposed by this compelling set of dual nuclear shock-burn measurements make it possible for efficient and insightful alterations to be selectively made in ICF simulations at a level hitherto unavailable.

#### ACKNOWLEDGMENT

The authors express their gratitude to the OMEGA engineers and operations crew who supported these experiments. This work was supported in part by the U.S. Department of Energy Office of Inertial Confinement Fusion (Grant No. DE-FG03-03NA00058), by the Fusion Science Center for Extreme States of Matter and Fast Ignition (Contract No. 412761-G), by the Laboratory for Laser Energetics (Subcontract No. 412160-001G), and by the Lawrence Livermore National Laboratory (Subcontract No. B543881).

#### REFERENCES

1. J. Nuckolls *et al.*, *Nature* **239**, 139 (1972).
2. S. Atzeni and J. Meyer-ter-Vehn, *The Physics of Inertial Fusion: Beam Plasma Interaction, Hydrodynamics, Hot Dense Matter*, International Series of Monographs on Physics (Clarendon Press, Oxford, 2004).
3. D. H. Munro *et al.*, *Phys. Plasmas* **8**, 2245 (2001).
4. R. L. McCrory, R. E. Bahr, R. Betti, T. R. Boehly, T. J. B. Collins, R. S. Craxton, J. A. Delettrez, W. R. Donaldson, R. Epstein, J. Frenje, V. Yu. Glebov, V. N. Goncharov, O. Gotchev, R. Q. Gram, D. R. Harding, D. G. Hicks, P. A. Jaanimagi, R. L. Keck, J. Kelly, J. P. Knauer, C. K. Li, S. J. Loucks, L. D. Lund, F. J. Marshall, P. W. McKenty, D. D. Meyerhofer, S. F. B. Morse, R. D. Petrasso, P. B. Radha, S. P. Regan, S. Roberts, F. Séguin, W. Seka, S. Skupsky, V. Smalyuk, C. Sorce, J. M. Soures, C. Stoeckl, R. P. J. Town, M. D. Wittman, B. Yaakobi, and J. D. Zuegel, *Nucl. Fusion* **41**, 1413 (2001).
5. T. R. Boehly, E. Vianello, J. E. Miller, R. S. Craxton, T. J. B. Collins, V. N. Goncharov, I. V. Igumenshchev, D. D. Meyerhofer, D. G. Hicks, P. M. Celliers, and G. W. Collins, *Phys. Plasmas* **13**, 056303 (2006).
6. V. N. Goncharov, O. V. Gotchev, E. Vianello, T. R. Boehly, J. P. Knauer, P. W. McKenty, P. B. Radha, S. P. Regan, T. C. Sangster, S. Skupsky, V. A. Smalyuk, R. Betti, R. L. McCrory, D. D. Meyerhofer, and C. Cherfils-Clérouin, *Phys. Plasmas* **13**, 012702 (2006).

7. R. D. Petrasso, J. A. Frenje, C. K. Li, F. H. Séguin, J. R. Rygg, B. E. Schwartz, S. Kurebayashi, P. B. Radha, C. Stoeckl, J. M. Soures, J. Delettrez, V. Yu. Glebov, D. D. Meyerhofer, and T. C. Sangster, *Phys. Rev. Lett.* **90**, 095002 (2003).
8. J. A. Frenje, C. K. Li, F. H. Séguin, J. Deciantis, S. Kurebayashi, J. R. Rygg, R. D. Petrasso, J. Delettrez, V. Yu. Glebov, C. Stoeckl, F. J. Marshall, D. D. Meyerhofer, T. C. Sangster, V. A. Smalyuk, and J. M. Soures, *Phys. Plasmas* **11**, 2798 (2003).
9. T. R. Boehly, D. L. Brown, R. S. Craxton, R. L. Keck, J. P. Knauer, J. H. Kelly, T. J. Kessler, S. A. Kumpan, S. J. Loucks, S. A. Letzring, F. J. Marshall, R. L. McCrory, S. F. B. Morse, W. Seka, J. M. Soures, and C. P. Verdon, *Opt. Commun.* **133**, 495 (1997).
10. S. Skupsky and R. S. Craxton, *Phys. Plasmas* **6**, 2157 (1999).
11. H.-S. Bosch and G. M. Hale, *Nucl. Fusion* **32**, 611 (1992).
12. R. A. Lerche, D. W. Phillion, and G. L. Tietbohl, *Rev. Sci. Instrum.* **66**, 933 (1995).
13. F. H. Séguin, J. A. Frenje, C. K. Li, D. G. Hicks, S. Kurebayashi, J. R. Rygg, B.-E. Schwartz, R. D. Petrasso, S. Roberts, J. M. Soures, D. D. Meyerhofer, T. C. Sangster, J. P. Knauer, C. Sorce, V. Yu. Glebov, C. Stoeckl, T. W. Phillips, R. J. Leeper, K. Fletcher, and S. Padalino, *Rev. Sci. Instrum.* **74**, 975 (2003).
14. J. Delettrez, R. Epstein, M. C. Richardson, P. A. Jaanimagi, and B. L. Henke, *Phys. Rev. A* **36**, 3926 (1987).
15. Protons from the shell (ablator) material are accelerated by electrostatic fields while the laser pulse illuminates the capsule. These fields have decayed well before the time of nuclear production, several 100 ps after the end of the pulse, so they do not affect nuclear product spectra. See also D. G. Hicks, C. K. Li, F. H. Séguin, J. D. Schnittman, A. K. Ram, J. A. Frenje, R. D. Petrasso, J. M. Soures, D. D. Meyerhofer, S. Roberts, C. Sorce, C. Stoeckl, T. C. Sangster, and T. W. Phillips, *Phys. Plasmas* **8**, 606 (2001).
16. Comparison of absolute shock-bang times, which is timing with respect to the onset of the laser drive pulse, is quoted here. Comparison of the relative shock-bang times, with respect to the initial rise of compression burn, reveals that simulations predict shock-bang time to occur  $12 \pm 15$  ps early for 18-atm fills and  $65 \pm 15$  ps late for 3.6-atm fills.
17. C. K. Li, D. G. Hicks, F. H. Séguin, J. A. Frenje, R. D. Petrasso, J. M. Soures, P. B. Radha, V. Yu. Glebov, C. Stoeckl, D. R. Harding, J. P. Knauer, R. L. Kremens, F. J. Marshall, D. D. Meyerhofer, S. Skupsky, S. Roberts, C. Sorce, T. C. Sangster, T. W. Phillips, M. D. Cable, and R. J. Leeper, *Phys. Plasmas* **7**, 2578 (2000).
18. C. K. Li and R. D. Petrasso, *Phys. Rev. Lett.* **70**, 3059 (1993).
19. J. H. Gardner, D. L. Book, and I. B. Bernstein, *J. Fluid Mech.* **114**, 41 (1982).
20. J. R. Rygg, J. A. Frenje, C. K. Li, F. H. Séguin, R. D. Petrasso, F. J. Marshall, J. A. Delettrez, J. P. Knauer, D. D. Meyerhofer, and C. Stoeckl, "Observations of the Collapse of Asymmetrically Driven Convergent Spherical Shocks," manuscript in preparation (2007).
21. J. R. Rygg, J. A. Frenje, C. K. Li, F. H. Séguin, R. D. Petrasso, V. Yu. Glebov, D. D. Meyerhofer, T. C. Sangster, and C. Stoeckl, *Phys. Rev. Lett.* **98**, 215002 (2007).
22. O. Larroche, *Eur. Phys. J. D* **27**, 131 (2003).

---

# Equation-of-State Measurements in Ta<sub>2</sub>O<sub>5</sub> Aerogel

## Introduction

In the last 15 years, there has been considerable interest in experiments that use laser-driven shock waves to measure high-energy-density equation-of-state (HED-EOS) data.<sup>1–5</sup> During this time, the generation of laser-driven shock waves has been refined, and the accuracy of the techniques employed has been improved significantly. Highly accurate optical studies of SiO<sub>2</sub> with laser-driven shock waves have shown strong agreement with experimental results obtained with other established drivers;<sup>6</sup> these measurements have extended the available data to many millions of atmospheres and identified new mechanisms that affect the material's HED-EOS.<sup>7</sup> Many HED-EOS experiments use standards or reference materials to which the behavior of the studied material is compared. These impedance-matching experiments are particularly important in laser-driven shock-wave experiments where nonreferenced HED-EOS measurements are complex.<sup>8,9</sup> The measurements on SiO<sub>2</sub> and the consistent structure of quartz lend themselves to the establishment of quartz as a standard material, as will be demonstrated in this study.

While shock waves in a material in its standard state can produce a wide range of pressures (depending upon the strength of the shock wave), the density and temperature states attainable are limited to the locus of solutions for the hydrodynamic equations commonly known as the principal Hugoniot of the material. One method to expand the attainable states from shock waves is to alter the initial density of the study material.<sup>10</sup> Experiments on these porous materials then enable the researcher to attain measurements of the material's HED-EOS over a broad range of conditions. Additionally, experiments on porous materials have also been used to understand the exotic shock phenomenon of supersonic, radiative transport.<sup>11</sup>

In supersonic radiative transport, the radiative flux from a shock front exceeds the material flux, indicating that the radiation front advances faster than the material shock front.<sup>12</sup> The experimental study in Ref. 11 used tantalum pentoxide (Ta<sub>2</sub>O<sub>5</sub>) aerogels as a host material for the study of radiative transport.

These low-density aerogels were shocked to pressures over a million atmospheres, and both the radiation and hydrodynamics were tracked experimentally. However, to fully understand this experiment and future experiments with this material, reliable radiation-hydrodynamic (RadHydro) simulations are needed, which requires an understanding of the HED-EOS of the study material. To date, there were no HED-EOS measurements to provide guidance for the development of theoretical models of this high-porosity material.

This study provides accurate EOS measurements on Ta<sub>2</sub>O<sub>5</sub> aerogel material to support model development. It uses the accumulated developments in laser-driven shock waves and their diagnosis to obtain compression and temperature data at pressures up to 3 Mbar ( $\sim 3 \times 10^6$  atm). At these pressures, the Ta<sub>2</sub>O<sub>5</sub> aerogels compress over four times their initial density and achieve temperatures  $\geq 5$  eV ( $\geq 60,000$  K). The aerogel densities used in this study are 0.1, 0.15, and 0.25 g/cm<sup>3</sup>, far smaller than the solid-state density of this material, 8.2 g/cm<sup>3</sup>. Twelve beamlines of the OMEGA Laser System<sup>13</sup> generated experimental pressures up to 1.25 Mbar in the 0.1-g/cm<sup>3</sup> aerogel and up to 3 Mbar in the 0.25-g/cm<sup>3</sup> aerogel. Since the material is transparent, the shock velocity was diagnosed with Doppler interferometry,<sup>14</sup> and the temperature was diagnosed with a streaked optical pyrometer.<sup>15</sup> Impedance-matching experiments were performed using two reference standards: aluminum (a legacy standard) and alpha quartz.

The shock-wave driver, diagnostics, and experimental materials necessary for this study will be discussed in the next section. The remaining sections (1) give important experimental observations, including the physical properties of the Ta<sub>2</sub>O<sub>5</sub> aerogel samples (refractive index and density as well as the manufacturing residuals present), the measurements that justify the use of quartz as a reference material, and the EOS measurements (density, temperature, and pressure) of the HED Ta<sub>2</sub>O<sub>5</sub>; (2) discuss the EOS measurements with respect to the available qEOS model; (3) address a diagnostic modification that could benefit future studies of this type; and (4) present conclusions.

## Experimental Technique

This experimental study used laser-driven shock waves to achieve the desired states required for HED-EOS model refinement. The OMEGA laser<sup>13</sup> is the driver for the experiments; the diagnostics were the velocity interferometer system for any reflector (VISAR)<sup>14</sup> and the streaked optical pyrometer (SOP).<sup>15</sup> Using these two diagnostics, it is possible to completely determine the EOS of a material using the impedance-matching technique. These diagnostics operate on a subnanosecond time scale so that they can fully capture the material response over the entire multnanosecond OMEGA laser pulse. The millimeter-scale targets of this study were precision manufactured, machined, and assembled through a collaboration between technicians in the LLE Target Fabrication Group and chemists at the Lawrence Livermore National Laboratory Target Fabrication Group.

OMEGA is a 60-beam, 351-nm, third-harmonic Nd:glass laser system designed for spherical illumination of imploding spherical targets.<sup>13</sup> To produce shocks in these planar EOS targets, up to 12 of the OMEGA beamlines irradiate the target package. Six of these beams have an angle of incidence of  $23^\circ$  with respect to the target normal; the other six are incident at  $48^\circ$ . All of the beams are focused (at  $f/6.7$ ) to the same spot on the target. Each beam was outfitted with a distributed phase plate<sup>16</sup> that produces a super-Gaussian intensity distribution at the target with a full width at half maximum (FWHM) of approximately  $800\ \mu\text{m}$ . A 3.7-ns, flattop pulse shape was used to maximize the steadiness of the shock-wave front while minimizing the coronal temperature for the desired experimental conditions. The total energy per beamline was  $\sim 240\ \text{J}$  of 351-nm radiation, yielding irradiances in the range of 15 to  $80\ \text{TW}/\text{cm}^2$ , depending on the number of beams and their incidence angle.

The primary diagnostics used during this experimental campaign were the VISAR<sup>14</sup> and the SOP.<sup>15</sup> Due to the fact that the shocked states are very hot ( $\geq 1\ \text{eV}$ ), the shocked material has a significant population of free electrons and readily emits in the near-infrared, optical, and ultraviolet portions of the spectrum. The VISAR records the time evolution of the Doppler shift of a probe laser that results from the advancing reflective shock-wave front. With the measurement of the shock-wave velocity in the reference material (or witness) and the target, the pressure and density of the shocked material can be determined with the impedance-matching technique. The SOP records the time evolution of the shock emission, which can then be related to a Planck radiation source to determine the temperature of the shock front. Using these diagnostics it is possible to fully capture the EOS of a shocked material.

The VISAR and the SOP share a common telescope located on the experimental axis directly opposite the OMEGA beams used to launch the shock wave into the sample (see Fig. 111.18). The telescope includes a mechanical assembly that allows the *in-situ* pointing and focusing of the diagnostics on the experimental package. The probe beam and the self-emission from the shock are relayed from the target, and a dichroic beam splitter separates the VISAR probe beam from the rest of the self-emission. Both the VISAR probe beam and the self-emission are relayed to the front of streak cameras that provide two-dimensional records. One dimension corresponds to a slit view of the relayed image, and the second dimension corresponds to a time sweep of that slit view. The spatial information from the slit allows the records from these diagnostics to be used to obtain shock evolution on complex targets with more than one region of interest.

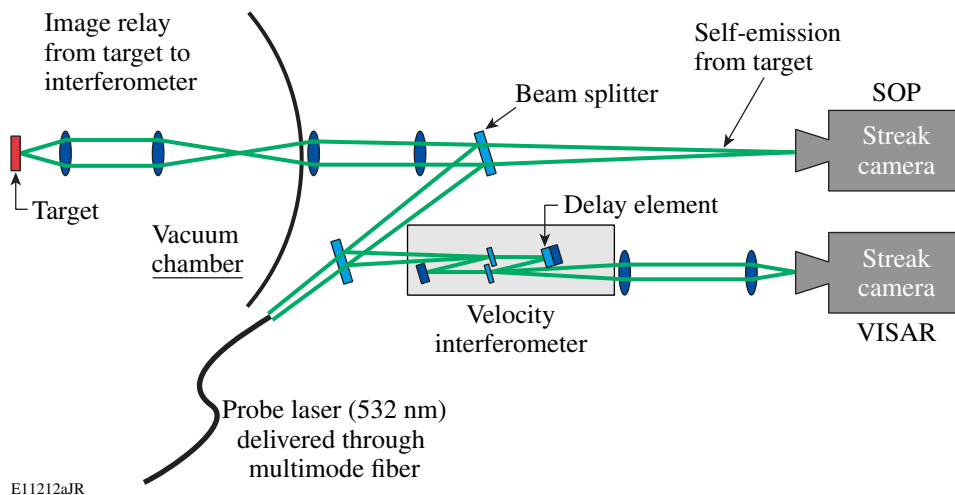


Figure 111.18  
Basic configuration of the VISAR/SOP system on OMEGA. VISAR: velocity interferometer system for any reflector; SOP: streaked optical pyrometer.

E11212aJR

Figure 111.19 shows side-by-side VISAR and SOP records that are representative of the data taken for this study. In the case of this experiment, OMEGA shot 37190, experimental records from an optically transparent, quartz/ $Ta_2O_5$  aerogel target (image in Fig. 111.20) are shown. The two diagnostic records are displayed as two-dimensional, gray-scale density plots with the brightest regions being darkest. Time zero is the point at which the OMEGA drive beams begin to irradiate the target. Variations in the gray scale are related to shock evolution, showing that the material reflectivity (VISAR record) and the brightness (SOP record) are not constant. The two main contributors to this behavior are shock strength and the local material properties. The shock strength affects the quantity and energy of the free electrons, and the material properties dictate the scattering of light. The relative location of the fringes on the VISAR record corresponds to the shock velocity. The shock brightness temperature corresponds to the intensity of the SOP record.

The targets used in this study consist of a pusher assembly (a plastic ablator and an aluminum or quartz reference) that transmits a shock wave into a low-density aerogel sample (silica or  $Ta_2O_5$ ) that is under study. These targets are generally 3-mm square, and the aerogel targets are transparent to optical wavelengths (Fig. 111.20). The targets are mounted on stalks and oriented such that the OMEGA beams are incident symmetrically about the target normal and the two principal diagnostics (VISAR and SOP).

The reference assembly has two components: a plastic ablator and a reference material. The plastic ablator is a 20- $\mu\text{m}$ -thick foil of polystyrene (CH) that is irradiated by the laser.

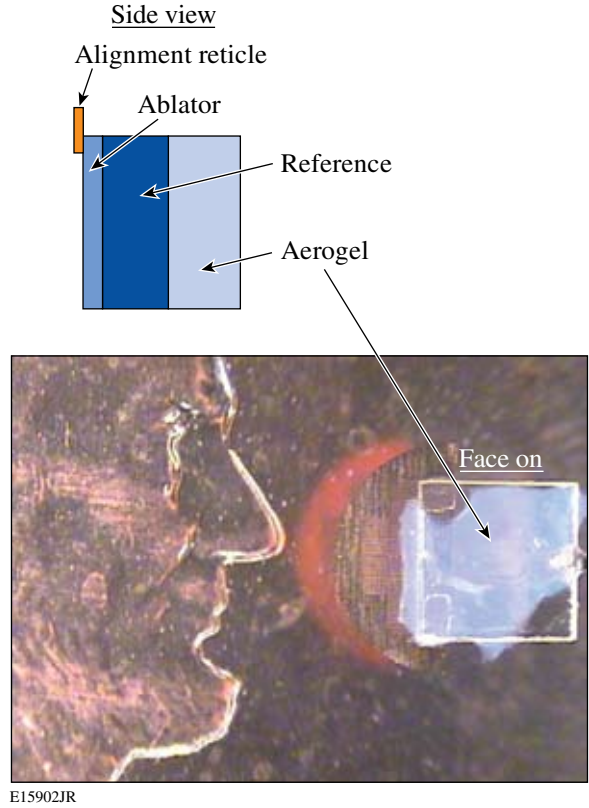


Figure 111.20  
A typical  $Ta_2O_5$  aerogel, planar target with a plastic ablator and quartz reference shown relative to a penny. These targets are generally  $3 \times 3$ -mm slides attached to a mounting stalk. This view shows the target as seen from the diagnostics (VISAR and SOP). The backing is a combination of a plastic ablator and a quartz slide, and the light amorphous material is the aerogel. Target alignment reticles, the grid to the left of the sample, are used to aid in pointing, rotation, and focusing during the experiment.

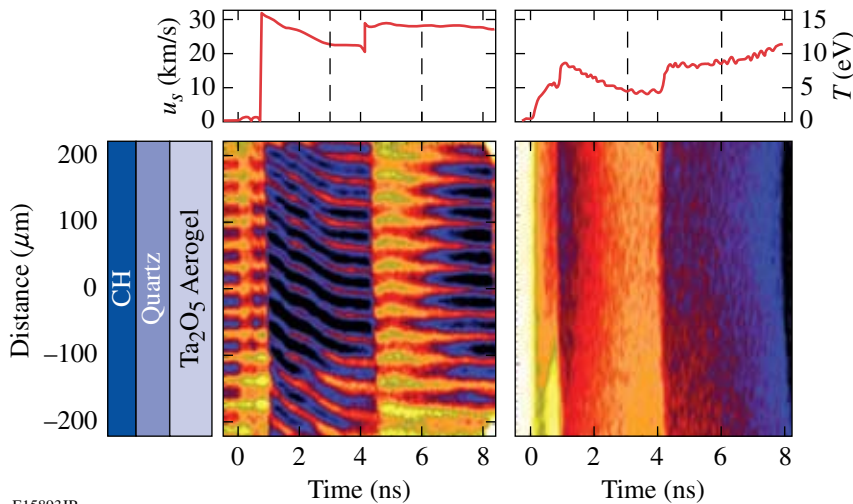


Figure 111.19  
The target cross-section is depicted on the left. The VISAR (left plot) and SOP (right plot) records for OMEGA shot 37190 give simultaneous records of the evolution of shock velocity and shock temperature along with the associated inferred velocity and temperature profiles for a 12-beam, 1.9-TW/cm<sup>2</sup> shot on a quartz reference  $Ta_2O_5$  aerogel target. Each lineout is taken at position zero in the records, which corresponds to the same point on the target.

Polystyrene is commonly used as the ablator due to its low atomic number [which reduces the production of high-energy ( $>2$  keV) x rays] and its ease of handling and machining. Lower-energy x rays are more easily absorbed in the dense, highly ionized, shocked ablator, keeping x rays away from the reference and the target and minimizing the preheat of the materials before the shock arrives. The ablator thickness is chosen to be about twice the ablation depth of the laser to ensure that none of the higher-atomic-number reference material is heated by the laser while minimizing the amount of time the shock propagates through the ablator. The ablator is attached to the reference material using a UV-cured epoxy.

The two reference materials used in this study were aluminum and z-cut alpha quartz. The aluminum pushers were approximately  $70\ \mu\text{m}$  thick while the alpha-quartz thicknesses were  $100\ \mu\text{m}$  thick to compensate for the slightly lower x-ray absorption in the quartz. The aerogels were mounted to the aluminum reference by bonding a freestanding aerogel sample onto an aluminum foil. To ensure that the glue did not wick into the aerogel, the samples were glued only at the edges, again with the UV-cured epoxy. The consequence of gluing the aerogel to the aluminum was that gaps, owing to the surface roughness of the aerogel, were present between the reference and the target. These gaps increase the uncertainty in the selection of the proper isentrope (initial state) for the release wave. With the alpha-quartz pushers the aerogel was grown directly onto the pusher, eliminating the gaps at the contact surface. This manufacturing technique was possible because, while the aluminum would disintegrate in the environment of the aerogel manufacturing process, the alpha quartz was unaffected.

Tantalum pentoxide, in its standard state, is a white to creamy-white solid with a density of  $\sim 8.2\ \text{g/cm}^3$ . The material has a relatively large band gap of  $\sim 4.2\ \text{eV}$ , a high index of refraction ( $\sim 2.1$  at  $532\ \text{nm}$ ), low absorption of optical and IR wavelengths ( $300\ \text{nm}$  to  $2\ \text{mm}$ ), and a low melting point ( $\sim 1800\ \text{K}$ , as compared to pure Ta,  $\sim 2700\ \text{K}$ ). The  $Ta_2O_5$  aerogel in this study had three mean densities:  $0.1$ ,  $0.15$ , and  $0.25\ \text{g/cm}^3$ . Since the aerogel grains are of the order of  $2$ - to  $50$ -nm scale, much less than the wavelength of light, a significant amount of Rayleigh scattering occurs within these aerogels. This limits the maximum sample thickness that can be probed with optical diagnostics to a few-hundred micrometers for  $0.1\text{-g/cm}^3$  aerogel and approximately  $100\ \mu\text{m}$  for the  $0.25\text{-g/cm}^3$  aerogel.

The  $Ta_2O_5$  aerogels were produced by the Target Fabrication Group at Lawrence Livermore National Laboratory via a

sol-gel process that entails the hydrolysis of tantalum ethoxide [ $Ta(OC_2H_5)_5$ ] in an ethanol solution.<sup>17</sup> The targets are grown by dip-coating quartz slides in the gelatinous solution. They are then placed in a casting vessel for supercritical extraction of the ethanol. While in the solution and during the extraction of the ethanol solvent, the tantalum atoms bond with oxygen atoms, forming primarily  $Ta_2O_5$  molecules. Unbonded surface oxygen atoms may terminate in either a hydroxyl or an alkynol (typically methanol) group. If the aerogel is sintered after the drying process, the alkyl groups will be released, leaving only hydroxyl groups, which greatly increases the water absorptivity of the aerogel. Samples studied with an aluminum reference are then removed from the quartz and bonded to the reference assembly. Quartz-referenced targets merely require affixing the plastic ablator on the quartz slide.

Porous aerogels are hydrophilic, readily absorbing atmospheric moisture, which is physisorbed (held by Van der Waals forces). The high polarizability of the hydroxyl groups as compared to an alkyl group makes the sintered materials especially hydrophilic, making it difficult to remove all of the moisture from the sample. Most experiments with a  $Ta_2O_5$  aerogel (including this study) use unsintered samples, so that these aerogels have residual alkyl groups that are weakly chemically bound, or chemisorbed, to the surfaces of the aerogel structures. Combustion analysis puts the mass percentage of carbon at  $1\%$  or less, which is interpreted as a chemically absorbed contaminant that is present during all unsintered studies with this material.

The aerogel targets used in this study were produced by creating a "vat" of the catalyzed tantalum ethoxide/ethanol solution as described above. The samples were formed on quartz slides by coating them with the gelatin and placing the slide in a casting vessel. The manufacturer casts a much larger witness from the same vat that is machined and weighed for density estimates. These growth techniques are expected to be highly reproducible with manufacturer-quoted density errors of less than  $10\%$ . A systematic densification of the samples (compared to the witness) is possibly due to an increase in the importance of capillary effects for the large-aspect-ratio targets.

### Experimental Observations

In this section, the series of measurements required to determine the EOS of the  $Ta_2O_5$  aerogel will be discussed. The measurements can be subdivided into two categories: (1) characterization of the targets and the reference and (2) the actual target experiments.

The characterization measurements provide input so that the target experiments can be evaluated. They include the refractive-index characterization (needed to determine shock velocity), the density characterization (needed for the impedance-matching technique), and the quantification of manufacturing residuals (needed to verify the manufacturer's estimate). The refractive index was measured as an input to the shock-velocity measurements, and this value helped evaluate density measurements. To determine the amount of absorbed contaminants removed prior to an experiment, a series of experiments were performed that exposed aerogel samples to heat and vacuum to determine the quantity and type of contaminants for comparison with the manufacturer's estimates.

With the characterization of the target and the reference materials established, the necessary inputs are available for interpreting experimental observations of the EOS of Ta<sub>2</sub>O<sub>5</sub>. The observations include kinematic properties, which can be determined by measuring the shock velocities with VISAR, and the thermal properties, which can be determined by measuring the shock brightness with the SOP.

### 1. Refractive-Index Measurements of the Ta<sub>2</sub>O<sub>5</sub> Aerogel

The refractive index  $n$  of the sample material affects the VISAR sensitivity,<sup>14</sup> and due to the highly porous nature of aerogels, the optical properties of an aerogel material differ greatly from its standard amorphous state. For these aerogels, the real part of the refractive index is near unity and the imaginary part is negligible.<sup>18</sup> Due to this near-unity refractive index and the thinness of these aerogel samples, it was necessary to use an optical technique based on white-light interferometry to measure the refractive index of the targets.<sup>19</sup> This technique uses the short coherence length of white light to identify the apparent depth of a reflective surface that is viewed through a refractive medium of thickness  $d$ , as shown in Fig. 111.21(a). This depth adjustment  $\Delta L$  achieves a total optical path length (OPL\*) through the sample that is equal to the OPL from the reflective surface through air. Using these two positions to eliminate the unknown distance between the image plane and the surface of the refractive medium, a relationship among these quantities is obtained:

$$\text{OPL} - \Delta L - d = \text{OPL}^* - nd, \quad (1)$$

and after solving for  $n$ , the simple relation

$$n = 1 + \Delta L/d \quad (2)$$

is found, where  $n$  is the real part of the index of refraction.

A ZYGO NewView 5000 white-light interferometer,<sup>20</sup> was used to measure both the depth adjustment  $\Delta L$  due to the refractive property of the aerogels and the thickness of the aerogels. The objective numerical aperture (N.A.) for the  $\Delta L$  measurement was 0.075 to keep the incident rays as normal to the aerogel surface as possible. The thicknesses  $d$  of the aerogel targets were measured in the manner shown in Fig. 111.21(b). Because the refractive index for these aerogels is close to that of air and the surface of the aerogel has a surface roughness of the order of a few microns, the thickness measurements required the use of an objective with a N.A. of 0.33 to achieve a small depth of focus. The use of this relatively large N.A. limited the overall depth of field to about a millimeter. Through multiple measurements around the edge, a reasonable surface profile was obtained. The uncertainty in the  $\Delta L$  measurement was dominated by the need to use a small N.A. objective that had a depth of focus of about 0.1  $\mu\text{m}$ , resulting in an uncertainty of  $\Delta L$  at about 4%, while the uncertainty in identifying the thickness  $d$  of the target was approximately 3%. The refractive indices of the Ta<sub>2</sub>O<sub>5</sub> aerogel targets were measured to be  $1.0206 \pm 0.0010$ ,  $1.0297 \pm 0.0017$ , and  $1.0471 \pm 0.0024$  for the 0.1-, 0.15-, and 0.25-g/cm<sup>3</sup> aerogel targets, respectively.

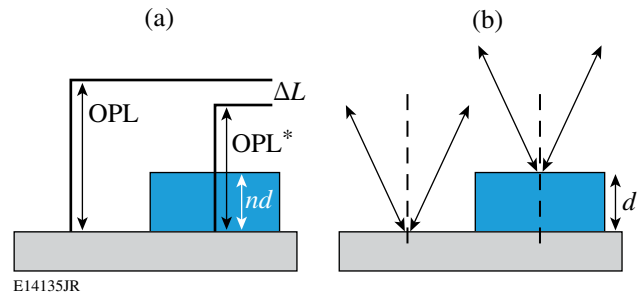


Figure 111.21

The measurement technique that determined the refractive index included two steps: First, the change in stage position,  $\Delta L$ , required that the base of the sample be kept at an equal optical path length (OPL) through air and the target (a). Second, the thickness of the sample was measured by the difference  $d$  in stage position for the target's upper surface in focus position and the base in focus position (b). Because the measurement (a) is through the sample, a small N.A. is desirable, whereas a large N.A. works best for the surface measurement of (b).

### 2. Density Measurements of an Ta<sub>2</sub>O<sub>5</sub> Aerogel

The nominal initial density values of 0.1, 0.15, and 0.25 g/cm<sup>3</sup> supplied by the manufacturer were estimates based on a witness sample rather than the actual sample itself. To determine if the target densified more than the witness during the drying process, it was deemed necessary to validate the provided estimates. These microscopic samples were validated by relating the density to the refractive index of the target.

The Clausius–Mossotti relation<sup>21</sup> applied to a highly porous material shows that the refractive index  $n$  less unity is proportional to the density  $\rho$  of the porous material:

$$n - 1 = \alpha\rho, \quad (3)$$

where  $\alpha$  is a proportionality constant associated with the strength of the dipole oscillators.<sup>18</sup> Knowing this proportionality constant and the refractive measurements discussed in **Refractive-Index Measurements of the Ta<sub>2</sub>O<sub>5</sub> Aerogel** (p. 158), the density of the actual target materials can then be determined. To ascertain the proportionality constant, the manufacturer machined a witness sample of known density to approximately 100  $\mu\text{m}$  thick. At this thickness, the technique described on p. 158 was used to determine the refractive index. Based on such measurements, the proportionality constant was determined to be  $0.188 \pm 0.013$ . Using this result, it was found that the densification of the targets compared to the witness sample is less than the combined uncertainties of the measurements of the refractive index and the proportionality constant; thus, the density of the witness accurately reflects that of the target. This equality provides no information on the purity of the samples, or what contaminants, such as water or alkyls, are present in a target. To resolve the amount of the residuals, another set of measurements was required to quantify the amount of contaminants absorbed and the nature of their bonding mechanisms.

A series of three tests were run on samples from the same batch of Ta<sub>2</sub>O<sub>5</sub> aerogel in ambient laboratory air having 30% to 40% relative humidity. The samples were approximately 0.5 cm in diameter, roughly 2 cm in height, and weighed approximately 100 mg prior to testing. The first test determined the total amount of residuals by heating the sample in a dry nitrogen atmosphere utilizing a Computrac moisture analyzer.<sup>22</sup> The samples were heated to 450 K over approximately 5 min based on the analyzer's termination criteria, then removed from the analyzer and transferred to a scale capable of 0.1-mg-accuracy measurements. The mass of the sample and absorbed moisture was tracked as a function of time after its initial exposure to air. Because of the need to transfer from the test apparatus to a scale, the measurement began ~15 s after initial exposure. Figure 111.22 shows the measured time-dependent aerogel and absorbed contaminant mass after exposure to atmosphere. Extrapolating these results to time zero, the mass of the target without any contaminants was inferred to be  $100.8 \pm 0.1$  mg. The measured initial mass (prior to heat exposure),  $104.7 \pm 0.1$  mg, was then normalized to this extrapolated value to determine the mass percentage of

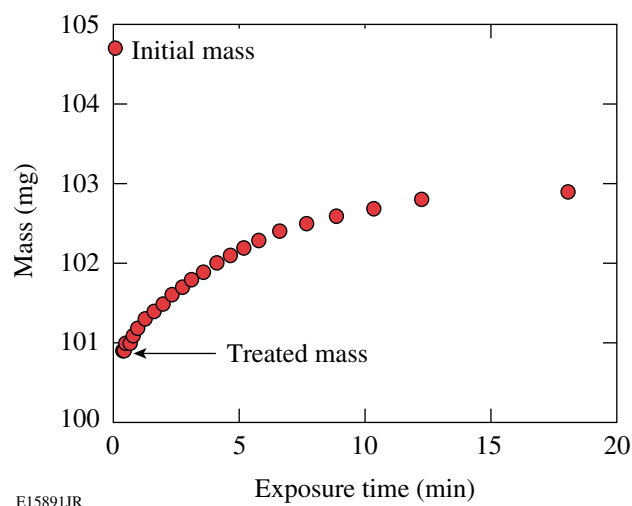


Figure 111.22

A characteristic plot of the total mass of a sample with absorbed water as a function of time after removal from the heat-addition test. Three such tests were performed: this first test was performed to measure the full chemically and physically absorbed contaminants, a second to determine the amount of physically absorbed contaminants, and a third to determine the amount of physically absorbed contaminants removed in an OMEGA shot cycle.

contaminants, which constitutes about 4% of the mass of the sample as it came from the manufacturer. The second sample was exposed to a vacuum ( $\sim 10^{-4}$  Torr), however, with no heat addition. This sample remained in a vacuum environment for a week and was then removed and measured in the same manner as previously described. After normalization, it was found that approximately 3% of the as-manufactured mass is due to absorbed contaminants that can be removed by vacuum alone. To determine if the normal OMEGA shot cycle, which is approximately 20 min of vacuum exposure, achieves the same result, a third sample was placed in an equivalent vacuum for a period of 20 min and then removed and measured in time. The extrapolation of this sample again showed that the mass percentage of physisorbed contaminants removed was 3% of the total as-manufactured mass.

These measurements indicate that approximately 1% of the as-manufactured mass fraction is from chemisorbed contaminants (contaminants that require heat addition to break bonds), while the remaining 3% is physisorbed and sufficient for vacuum removal. Correlating these results with the manufacturer's carbon estimates based on combustion analysis experiments, it is expected that the chemisorbed contaminants are the alkyls and that the primary physisorbed contaminant is absorbed water. The importance of these measurements is that the contaminants that can be removed by vacuum are removed

in times less than the OMEGA shot cycle; however, a small amount of the residual alkyl groups are present in experiments using this aerogel.

### 3. Kinematic Properties of $Ta_2O_5$ Aerogel

The kinematic properties of the  $Ta_2O_5$  aerogel samples were studied using both aluminum and alpha quartz as reference materials. The shock velocity in the aluminum reference was inferred from a quartz witness adjacent to the aerogel sample, as shown in Fig. 111.23, following the high-precision method proposed by Hicks *et al.*<sup>6</sup> In this study, the linear relationship, reported by Hicks *et al.*, between the measured shock velocity in a quartz witness and the shock velocity in aluminum,  $u_s^{Al} = B_0 + B_1(u_s^Q - \overline{u_s^Q})$ , where  $\overline{u_s^Q} = 20.57 \mu\text{m/ns}$ ,  $B_0 = 21.14 \pm 0.12 \mu\text{m/ns}$ , and  $B_1 = 0.91 \pm 0.03$ , was used to determine the aluminum shock velocity. The shock velocities in both the quartz and aerogel portions of the sample were determined with VISAR and are tabulated in Table 111.III along with the other kinematic parameters determined from the impedance-matching analysis using the SESAME-3700 equation-of-state model for aluminum.

Although aluminum is a proven reference material, the difficulties of affixing these aerogels to the aluminum contact surface without gaps proved to be challenging and had a low success rate; consequently, the target design was switched to the quartz reference similar to that shown in Fig. 111.24 with  $Ta_2O_5$  aerogel across the entire target. With the aerogel grown directly on the reference, the interface between the two materials was gapless, leading to a perfect shot success rate. With the quartz pushers and transparent aerogels, the shock velocity was continuously measured through the quartz pusher and into the aerogel. Table 111.IV lists the 19 experimental results,  $u_s^Q$  and  $u_s^{Ta_2O_5}$ , for the aerogels of the three nominal densities along with the particle velocity and pressure inferred from the impedance-matching technique using the Kerley-7360 model.

Figure 111.25 shows the results for the shock-velocity dependence on the particle velocity for the three different densities of  $Ta_2O_5$  aerogel (the initial densities 0.1-, 0.15-, and 0.25-g/cm<sup>3</sup> targets are solid diamond, open ellipses; solid diamond, gray ellipses; and open diamond, solid ellipses, respectively). Experiments with the 0.25-g/cm<sup>3</sup> aerogels were performed with both aluminum and alpha-quartz pushers. In Fig. 111.26, these points are translated into the pressure-density equation-of-state plane, with the same designations. Also shown in Fig. 111.26 are the *a priori* predictions by the qEOS model for this material (shown with the open, gray, and solid curves correlating to 0.1, 0.15, and 0.25 g/cm<sup>3</sup> as with the measurements). Figure 111.26

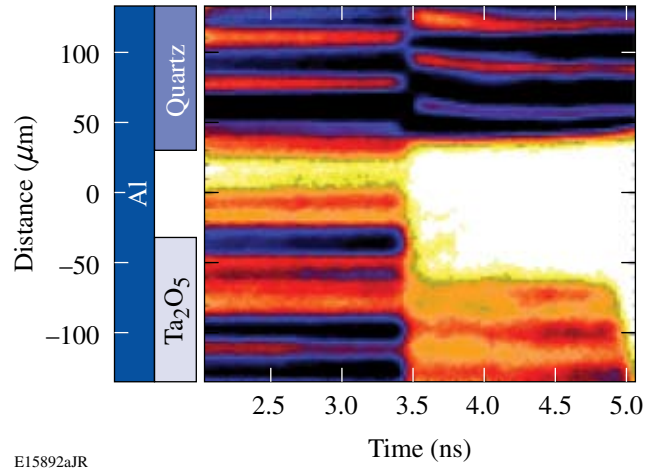


Figure 111.23

The experimental package used when the reference material is aluminum includes a quartz witness material in addition to the aerogel. The interferogram shows the shock within the aerogel (lower half) and within the quartz (upper half). Before 3.5 ns, the shock is within the aluminum reference. After 3.5 ns, the shock reaches the material interface where it breaks out of the aluminum. The quartz and aerogel shock velocities are both determined within 1 ns of the breakout.

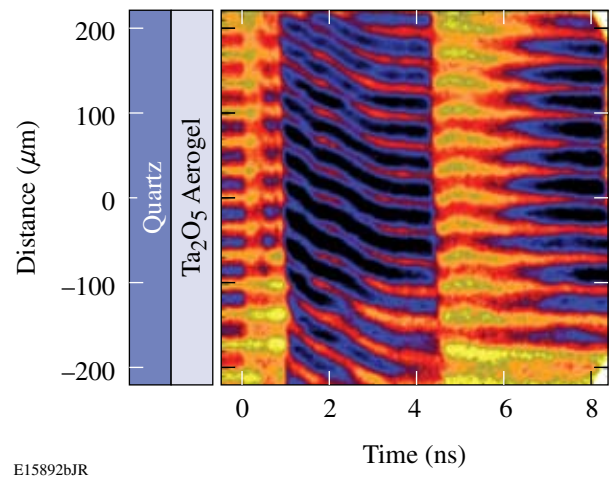


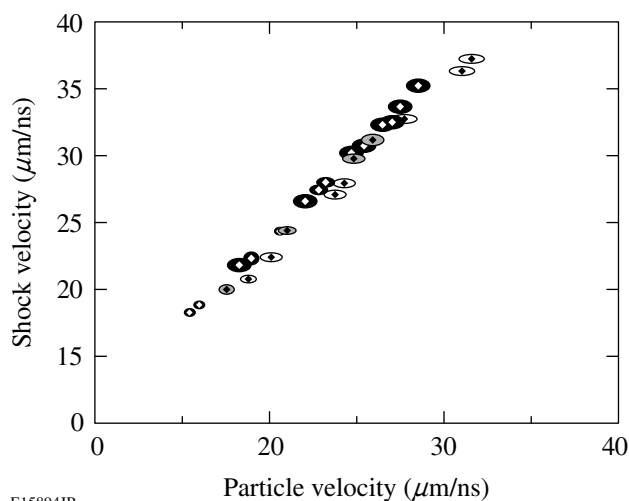
Figure 111.24

The target and VISAR data with a quartz pusher are shown. The interferogram from an experimental record shows the shock evolution as it propagates through the target. At  $t = 0$ , OMEGA begins irradiating the surface of the target. At approximately 1 ns, the shock exits the plastic ablator and enters the quartz with a reflected shock going back into the ablator. Due to the expansion of the critical surface, the coupling between the laser and the target decreases, resulting in a decay in the strength of the shock as evidenced by the fringe movement. At  $t = 3.5$  ns, the shock is strengthened by the arrival of a compression wave due to the arrival of the reflected shock at the vacuum interface. This causes the shock wave to become steady as it approaches the interface. The shock reaches the interface at 4.5 ns. In this example, the shock velocity for the quartz is determined between 3 to 4.5 ns and for the aerogel between 4.5 to 6 ns.

Table 111.III: Ta<sub>2</sub>O<sub>5</sub> aerogel-aluminum impedance matching.

Shot number	$\rho_0^{\text{Ta}_2\text{O}_5}$ (g/cm <sup>3</sup> )	$u_s^{\text{Al}}$ ( $\mu\text{m/ns}$ )	$P^{\text{Al}}$ (Mbar)	$u_s^{\text{Ta}_2\text{O}_5}$ ( $\mu\text{m/ns}$ )	$u_p$ ( $\mu\text{m/ns}$ )	$P^{\text{Ta}_2\text{O}_5}$ (Mbar)	$\rho^{\text{Ta}_2\text{O}_5}$ (g/cm <sup>3</sup> )
34136	0.25±0.025	24.6±0.3	10.1±0.3	30.6±0.5	25.3±0.7	1.94±0.18	1.46±0.24
34138	0.25±0.025	19.1±0.3	5.5±0.2	21.7±0.5	18.3±0.6	0.99±0.11	1.58±0.38
34141	0.25±0.025	25.5±0.3	11.0±0.3	32.2±0.5	26.5±0.7	2.13±0.19	1.40±0.22
34143	0.25±0.025	24.1±0.3	9.6±0.3	30.0±0.5	24.7±0.6	1.85±0.17	1.41±0.23
34915	0.25±0.025	27.1±0.3	12.6±0.3	35.1±0.5	28.4±0.7	2.50±0.22	1.32±0.18
34917	0.25±0.025	22.0±0.3	7.8±0.25	26.5±0.5	22.0±0.6	1.46±0.14	1.48±0.26
35152	0.25±0.025	26.3±0.3	11.7±0.3	33.5±0.5	27.4±0.7	2.30±0.21	1.38±0.21
35153	0.25±0.025	25.9±0.3	11.4±0.3	32.4±0.5	27.0±0.7	2.19±0.20	1.51±0.25
34136	0.25±0.025	24.6±0.3	10.1±0.3	30.6±0.5	25.3±0.7	1.94±0.18	1.46±0.24

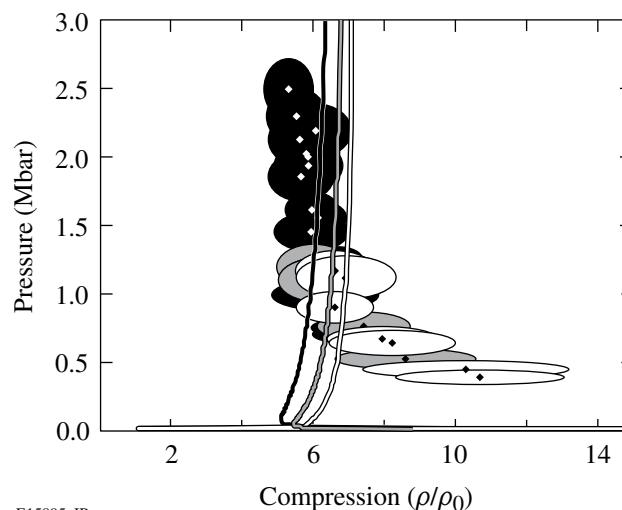
Shot data and inferred EOS parameters of Ta<sub>2</sub>O<sub>5</sub> aerogel. The columns correspond to the OMEGA shot archive number, the initial density of the aerogel, the inferred shock velocity within the aluminum, the final shock strength prior to the wave decomposition, the shock velocity measured within the aerogel, the particle velocity that conserves mass and momentum for the wave decomposition, the strength of the shock within the aerogel, and the density of the shocked compressed aerogel.



E15894JR

Figure 111.25

The shock-velocity dependence on the particle velocity for the three densities of this study. The points with the open error ellipses and gray error ellipses are from the 0.1- and 0.15-g/cm<sup>3</sup> aerogels, respectively. Experiments in 0.25-g/cm<sup>3</sup> aerogels (solid ellipses) used aluminum references and quartz references. The uncertainty of the velocity measurements was dramatically reduced with the quartz reference as evidenced by the relative area of the error ellipses.



E15895aJR

Figure 111.26

The translation of the  $u_s$ - $u_p$  plane to the shock strength versus the compressed-density plane for the three densities: 0.1, 0.15, and 0.25 g/cm<sup>3</sup> (open, gray, and solid, respectively). In addition to the measurements, the qEOS model's predicted dependence for the three densities is shown as the solid lines. As can be seen, below 1 Mbar the measured compressed density is significantly higher than that predicted; however, above 1 Mbar, the qEOS model appears to adequately predict the material behavior.

Table 111.IV: Ta<sub>2</sub>O<sub>5</sub> aerogel-quartz impedance matching.

Shot number	$\rho_0^{\text{Ta}_2\text{O}_5}$ (g/cm <sup>3</sup> )	$u_s^Q$ ( $\mu\text{m/ns}$ )	$P^Q$ (Mbar)	$u_s^{\text{Ta}_2\text{O}_5}$ ( $\mu\text{m/ns}$ )	$u_p$ ( $\mu\text{m/ns}$ )	$P^{\text{Ta}_2\text{O}_5}$ (Mbar)	$\rho^{\text{Ta}_2\text{O}_5}$ (g/cm <sup>3</sup> )
37190	0.10±0.01	21.2±0.2	7.4±0.15	27.0±0.3	23.7±0.6	0.64±0.09	0.82±0.18
37729	0.10±0.01	26.8±0.2	12.4±0.2	37.1±0.3	31.5±0.7	1.17±0.15	0.66±0.11
37730	0.10±0.01	18.5±0.2	5.5±0.1	22.3±0.2	20.1±0.5	0.45±0.06	1.03±0.29
37731	0.10±0.01	17.6±0.1	4.9±0.1	20.7±0.2	18.8±0.3	0.39±0.05	1.07±0.24
37732	0.10±0.01	21.6±0.2	7.7±0.2	27.8±0.3	24.3±0.6	0.68±0.09	0.79±0.16
37734	0.10±0.01	24.1±0.2	9.8±0.2	32.6±0.2	27.7±0.6	0.90±0.12	0.66±0.11
38790	0.10±0.01	26.4±0.3	12.0±0.3	36.2±0.3	31.0±0.8	1.12±0.15	0.69±0.14
38127	0.15±0.015	17.3±0.1	4.7±0.1	19.9±0.3	17.6±0.4	0.53±0.07	1.29±0.30
38129	0.15±0.015	19.9±0.2	6.4±0.1	24.3±0.2	21.0±0.5	0.77±0.10	1.11±0.20
38793	0.15±0.015	23.6±0.2	9.4±0.2	31.0±0.4	25.8±0.6	1.20±0.16	0.90±0.16
38794	0.15±0.015	22.8±0.2	8.7±0.2	29.7±0.3	24.8±0.6	1.10±0.15	0.90±0.15
36542	0.25±0.025	19.2±0.2	6.0±0.1	22.2±0.4	19.0±0.4	1.05±0.09	1.72±0.31
36545	0.25±0.025	24.8±0.2	10.5±0.2	31.1±0.4	25.8±0.5	2.00±0.16	1.46±0.19
36546	0.25±0.025	22.7±0.2	8.6±0.2	27.9±0.3	23.2±0.5	1.62±0.13	1.48±0.19
42092	0.25±0.025	16.5±0.1	4.2±0.1	18.2±0.2	15.5±0.3	0.71±0.06	1.70±0.22
42094	0.25±0.025	16.9±0.1	4.4±0.1	18.8±0.2	16.0±0.3	0.75±0.06	1.70±0.22
42097	0.25±0.025	24.9±0.1	10.6±0.1	31.3±0.2	25.9±0.3	2.03±0.14	1.44±0.13
42098	0.25±0.025	20.6±0.1	6.9±0.1	24.3±0.2	20.7±0.3	1.26±0.09	1.67±0.18
42099	0.25±0.025	22.4±0.2	8.4±0.2	27.3±0.3	22.8±0.4	1.56±0.13	1.53±0.20
37190	0.10±0.01	21.2±0.2	7.4±0.15	27.0±0.3	23.7±0.6	0.64±0.09	0.82±0.18

Shot data and inferred EOS parameters of Ta<sub>2</sub>O<sub>5</sub> aerogel. The columns are arranged as in Table 111.III.

shows that the model predicts the observed local asymptote at approximately six-fold compression for a strong shock. A disagreement exists at the lower pressures ( $\leq$ Mbar) where the experiments exhibit higher compression than predicted by the model. The model's region of high compression, occurring at  $\sim$ 0.10 Mbar, is at much lower shock strength than that found in these experiments.

The shock velocities across the contact surface are used with the impedance-matching technique to derive the kinematic properties of the shock. This procedure is shown in Fig. 111.27 for OMEGA shot 37190. The shock velocity in the quartz just

prior to the shock arrival at the contact surface is 21.2  $\mu\text{m/ns}$  with an uncertainty of  $\sim$ 1% because the contact surface is free of gaps. This yields a Rayleigh line with a slight slope uncertainty. The intersection of the Rayleigh line and its uncertainty lines with the reference Hugoniot (in this case quartz) identifies the release shock state  $P_0$  with its associated uncertainty. The isentropes from  $P_0$  and its uncertainty are calculated for the reflected wave. These isentropes are matched to the Rayleigh line for the aerogel, the product of 0.1 g/cm<sup>3</sup> and 27  $\mu\text{m/ns}$ , with the associated uncertainty in this slope,  $\sim$ 10%. The uncertainties in the final kinematic parameters reported in this study were reported as the larger of the uncertainties in the matched

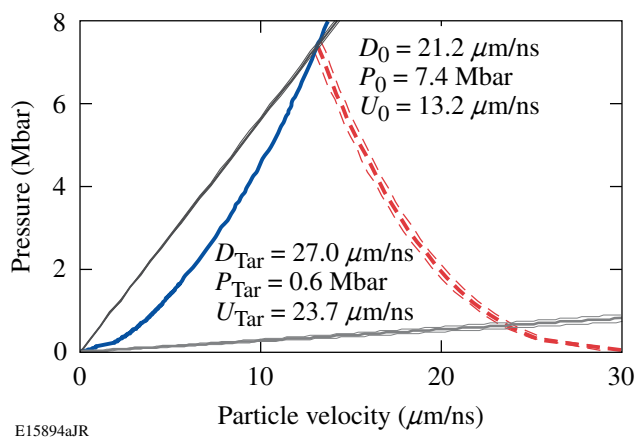


Figure 111.27

Uncertainties in the slopes of the Rayleigh lines were used to determine the uncertainties in the kinematic properties for shot 37190. The uncertainty in the measurement of the shock velocity of the reference standard produces uncertainties in the isentrope (dashed curves), which combines with the uncertainties in the density of the aerogel and shock velocity in the aerogel (thin, light gray curves).

values, i.e.,  $\delta u_p = \max\{\{\delta u_{p-}, \delta u_{p+}\}\}$ ,  $\delta P = \max\{\{\delta P_-, \delta P_+\}\}$ .

#### 4. Thermal Properties of Ta<sub>2</sub>O<sub>5</sub> Aerogel

The streaked optical pyrometer was used to infer the brightness temperature of the shock front. These measurements involved the simultaneous measurement of the shock velocity and its brightness just prior to the shock's arrival at the rear surface. Brightness measurements are acquired just before shock breakout to eliminate uncertainties in the shock-front brightness that might occur due to the scattering or absorption of light within the unshocked target ahead of the shock. The dependence of brightness and shock-velocity measurements are translated to temperature dependence on shock pressure using the NIST-traceable calibration of the SOP<sup>15</sup> and the kinematic measurements discussed in **Kinematic Properties of Ta<sub>2</sub>O<sub>5</sub> Aerogel** (p. 160), respectively. The results for the 0.25-g/cm<sup>3</sup>, Ta<sub>2</sub>O<sub>5</sub> aerogel are shown in Fig. 111.28 along with the prediction by qEOS (solid line). As can be seen in this figure, the qEOS model overpredicts the temperature of the shock front. In the strong-shock limit [temperature ( $T$ )  $\propto$  shock strength ( $P$ )], the slope of the locus of points,  $(\Delta T/\Delta P)_{\text{Hug}}$ , is a few times greater than that of the measured values.

#### Discussion

The measurements of the EOS of the Ta<sub>2</sub>O<sub>5</sub> showed marked differences to the *a priori* qEOS model that has been built for

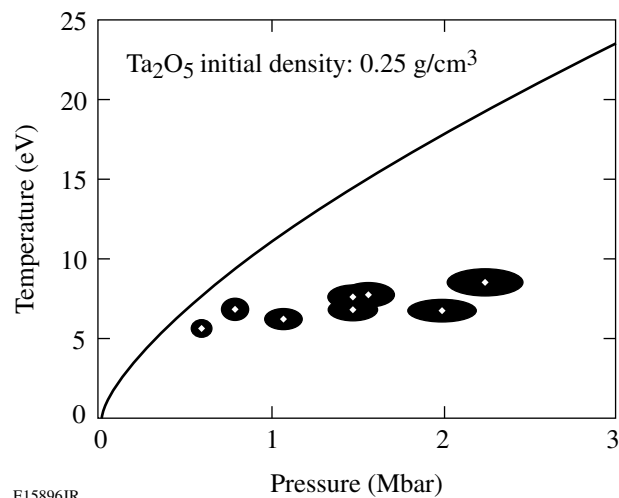


Figure 111.28

The temperature dependence on the shock strength for the 0.25-g/cm<sup>3</sup> aerogel shows that the predicted temperature for qEOS is significantly different than that observed. Above 0.1 Mbar the rise in predicted temperature as the shock strength increases is about three times greater than the observed temperature dependence on shock strength.

the material. It was shown that the qEOS model exhibits very different behavior in the sub-Mbar regime than the measurements. In this shock-strength regime, the qEOS model behavior is much stiffer (small compression for given shock strength) than that observed experimentally. High temperatures with only translational degrees of freedom available would restrict the final compression to this extent, so it is necessary to look at the Ta<sub>2</sub>O<sub>5</sub> molecule to see if there may be neglected degrees of freedom to account for this deviation. While the temperature measurements could be consistent with the higher compressions in experiment (as opposed to those found with qEOS), the temperature's very weak dependence on shock strength suggests consideration of other potential reasons.

In **qEOS Kinematic Agreement** (p. 164), the Ta<sub>2</sub>O<sub>5</sub> aerogel measurements will be compared with SiO<sub>2</sub> aerogel measurements conducted at multiple laboratories. The silica aerogels have a comparable final density to the Ta<sub>2</sub>O<sub>5</sub> aerogels; however, they exhibit marked differences in some of their fundamental properties, namely the binding energy. Due to the finite time required for ionization, the possibility of nonequilibrium between the free electrons and the ions will be considered in **qEOS Thermal Properties** (p. 164). While this nonequilibrium would adversely affect thermal measurements that rely on the local electron temperature near the critical surface of the SOP, it would not affect the kinematic measurements, which

rely on an equilibrium wave that is much less localized.

### 1. qEOS Kinematic Agreement

The shock-strength dependence of the compression for silica aerogel and Ta<sub>2</sub>O<sub>5</sub> is shown in Fig. 111.29. Based on the Ta<sub>2</sub>O<sub>5</sub> response, the Thomas-Fermi-based qEOS model [lines in Fig. 111.29(b)] is in good agreement with the high-pressure, kinematic behavior of Ta<sub>2</sub>O<sub>5</sub>. This agreement begins approximately between 0.75 and 1 Mbar for the three studied aerogel sample densities. The agreement at higher pressure means that sufficient ionization exists to allow the free electrons in the

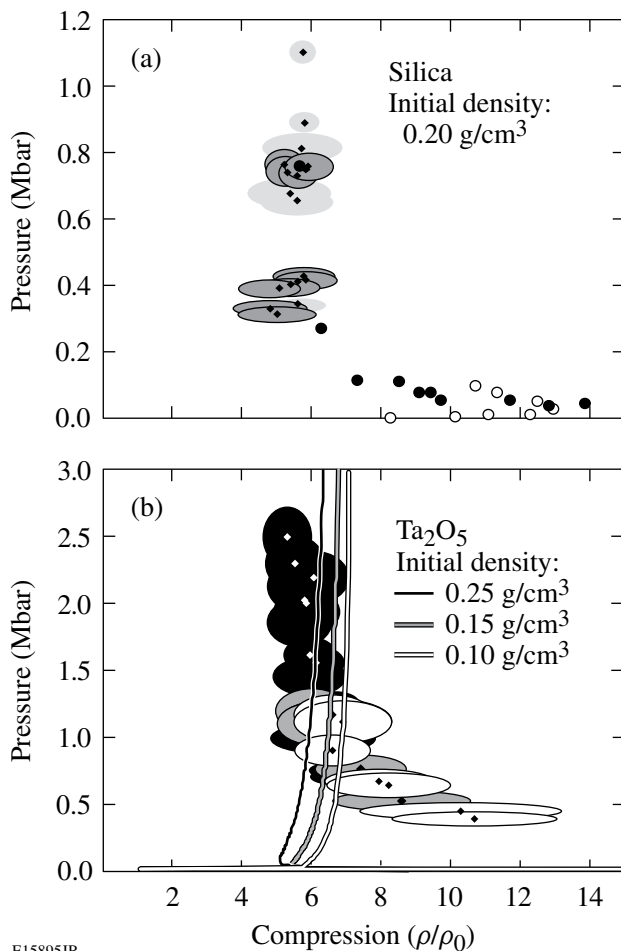
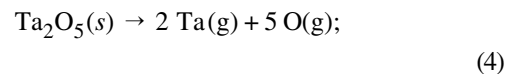


Figure 111.29

These two graphs show the shock-strength dependence of the compression for (a) silica aerogel and (b) the Ta<sub>2</sub>O<sub>5</sub> aerogel. The data and curves in both (a) and (b) exhibit high compressions at low pressures due to molecular contributions to the material compressibility. The molecular contributions become negligible at about 0.3 Mbar in the silica aerogel and at about 0.1 Mbar in the Ta<sub>2</sub>O<sub>5</sub> aerogel. Above these threshold values, the compression is essentially independent of shock strength. The silica data are from Boehly *et al.* (light gray ellipses), Knudson *et al.* (dark gray ellipses), Trunin and Simakov (solid circles), and Vildanov *et al.* (open circles).<sup>13,23–26</sup>

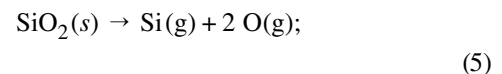
plasma to dominate the kinematic behavior of the background molecules/ions. At low pressure, the difference between the predicted and observed response is large, with predicted compression ratios far lower than those experimentally observed. This behavior indicates that the qEOS model is probably handling the dissociation of the material incorrectly. This is consistent with a reduction in the observed temperature.

When comparing the Ta<sub>2</sub>O<sub>5</sub> aerogel to the silica aerogel, it is clear that there is precedent for this increased compressibility relative to qEOS predictions for these two materials, which are of comparable final density. The main difference between this Ta<sub>2</sub>O<sub>5</sub> study and the studies in the silica aerogel is that the pressure at which the Ta<sub>2</sub>O<sub>5</sub> aerogels exhibit compression independence is about three times higher than that in the silica aerogel. Ta<sub>2</sub>O<sub>5</sub> has a total sublimation/dissociation energy<sup>26</sup> of



$$\Delta H_0 = 1157 \text{ kcal/mol},$$

which is approximately three times larger than that of SiO<sub>2</sub> (Ref. 27):



$$\Delta H_0 = 443 \text{ kcal/mol}.$$

This difference appears to account for the delayed onset of Thomas-Fermi behavior. The Ta<sub>2</sub>O<sub>5</sub> remains more compressible because these molecular structures provide an increased compressibility through the additional degrees of freedom and higher energy consumption to break the bonds.

### 2. qEOS Thermal Properties

The disagreement between the qEOS model and the temperature measurements in **Thermal Properties of Ta<sub>2</sub>O<sub>5</sub> Aerogel** (p. 163) is pronounced. The kinematic results indicate that the Ta<sub>2</sub>O<sub>5</sub> material can absorb more energy than predicted by the qEOS model. The apparent independence of the measured temperature on the pressure suggests that local, nonequilibrium processes may also be important. Studies of other material have indicated that at sufficiently high pressures the brightness/temperature measurements in alkali halides (NaCl, KCl, and KBr) approached a similar plateau where the observed temperature became nearly constant with shock strength.<sup>28</sup> An explanation for these observations based on a lack of equilibrium between electrons and the atoms just behind

the shock front was provided by Zeldovich.<sup>29</sup> Zeldovich argued that the energy of a shock wave is carried by the atoms and transferred (via collisions) to the electrons; thus, full equilibrium depends on the rate of electron–ion collisions. In most crystalline materials, the collision frequency is sufficiently high that equilibration occurs on a subpicosecond time scale. If the shock speed is sufficiently high and the collision rates are moderate, then equilibration can lag significantly behind the shock-wave front. This would result in the electron temperature being lower than the ion temperature until deep into the shock front. As the electron temperature is equilibrating, ionization is taking place, resulting in an increase in electron density as a function of position within the shock. Consequently, if the critical surface of a pyrometer channel is closer to the observer than the equilibrium temperature, then the brightness temperature, which is predominantly related to bound-free and free-free electronic transitions, would be artificially low.

To determine if these aerogels exhibit this nonequilibrium behavior, a simulation of the experiment was performed using the one-dimensional hydrodynamics code HYDRA.<sup>30</sup> In this simulation, a  $0.1\text{-g/cm}^3$  sample of  $Yb_2O_5$  was shocked by a quartz pusher in the same configuration as shown in Fig. 111.24. It should be noted that ytterbium (Yb) was used as a surrogate for Ta because opacity tables for Ta were unavailable at the time of the simulation. The simulated drive environment was identical to that used in OMEGA shot 37190. Figure 111.30(a) shows the predicted electron density ( $n_e/n_c$ ) as a function of the one-dimensional spatial coordinate in the simulation. The density is normalized to the critical density for the band of the SOP centered at 1.84 eV. Figure 111.30(b) shows the temperature of the electrons (dotted) and the ions (solid) as a function of the one-dimensional spatial coordinate in the simulation. As with density, the temperature is normalized to the electron temperature at the critical surface for the SOP measurement wavelength. These snapshots are from 7 ns after the laser pulse began and spatially referenced to the front surface of the ablator. In the density plot looking from left to right, the high-density shocked region, at positions less than  $141\ \mu\text{m}$ , is the advancing quartz pusher. The density gradient between  $141$  and  $142\ \mu\text{m}$  is due to the release of the high-density quartz into the lower-density, shocked aerogel. The measured shock-wave front is at approximately  $145\ \mu\text{m}$  and is a little over  $500\ \text{nm}$  thick. Ahead of the shock wave is a region where the radiation from the shock is ionizing some of the atoms in the unshocked material to  $\sim 4\%$  of the equilibrium electron density of the shocked material. In the temperature plot, one can see the corresponding features behind the shock front. As one approaches the shock front, significant deviations

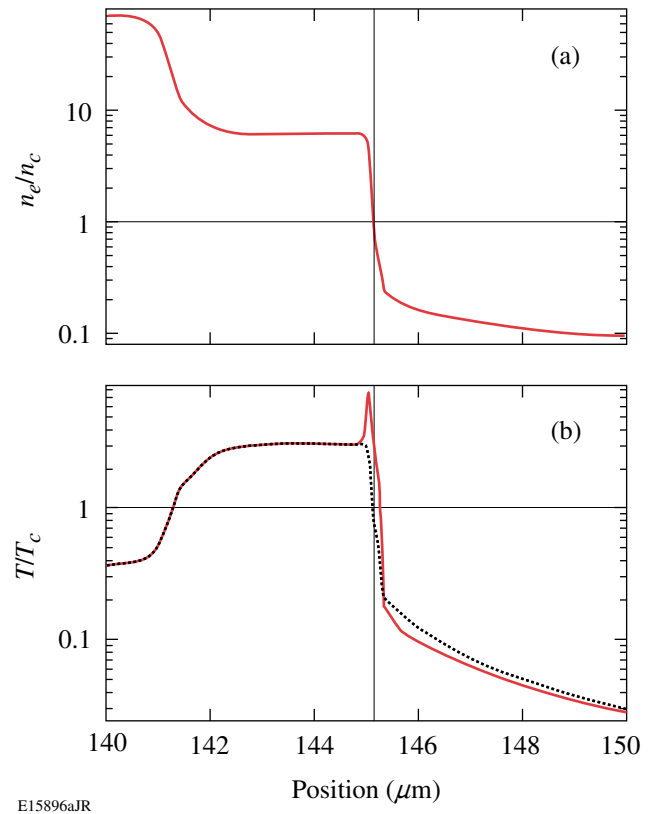


Figure 111.30

The electron density in the vicinity of the shock front (a) normalized to the critical density of the pyrometer's band center, 670 nm, and (b) the temperature of the electrons (dotted) and the ions (solid) in the vicinity of the shock front normalized to the electron temperature at the SOP's critical surface. In the position coordinate, up to  $141\ \mu\text{m}$ , the material is quartz, while from  $142\ \mu\text{m}$  and beyond, the material is the  $Yb_2O_5$  aerogel. Between  $141$  and  $142\ \mu\text{m}$ , the quartz is releasing into the less-dense aerogel. From about  $145\ \mu\text{m}$  and beyond, the shock wave has not yet arrived; however, radiation from the shock front is ionizing and heating the nearby material in advance of the arrival of the shock. The actual shock front arrives at about  $145\ \mu\text{m}$  and rapidly heats the ions. The electrons come into equilibrium with the ions at about  $0.5\ \mu\text{m}$  behind the shock front.

occur between the electron and ion temperatures. The leading edge of the shock front transfers energy to the ions by ion–ion collisions, heating them very rapidly to a level above the final equilibrium value. The electron–ion collision cross section is much smaller; therefore the energy transfer to the electrons is much slower and lags behind the shock front.

The simulation indicates that the critical electron density for the measurement wavelength is achieved at a point ahead of where the electrons and the ions come into full equilibrium. Therefore, the measurement would exhibit lower temperatures than that produced by the shock wave. The most reasonable method to overcome this skin-depth issue is to observe the

shock at shorter wavelengths (i.e., at higher critical frequencies). For example, this simulation indicates that a 200-nm pyrometer would likely make an accurate measurement of the shock temperature.

## Conclusions

This study provided experimental EOS data of highly porous  $Ta_2O_5$  aerogels. Using the OMEGA Laser System, aerogel samples were compressed from their initial densities of 0.1, 0.15, and 0.25 g/cm<sup>3</sup> by shock waves with strengths between 0.3 and 3 Mbar. Under these shock loads, the materials were compressed to densities between 5 and 15 times their initial density and to temperatures  $\geq 50,000$  K. The shocked states as diagnosed with the VISAR and the SOP show strong deviations from the available qEOS model for this material. When the compression measurements are compared to qEOS, it is found that the model underestimates the level of compression achieved by shock loading below 1 Mbar but reproduces the material behavior above 1 Mbar. This observation indicates that there are material degrees of freedom below 1 Mbar that are not fully captured by the qEOS model. The thermal measurements indicate that this might be due to less-significant heating; however, the weak dependence of temperature on shock strength could indicate that nonequilibrium effects require more attention when considering aerogel materials.

## ACKNOWLEDGMENT

This work was supported by the U.S. Department of Energy Office of Inertial Confinement Fusion under Cooperative Agreement No. DE-FC52-92SF19460, the University of Rochester, and the New York State Energy Research and Development Authority. The support of DOE does not constitute an endorsement by DOE of the views expressed in this article.

## REFERENCES

- R. Cauble *et al.*, *Astrophys. J. Suppl. Ser.* **127**, 267 (2000).
- G. W. Collins *et al.*, *Science* **281**, 1178 (1998).
- M. Koenig *et al.*, *Appl. Phys. Lett.* **72**, 1033 (1998).
- P. M. Celliers *et al.*, *Phys. Plasmas* **11**, L41 (2004).
- D. K. Bradley *et al.*, *Phys. Rev. Lett.* **93**, 195506 (2004).
- D. G. Hicks, T. R. Boehly, P. M. Celliers, J. H. Eggert, E. Vianello, D. D. Meyerhofer, and G. W. Collins, *Phys. Plasmas* **12**, 082702 (2005).
- D. G. Hicks, T. R. Boehly, J. H. Eggert, J. E. Miller, P. M. Celliers, and G. W. Collins, *Phys. Rev. Lett.* **97**, 025502 (2006).
- R. Cauble *et al.*, *Phys. Rev. Lett.* **80**, 1248 (1998).
- M. D. Knudson *et al.*, *Phys. Rev. Lett.* **87**, 225501 (2001).
- L. V. Al'tshuler, *Sov. Phys.-Usp.* **8**, 52 (1965).
- C. A. Back *et al.*, *Phys. Plasmas* **7**, 2126 (2000).
- R. P. Drake, *High-Energy-Density Physics: Fundamentals, Inertial Fusion, and Experimental Astrophysics*, Shock Wave and High Pressure Phenomena (Springer, Berlin, 2006).
- T. R. Boehly, R. S. Craxton, T. H. Hinterman, J. H. Kelly, T. J. Kessler, S. A. Kumpan, S. A. Letzring, R. L. McCrory, S. F. B. Morse, W. Seka, S. Skupsky, J. M. Soures, and C. P. Verdon, *Rev. Sci. Instrum.* **66**, 508 (1995).
- P. M. Celliers, D. K. Bradley, G. W. Collins, D. G. Hicks, T. R. Boehly, and W. J. Armstrong, *Rev. Sci. Instrum.* **75**, 4916 (2004).
- J. E. Miller, T. R. Boehly, A. Melchior, D. D. Meyerhofer, P. M. Celliers, J. H. Eggert, D. G. Hicks, C. M. Sorce, J. A. Oertel, and P. M. Emmel, *Rev. Sci. Instrum.* **78**, 034903 (2007).
- Y. Lin, T. J. Kessler, and G. N. Lawrence, *Opt. Lett.* **20**, 764 (1995).
- T. F. Baumann *et al.*, in *Handbook of Porous Solids*, edited by F. Schüth, K. S. W. Sing, and J. Weitkamp (Wiley-VCH, Weinheim, Germany, 2002), p. 2014.
- P. Wang *et al.*, *J. Phys. D: Appl. Phys.* **27**, 414 (1994).
- A. G. Van Engen, S. A. Diddams, and T. S. Clement, *Appl. Opt.* **37**, 5679 (1998).
- Zygo NewView™ 5000, Zygo Corporation, Middlefield, CT 06455.
- E. Hecht, *Optics*, 4th ed. (Addison-Wesley, Reading, MA, 2002).
- Computrac Max-1000 moisture analyzer, Arizona Instruments, Phoenix, AZ 85040-1941.
- T. R. Boehly, J. E. Miller, D. D. Meyerhofer, J. G. Eggert, P. M. Celliers, D. G. Hicks, and G. W. Collins, "Measurement of Release of Alpha Quartz: A New Standard for Impedance-Matching Experiments," submitted to the Proceedings of the APS.
- M. D. Knudson, J. R. Asay, and C. Deeney, *J. Appl. Phys.* **97**, 073514 (2005).
- G. V. Simakov and R. F. Trunin, *Izv. Akad. Nauk SSSR Fiz. Zemli* (11), 72 (1990).
- V. G. Vildanov *et al.*, in *Shock Compression of Condensed Matter '95, AIP Conference Proceedings 370*, edited by S. C. Schmidt and W. C. Teo (American Institute of Physics, Melville, NY, 1996), pp. 121–124.
- M. G. Inghram, W. A. Chupka, and J. Berkowitz, *J. Chem. Phys.* **27**, 569 (1957).
- J. D. Cox, D. D. Wagman, and V. A. Medvedev, *CODATA Key Values for Thermodynamics* (Hemisphere, New York, 1989).
- S. B. Kormer, *Sov. Phys.-Usp.* **11**, 229 (1968).
- S. B. Kormer, M. V. Sinitsyn, and A. I. Kuryapin, *Sov. Phys.-JETP* **28**, 852 (1969); Ya. B. Zel'dovich, S. B. Kormer, and V. D. Urlin, *Sov. Phys.-JETP* **28**, 855 (1969).

---

# EXAFS Measurements of Quasi-Isentropically Compressed Vanadium Targets on the OMEGA Laser

## Introduction

The response of materials to shocks and other high-strain-rate deformation is the subject of intense research.<sup>1</sup> There is particular interest in developing and testing constitutive models that allow continuum hydrodynamic computer codes to simulate plastic flow in the solid state. Such models are important for the study of material strength under high-strain and high-strain-rate conditions. To test such models, the conditions within the compressed samples (such as compression and temperature) must be measured on a nanosecond time scale. We describe experiments on the OMEGA<sup>2</sup> laser where vanadium (V) is compressed quasi-isentropically to a pressure of  $\sim 0.75$  Mbar and its compression and temperature are measured by Extended X-Ray Absorption Fine Structure (EXAFS).<sup>3</sup> Isentropic compression (where the entropy is kept constant) enables us to reach high compressions at relatively low temperatures. This is important for the study of highly compressed metals at temperatures well below the melting point. Additionally, significant EXAFS modulations can be obtained only at sufficiently low temperatures. The study of deformations and crystal phase transformations of compressed metals requires that the temperature be kept below melting. This limits the pressure that can be applied in shock compression. Examining the Hugoniot curve that describes the trajectory of shocks in parameter space shows that vanadium will melt<sup>4</sup> at a pressure of  $\sim 2.4$  Mbar (and a temperature of  $\sim 8000$  K), precluding solid-state studies at higher pressures. However, quasi-isentropic compression experiments (ICE), involving a slower-rising compression, can access much higher pressures and still stay below the melting curve. Laser-driven quasi-isentropic compression can be achieved by a two-stage target design<sup>5</sup> where a laser of a few-nanosecond pulse irradiates a “reservoir” layer. When the laser-generated shock wave reaches the back of the reservoir, the material releases and flows across a vacuum gap and stagnates against the sample (“plasma impact”), causing its pressure to rise over a period of a few tens of nanoseconds. This configuration has been previously studied and pressures of up to 2 Mbar demonstrated.<sup>6–8</sup> The main diagnostic in those experiments was the interferometric measurement of the back target surface, which, when back-integrated (in time and space), can yield the

pressure on the front surface as a function of time. EXAFS has the unique advantage of yielding information on the sample temperature. This is particularly important to measure because the stagnating reservoir material causes severe heating of the front sample surface, unless protected by a heat shield. The ability to measure temperatures of the order of  $10^3$  K is unique to EXAFS, as is the ability to *directly* measure compression and temperature within the sample. The EXAFS results show details not seen in the VISAR results: without the use of a heat shield, the heating of the target leads to a lower compression. Also, higher laser intensities can lead to nonuniformities due probably to hydrodynamic instability.

The use of *in-situ* EXAFS for characterizing nanosecond laser-shocked vanadium, titanium, and iron has been recently demonstrated.<sup>9,10</sup> Additionally, the observed EXAFS was shown to indicate crystal phase transformation due to shock compression: the  $\alpha$ -to- $\omega$  transformation in titanium<sup>9</sup> and the body-centered-cubic (bcc) to hexagonal-closely-packed (hcp) phase transformation in iron.<sup>10</sup> We show here that EXAFS can likewise be applied to the case of laser-driven, quasi-isentropic compression experiments (ICE).

EXAFS modulations above an absorption edge are due to the interference of the ejected photoelectron wave with the reflected wave from neighboring atoms.<sup>3</sup> This interference translates into modulations in the cross section for photon absorption above the K edge, the measured quantity. The frequency of these modulations relates to the interparticle distance, hence the density of the compressed material. The decay rate of the modulation with increasing photoelectron energy yields the mean-square relative displacement ( $\sigma$ ) of the crystal atoms and serves as a temperature diagnostic. The basic theory of EXAFS<sup>3</sup> yields an expression for the relative absorption  $\chi(k) = \mu(k)/\mu_0(k) - 1$ , where  $\mu(k)$  is the absorption coefficient and  $\mu_0(k)$  is the absorption of the isolated atom. The wave number  $k$  of the ejected photoelectron is given by the de Broglie relation  $\hbar^2 k^2 / 2m = E - E_K$ , where  $E$  is the absorbed photon energy and  $E_K$  is the energy of the K edge. The measured spectrum yields the absorption  $\mu(E)$ , which is converted

to  $\chi(k)$ . The derived  $\chi(k)$  is analyzed with the FEFF *ab initio* EXAFS software package.<sup>11</sup> The basic EXAFS formula for a single reflection in the plane-wave approximation is<sup>3</sup>

$$\chi(k) = \sum_j N_j S_0^2 F_j(k) \exp\left[-2\sigma^2 k^2 - 2R_j/\lambda(k)\right] \times \sin\left[2kR_j + \phi_j(k)\right]/kR_j^2, \quad (1)$$

where  $N_j$  is the number of atoms in the  $j$ -th shell, that is, the number of atoms surrounding the absorbing atom at a distance  $R_j$ , and  $\lambda(k)$  is the mean free path for collisions. FEFF uses the scattering potential to calculate the amplitude and phase shift of the photoelectron waves scattered from several shells of neighboring atoms including multiple scattering paths. The total  $\chi(k)$  is constructed in the curved-wave approximation (i.e., the assumption of plane wave is removed) and iteratively fitted to the experimental  $\chi(k)$ . The main fitting parameters are the nearest-neighbor distance  $R$  and the vibration amplitude  $\sigma^2$  appearing in the Debye–Waller term.  $R$  yields the density or compression; since  $R$  is the frequency of the modulations in  $k$  space, a compression results in the lengthening of the period of EXAFS modulations (a similar lengthening will also be evident in the photon-energy space, i.e., in the original spectrum). As a function of temperature,  $\sigma^2$  was calculated using the Debye model<sup>12</sup> for the phonon density of states, including correlation, and it also depends on the density through the Debye temperature. Using the density dependence<sup>13</sup> of the Debye temperature for V and the result for  $\sigma^2$  from the FEFF fitting, the temperature can be derived. As the temperature increases, the EXAFS oscillations decay faster with increasing photon energy (or increasing electron wave number).

The use of EXAFS for diagnosing compressed metals places a severe restriction on the temperature since at higher temperatures the damping of the EXAFS modulations (because of an increase in  $\sigma^2$ ) may preclude reliable measurement. A useful general criterion for the observation of significant EXAFS modulations is the requirement for  $\sigma^2$  to not exceed  $\sim 0.015 \text{ \AA}^2$ . The averaged square vibration amplitude  $\sigma^2$  increases with the temperature, but compression mitigates this increase because the Debye temperature increases with density. At normal density the temperature  $T_0$  of vanadium at which  $\sigma^2 = 0.015 \text{ \AA}^2$  is  $T_0 \sim 500 \text{ K}$ , whereas at a compression of 1.5 that temperature increases to  $T_0 \sim 1800 \text{ K}$ . Thus, compression extends the range of temperatures where EXAFS can be observed. This compression, when achieved by a shock [at a pressure of  $\sim 1.8 \text{ Mbar}$  (Ref. 14)], will result in a temperature of  $\sim 5000 \text{ K}$ , much higher

than  $T_0$ . Thus, in spite of the compression, significant EXAFS modulations would not be visible in that case. On the other hand, an examination of the equation of state of vanadium<sup>15</sup> shows that in a purely isentropic compression, the temperature corresponding to 1.8 Mbar will rise to only  $\sim 530 \text{ K}$ . Thus, in future ICE experiments, even if not purely isentropic, EXAFS could be measured at pressures of several Mbar and possibly higher.

The drive (i.e., the pressure as a function of time at the front surface of the sample) is calibrated by substituting aluminum for the vanadium; this pressure is independent of the material of the sample. The drive pressure is deduced, for various laser intensities, by interferometrically measuring the velocity of the back target surface (VISAR<sup>16</sup>) as a function of time and then integrating it backward in time and space to obtain the drive.<sup>17</sup> Aluminum is used because its equation of state is well known, and LiF is used because it is transparent to the VISAR laser and its acoustical impedance is well matched to that of aluminum, minimizing reflections at the interface. The behavior of the total target (reservoir, vacuum gap, and sample) is simulated by the hydrodynamic code *LASNEX*.<sup>18</sup> The code results are compared with both the measured back-surface velocity as well as the drive pressure obtained as explained above. Good agreement validates the use of such simulations for the case of the vanadium sample. The *LASNEX*-simulated compression and temperature within the vanadium can be compared with the EXAFS results.

In addition to the inevitable heating due to the compression, there are three sources of extraneous heating (called here preheat): (a) radiation from the imploding target (the radiation source, or the backlighter), (b) radiation from the laser-drive absorption region, and (c) heat generated from the plasma impact upon stagnation and conducted into the sample. The first preheating occurs during the EXAFS probing, whereas the other two occur before the onset of sample compression. Ways to measure as well as to minimize these heating sources are described below.

The present work demonstrates the feasibility and finds the limitations of laser-driven quasi-isentropic compression experiments, rather than carrying out a systematic parameter study. Typical results will highlight these limitations.

The following sections of this article (1) explain the experimental setup and procedures; (2) present the VISAR results and their analysis; (3) present the special case of high-irradiance, which leads to nonuniform compression; (4) analyze the role of the heat shield; (5) discuss the measurement of preheat;

and (6) present the EXAFS measurements of compression and heating.

### Experimental

Figure 111.31 shows a schematic of the experimental configuration used to measure K-edge EXAFS absorption spectra. The target consisted of two parts: a reservoir and a sample (V or Al), separated by a vacuum gap of either 300 or 400  $\mu\text{m}$ . The reservoir includes an undoped, 125- $\mu\text{m}$ -thick polyimide layer and a 50- $\mu\text{m}$ -thick CH layer, doped with 2% (by number of atoms) of bromine. The bromine minimizes the sample heating by radiation from the laser-absorption region. The doping is limited to only the back of the reservoir to prevent laser heating of the doped layer, which would have increased the emitted radiation, and thus the preheating. The doping concentration is limited to minimize the absorption of source radiation within the reservoir, which reduces the intensity available for the EXAFS measurement. The sample (10- $\mu\text{m}$ -thick polycrystalline V) was coated on the laser side with 8  $\mu\text{m}$  of a low-conduction parylene-N heat shield. Its role is to protect the sample from heat conducted from its surface, where the reservoir plasma impact occurs. On some of the shots the heat shield was absent in order to demonstrate its effect. The V sample was backed by a 500- $\mu\text{m}$ -thick  $\text{C}_2\text{H}_4$  substrate, which served to minimize sample heating by the soft radiation from the imploding EXAFS source. This radiation shield also prevents rarefaction of the sample when the pressure wave arrives at its rear surface. The thickness of the radiation shield was chosen to heavily absorb the radiation below the vanadium K edge (5.463 keV) while absorbing only slightly the radiation above

the K edge, where the EXAFS modulations occur. To further minimize this preheat, the target-backlighter distance (19 mm) was the largest possible on OMEGA. As explained before, in the VISAR drive-calibration shots, the V was replaced by Al and the radiation shield was changed to LiF. The rest of the targets were identical to that with the vanadium sample. For the calibration shots there is no backlighter and the VISAR laser travels from the right in Fig. 111.31.

Eleven driving laser beams, 3-ns square pulse each, were fired simultaneously and focused to an  $\sim 3$ -mm focal spot, yielding an irradiance of  $\sim 17 \text{ TW}/\text{cm}^2$  (some results for different irradiances are mentioned below). The x-ray spectrum is obtained when a fan of rays originating at the backlighter fall on the flat crystal at different Bragg angles, reflecting a slightly different wavelength at each point. The spectral range of the EXAFS spectrum ( $\sim 5.5$  to 6 keV) subtends a distance of  $\sim 0.5$  mm at the target. A 3-mm-focal-spot size was chosen so that the EXAFS rays probe a small central region of the focal spot. This necessitates working without distributed phase plates (DPP's),<sup>19</sup> which create intensity nonuniformity in the focal spot. Some of this nonuniformity is smoothed out when the reservoir material flows across the vacuum gap (as will be shown in Fig. 111.33) for the uniformity of the back-surface motion. Specially designed phase plates for an  $\sim 3$ -mm focal-spot size could improve the quality of these experiments. The spectral resolution (limited by the size of the imploded backlighter core) is  $\sim 10$  eV, much smaller than a typical EXAFS modulation period.

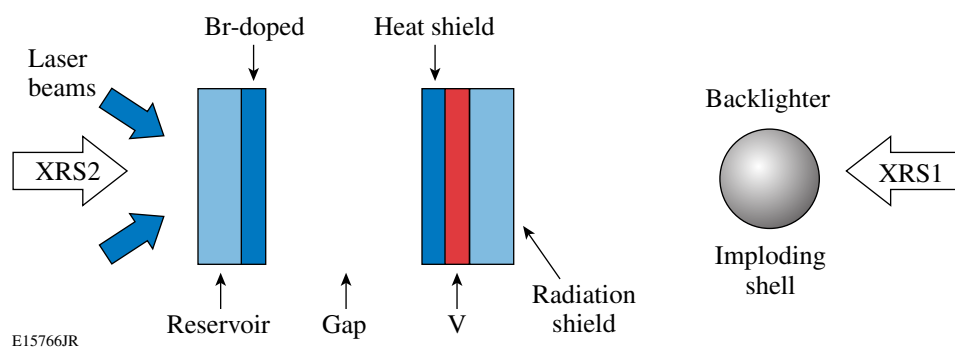
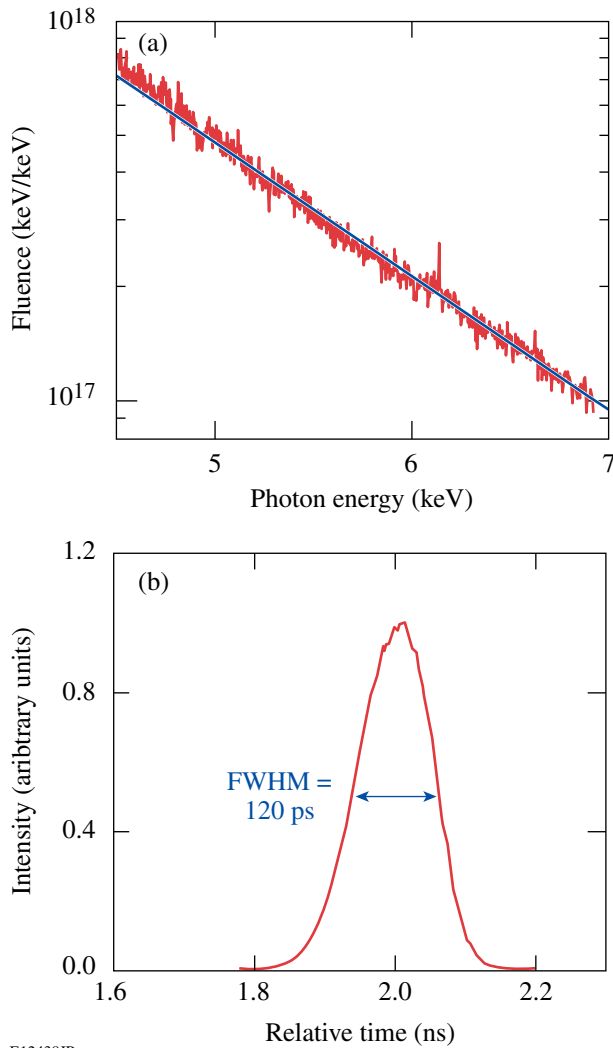


Figure 111.31

Schematic of the experimental configuration for EXAFS measurement of ICE targets. For calibrating the drive, the V is replaced by Al and the radiation shield by LiF, the backlighter is removed, and the VISAR laser travels from right to left. XRS1 and XRS2 are x-ray spectrometers that measure, respectively, the incident and transmitted spectra. The Br doping reduces heating due to radiation from the laser-deposition region, the heat shield reduces heating due to the impact of reservoir material on the sample, and the radiation shield reduces heating due to the backlighter.

The backlighter is formed by focusing 40 of the OMEGA beams on a CH shell of  $\sim 16\text{-}\mu\text{m}$  thickness and  $\sim 850\text{-}\mu\text{m}$  outer diameter, filled with 0.1 atm of argon, using a 1-ns square pulse. At peak compression the compressed core of the target ( $<100\ \mu\text{m}$  in size) emits an intense continuum that is spectrally smooth [see Fig. 111.32(a)]; this is a requisite for measuring the inherently weak modulations in the absorption spectrum. Two cross-calibrated, flat-crystal spectrometers equipped with a Ge (1,1,1) crystal were placed at the extreme right and left positions in Fig. 111.31. The first was used to measure the inci-



E12438JR

Figure 111.32

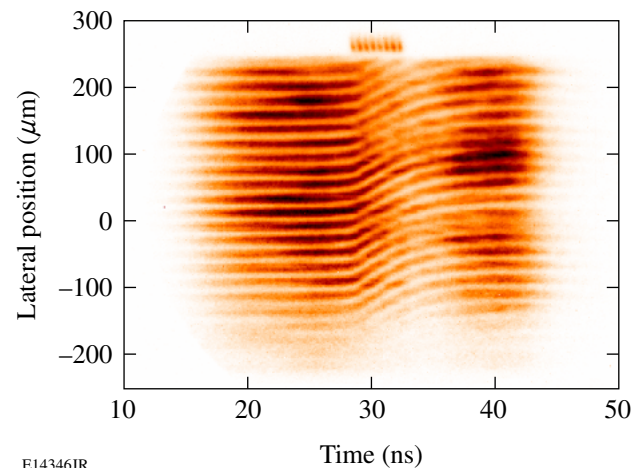
(a) Typical spectrum emitted by the backlighter, used as a source for the measurement of absorption above the vanadium K-shell edge at 5.46 keV. The use of imploding CH shells creates a continuum without spectral lines, essential for reliable EXAFS measurements. (b) Streaked x-ray emission from the imploding backlighter target. Radiation above  $\sim 3$  keV is emitted during peak compression (earlier emission is negligibly small), ensuring a short x-ray probing pulse.

dent spectrum ( $I_0$ ) and the second to measure the transmitted spectrum ( $I$ ). The absorption as a function of photon energy  $E$  is defined as  $\mu(E) = \ln[I_0(E)/I(E)]$ .  $I_0$  has to be corrected for the (known) absorption of backlighter radiation in the radiation shield. Absorption of the transmitted radiation ( $I$ ) in the reservoir is small, and, additionally, at the time of EXAFS probing, most of the reservoir material has been ablated away. The measured intensity also includes radiation from the laser-deposition region, which is subtracted. To measure this contribution (typically,  $\sim 10\%$  of the total), we fire the drive beams without irradiating the backlighter. A final adjustment of  $I_0/I$  can be done far above the K edge, where EXAFS modulations are heavily damped and the absorption  $\mu_0(E)$  is well known. The delay time of the drive beams with respect to the backlighter beams was varied so that the EXAFS could probe the vanadium at different times during the compression. Although the spectrometers used in the EXAFS measurement are time integrated, a meaningful shock diagnosis can be obtained without streaking the spectrum in time because the x-ray pulse width [Fig. 111.32(b)] is only  $\sim 120$  ps, much shorter than the compression-wave transit time through the metal ( $\sim 20$  ns).

## Results and Analysis

### 1. VISAR Results

Figure 111.33 shows a typical VISAR record for the case of an ICE target without a heat shield, driven at  $17\ \text{TW}/\text{cm}^2$ . The time refers to the delay with respect to firing the drive-laser beams; a timing fiducial is shown above the VISAR record. The



E14346JR

Figure 111.33

VISAR record for the case of an ICE target without a heat shield, driven at  $17\ \text{TW}/\text{cm}^2$ . The time refers to the delay with respect to firing the drive-laser beams; a timing fiducial is shown above the VISAR record. The fringe motion tracks the Al particle motion at the reflective Al-LiF interface. The smooth, gradual fringe shift with time is indicative of shockless, quasi-isentropic compression.

fringes are produced by the interference of the VISAR laser with the beam reflected from the back surface of the target. The vertical displacement of fringes is proportional to the Al particle velocity at the Al–LiF interface. The velocity results reported here refer to a spatial average over the 150- $\mu\text{m}$  central portion of the field of view. The smooth, gradual fringe shift with time indicates shockless, quasi-isentropic compression. The relative uniformity (or planarity) of the drive is evidenced by the quasi-simultaneous arrival of the pressure wave (at  $\sim 30$  ns) and the small variations ( $\pm 10\%$ ) in the slope of the fringes (i.e., the acceleration). This uniformity is achieved even though no smoothing was applied to the incident laser beams; nonuniformities in the laser irradiation are smoothed during the propagation through the target vacuum gap, leading to a more-uniform back-surface velocity.

The analysis of VISAR records, such as that in Fig. 111.33, proceeds in two directions: by back-integrating the VISAR-measured velocity and by comparing with 1-D simulations of the *LASNEX* code. Normally, the back-surface velocity is used to derive the front-surface pressure, which is then used as input to a hydrodynamic code. The code then simulates the forward propagation whose end result is the back-surface velocity. This derived velocity is, in turn, compared with the measured velocity. This procedure cannot yield any information on the heating due to the three preheat sources mentioned above. *LASNEX* is used to simulate the entire experiment, starting with the laser interaction, the reservoir expansion, and the sample compression. Because of the resulting complexity, the application of *LASNEX* requires some adjustments to fit the data. This is thought to be due to 2-D effects that are neglected in these 1-D runs (primarily related to the nonuniformities of the unsmoothed beams) as well as uncertainties in the equation of state of the expanding reservoir plasma. Our confidence in the validity of the simulations depends on their agreement with both the measured back-surface velocity as well as the deduced front-surface pressure. Additionally, the code simulations are compared with the EXAFS results.

A sample of such an analysis of VISAR results (Fig. 111.34) shows the rear-surface velocity (upper frames) and the drive pressure (lower frames) for three different cases: irradiance of (a) 17 TW/cm<sup>2</sup>, (b) 17 TW/cm<sup>2</sup> with no Br in the ablator, and (c) 10 TW/cm<sup>2</sup>. In (a) and (c) the reservoir contained a brominated layer; in (b) the brominated layer was replaced with an equal-thickness CH layer. The vacuum gap was 400  $\mu\text{m}$ . The solid curves show simulation results by the *LASNEX* code; the dashed curves show experimental results. The dashed velocity curves are directly from the VISAR-measured results; the

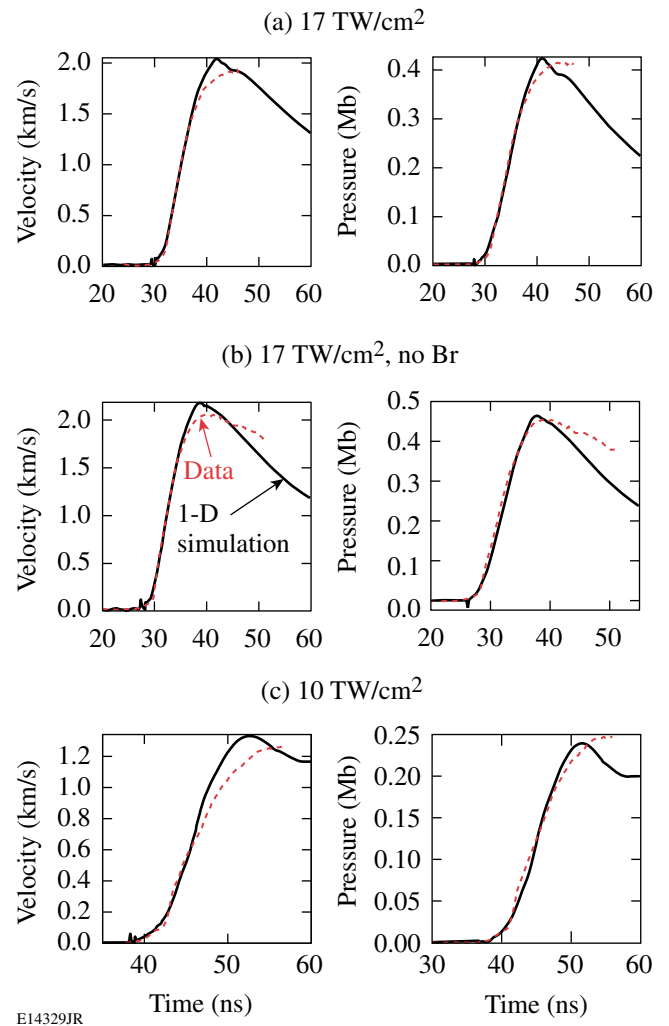


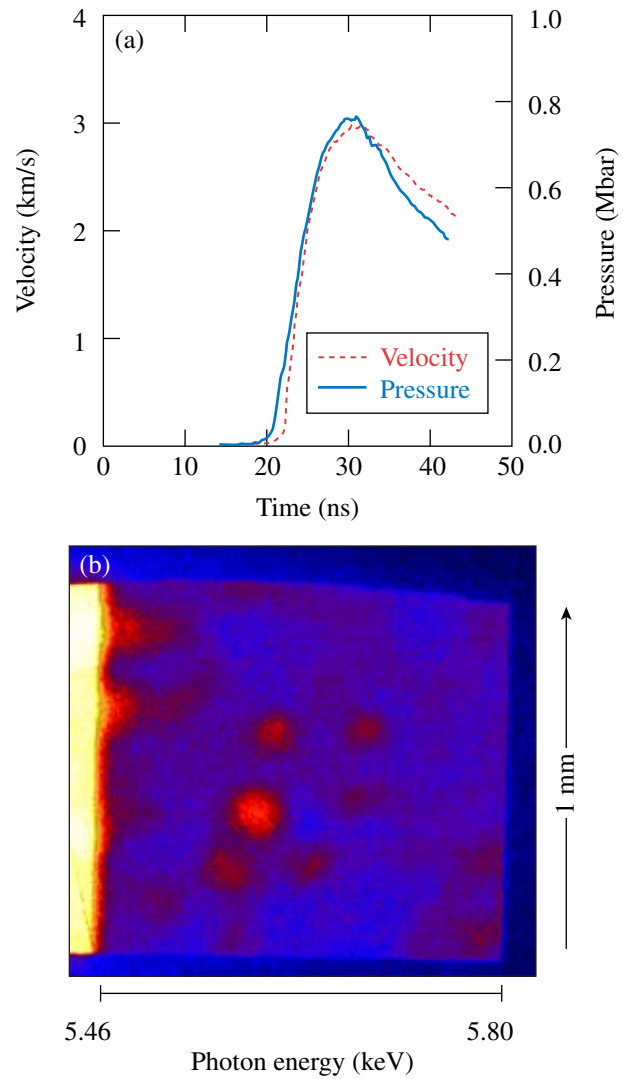
Figure 111.34 Rear-surface velocity (left column) and drive pressure (right column) for three different cases: irradiance of (a) 17 TW/cm<sup>2</sup>, (b) 17 TW/cm<sup>2</sup> (no Br), and (c) 10 TW/cm<sup>2</sup>. The solid curves show simulation results by the *LASNEX* code. The dashed velocity curves (upper) show the VISAR-measured results; the dashed pressure curves (lower) are obtained from the measured velocity curves by back-integration. The rise in velocity and pressure is seen to be slow and smooth, characteristic of shockless compression.

dashed pressure curves are obtained from the measured velocity curves by back-integration.<sup>17</sup> A heat shield was not used in any of these cases. The rise in velocity and pressure is seen to be slow and smooth, characteristic of shockless compression. The small differences between the code and experimental results around peak compression and later are not well understood; similar disagreements with 1-D simulations were also observed in ICE results reported in Fig. 7(b) of Ref. 5. To obtain the velocity fits in Fig. 111.34, two small adjustments had to be introduced in the *LASNEX* runs (no additional adjustments

had to be made to fit the pressure curves): (a) the assumed laser power had to be reduced by  $\sim 30\%$  from the measured values to fit the magnitude of the velocity curve; this is due to the reduction in absorption due to the oblique incidence of the laser beams, and (b) the time scale had to be shifted by a few nanoseconds to fit the time of peak velocity. Nevertheless, the code simulations provide strong support for the VISAR measurements of velocity and pressure as well as the compression and temperature measurements by EXAFS. This is because the main interest here is understanding the sample compression, whereas the interaction of the laser with the reservoir is of secondary importance. Figure 111.34 shows that the inclusion of Br doping slightly reduces the pressure achieved. Examination of the simulations shows that this is caused by the weakening of the compression pressure: the shock traveling within the reservoir weakens when passing from the polyimide to the less-dense CH(Br) layer, then further weakens when traveling through the latter layer. Thus, the total weakening is higher for a thicker CH(Br) layer.

## 2. High-Irradiance Target Experiments

The laser irradiance for most of the target experiments described in this article was  $17 \text{ TW/cm}^2$  for which the achieved pressure was  $\sim 0.4 \text{ Mbar}$  (see Fig. 111.34). At the higher irradiance of  $25 \text{ TW/cm}^2$ , the VISAR results indicate a pressure of  $0.75 \text{ Mbar}$ . However, significant target nonuniformities are indicated in the EXAFS record, at irradiances above  $\sim 22 \text{ TW/cm}^2$ . This precludes meaningful EXAFS analysis. Figure 111.35(a) shows the VISAR-measured velocity and the deduced pressure evolution for a  $400\text{-}\mu\text{m}$ -vacuum-gap target, without a heat shield, and a laser irradiance of  $25 \text{ TW/cm}^2$ . Figure 111.35(b) shows the EXAFS record for a target experiment at the same conditions. The horizontal axis corresponds to the dispersed photon energies (the K edge is seen at  $5.46 \text{ keV}$ ), whereas the vertical axis corresponds to a one-dimensional image (or face-on radiograph) of the vanadium layer. The energy range shown ( $\sim 5.4$  to  $5.8 \text{ keV}$ ) is where the EXAFS modulations are normally seen. The horizontal axis also corresponds to a face-on radiograph of the vanadium sample, except that at each horizontal position, a different photon energy contributes to the image. Thus, Fig. 111.35(b) is a quasi-2-D face-on radiograph of the vanadium. The relative modulation depth of the structures is  $\sim 15\%$  (corresponding to vanadium thickness modulation of  $\pm 0.5 \mu\text{m}$ ), considerably higher than the modulation depth of the expected EXAFS ( $< 5\%$ ), making the reliable measurement of EXAFS impossible. It should be noted that the EXAFS modulations [appearing as vertical lines in records like that in Fig. 111.35(b)] are due to modulations in the absorption as functions of photon energy, whereas the 2-D structure modulations



E15767JR

Figure 111.35

(a) High pressure achieved with high laser irradiance: VISAR-measured back-surface velocity and derived pressure for an irradiance of  $25 \text{ TW/cm}^2$  ( $400\text{-}\mu\text{m}$ -vacuum-gap target, without a heat shield). (b) EXAFS record for a target shot at this irradiance showing nonuniformities believed to be due to the instability of the rarefaction wave following the unloading of the laser-launched shock at the rear surface of the reservoir. (The EXAFS record is effectively a 2-D radiograph of the target, and the intensity modulations are due to modulations in the thickness of the vanadium layer.)

in Fig. 111.35(b) must be due to modulations in the thickness of the vanadium layer. Similar behavior was seen for targets with or without a heat shield. A possible explanation for this observed modulation is related to the instability occurring when the laser-launched shock arrives at the back surface of the reservoir, leading to a rarefaction wave moving in the opposite direction.<sup>20</sup> Modulations in the density of the expanding reservoir material grow linearly with time, at a rate proportional to

the shock speed and the perturbation wave number (see Fig. 5 in Ref. 20). These modulations result in modulations in the strength of impact on the target and, therefore, to modulations in the latter's compression. The instability appears for targets with or without a heat shield. The only common characteristic of the unstable cases is the high laser irradiance. This can be explained by the higher shock speed at higher laser intensities, leading to a higher growth rate. It is noteworthy that these nonuniformities do not seem to affect the VISAR signal [Fig. 111.35(a)]. The remainder of this article shows only results at irradiances lower than  $20 \text{ TW/cm}^2$ , where the nonuniformities discussed here were not observed.

### 3. The Heat Shield

Simulations described below show that without a heat shield, the front surface of the sample heats up substantially ( $>10^4 \text{ K}$  for  $17 \text{ TW/cm}^2$ ) and the heat flow into the sample creates a temperature gradient. The inclusion of a heat shield greatly reduces this heating and creates a quasi-uniform temperature profile of the order of  $10^2 \text{ K}$ . This heating has a dramatic effect on the EXAFS spectra, as seen when comparing EXAFS results for the two cases of targets with and without a heat shield. As explained above, EXAFS is sensitive to the temperature because of the Debye–Waller term in Eq. (1). The back-surface velocity (both measured and simulated) is affected very little by this heating. This is related to the fact that the pressure in the sample is determined mainly by the reservoir plasma at stagnation and the effect of target preheat is mainly to lower the density; in the relevant part of parameter space a very large increase in temperature at a constant pressure causes only a small decrease in density. Therefore, to achieve maximum compression and uniform, low temperature in laser ICE experiments, it is necessary to use targets with a heat shield.

The effect of the heat shield on the target behavior was studied with 1-D runs of the *LASNEX* code. Figure 111.36(a) shows the evolution of pressure on the front surface of the vanadium sample, with and without a heat shield, for otherwise identical conditions. Dashed curves refer to targets with a heat shield; solid curves refer to targets without a heat shield. In Fig. 111.36(b), the curves that rise later correspond to the  $400\text{-}\mu\text{m}$  vacuum gaps. The smaller vacuum gap yields a higher pressure. The introduction of a heat shield creates a weak shock, as evidenced by the sharp initial rise in pressure. Some reverberation is due to shock reflections, but when the pressure increases further, its behavior is almost the same as when the heat shield is absent. The predicted effect of the heat shield on the rear-surface velocity is seen in the experiment (Fig. 111.33 compared with Fig. 111.37 below). Figure 111.36(b) shows the

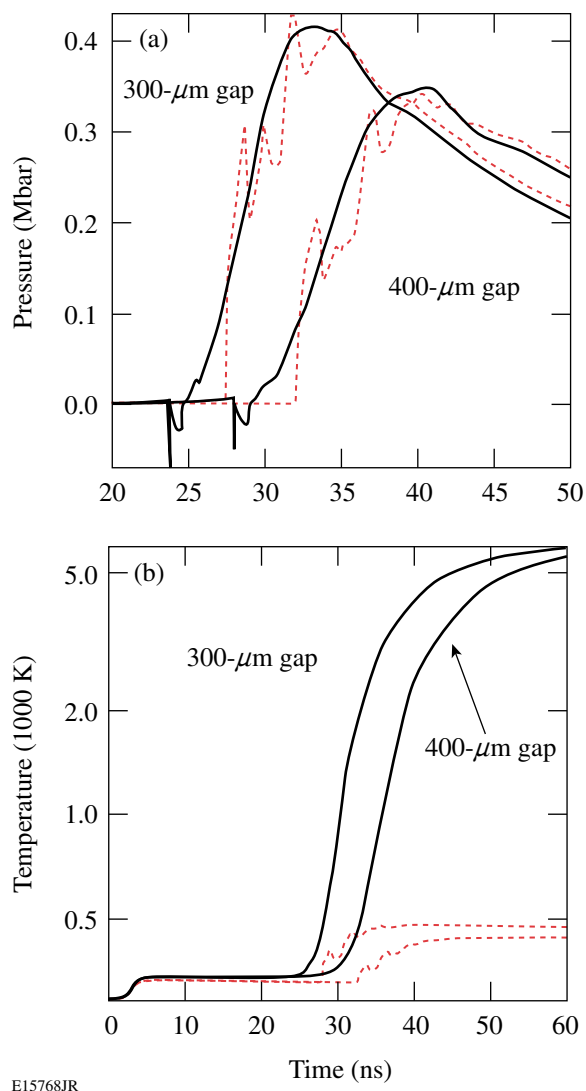


Figure 111.36  
*LASNEX* simulation for targets of two different vacuum gaps, with and without a heat shield: (a) the evolution of pressure on the front surface of the vanadium sample, and (b) the evolution of temperature in the middle of the vanadium sample. Dashed curves: with a heat shield; solid curves: without a heat shield. The heat shield is seen to effectively block the heating from reaching the sample. It has a much greater effect on the temperature than on the pressure. The results in (a) are borne out by the VISAR results and those in (b) by the EXAFS results.

evolution of temperature in the middle of the vanadium sample with and without a heat shield. The heat shield effectively eliminates the heat flow from the front surface. More simulation examples, as will be shown in Figs. 111.42 and 111.43, can be summarized as follows (for  $17 \text{ TW/cm}^2$  at times  $\geq 35 \text{ ns}$ ): (a) With a heat shield the temperature is quasi-uniform and low ( $\sim 10^2 \text{ K}$ ) and the compression is 15%. (b) Without a heat shield the temperature falls sharply from a very high surface value

(>10<sup>4</sup> K) and toward the back surface approaches ~500 K. The compression, ~8%, is much smaller than with a heat shield. These simulation results are borne out by the EXAFS measurements (as will be shown in Fig. 111.43).

Figure 111.37 shows the VISAR-measured rear-surface velocity of an ICE target of 300- $\mu\text{m}$  vacuum gap, with a heat shield, irradiated at 20 TW/cm<sup>2</sup>. In close agreement with Fig. 111.36, the heat shield introduces a sharp initial rise in the velocity due to a shock, but later the velocity approaches a curve characteristic of a shockless compression. Thus, the employment of a heat shield results in a significant improvement in target performance, with only a small perturbation. The thickness of the heat shield (8  $\mu\text{m}$ ) was chosen to be sufficiently large to protect the sample from heating but not large enough to cause steepening of the compression wave into a strong shock. With Be, where both the density and the sound speed are higher than for CH, a thicker heat shield could be used without causing such steepening.

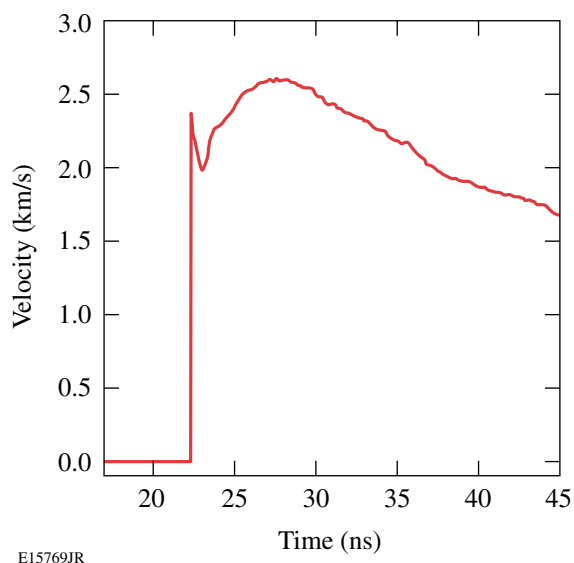


Figure 111.37

VISAR-measured rear-surface velocity of an ICE target of 300- $\mu\text{m}$  vacuum gap, with a heat shield, irradiated at 20 TW/cm<sup>2</sup>. In close agreement with Fig. 111.36, the heat shield introduces a sharp initial rise in the velocity due to a shock, but later the velocity approaches the shape of the velocity curve obtained with no heat shield.

#### 4. Measurements of Preheat

To measure the temperature rise due to backlighter radiation, the EXAFS spectrum is obtained when irradiating the backlighter but without firing the drive beams. The temperature rise deduced from the EXAFS spectrum is then solely due to the backlighter radiation. The temperature is deduced from a

fit of the EXAFS spectrum calculated by the FEFF code to the experimental spectrum. As explained in the **Introduction** (p. 167), the parameters  $R$  (nearest-neighbor distance) and  $\sigma$  (mean atomic vibration amplitude) in the FEFF code are varied to yield the best fit. The resulting values of  $R$  and  $\sigma$  yield the temperature and compression. A typical result is shown in Fig. 111.38. Here the best fit of the FEFF code corresponds to a compression of 1 (i.e., the normal density of vanadium, 6.11 g/cm<sup>3</sup>) and a temperature rise from room temperature of  $\Delta T \sim 200$  K. The precision of temperature determination<sup>8</sup> is 10% to 15%.

To measure the preheat by radiation from the laser-deposition region, the target is probed at ~20 ns after firing the driving beams, i.e., before the impact of the expanding reservoir on the vanadium sample. The FEFF fit shown in Fig. 111.39 yields a temperature of 630 K (and normal density). Of this, a rise of ~200 K is shown in Fig. 111.38 to be due to the backlighter radiation. Thus, the temperature rise due to radiation from the laser-deposition region is ~130 K. The corresponding calculated preheat can be read off Fig. 111.36(b) at times <30 ns (preheat due to the backlighter is not included in the simulations). The result is ~90 K; the discrepancy could be due to shot irreproducibility (since two target experiments are required to make this determination). It should be noted that heating due to radiation from the laser-deposition region in the case of shock compression<sup>8,9</sup> is negligible because in that case

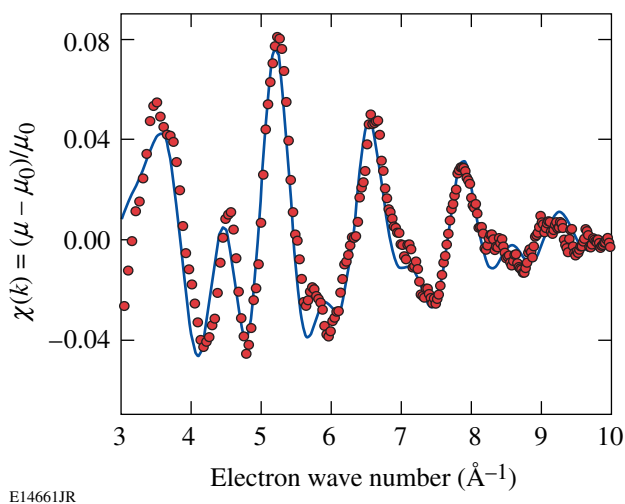
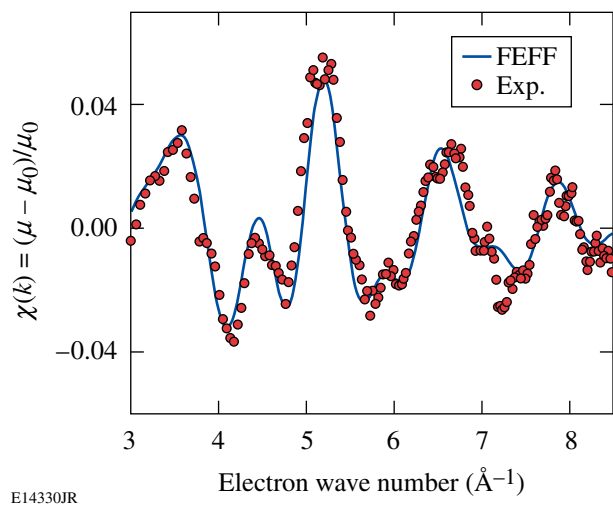


Figure 111.38

Fitting spectra calculated by the FEFF code to the measured EXAFS for the case where the drive beams were not shot. The temperature of the best-fit spectrum corresponds to an increase above room temperature of  $\Delta T \sim 200$  K. This heating is due to radiation from the imploding spherical target. The density of the best-fit spectrum corresponds to the normal density of vanadium.



E14330JR

Figure 111.39

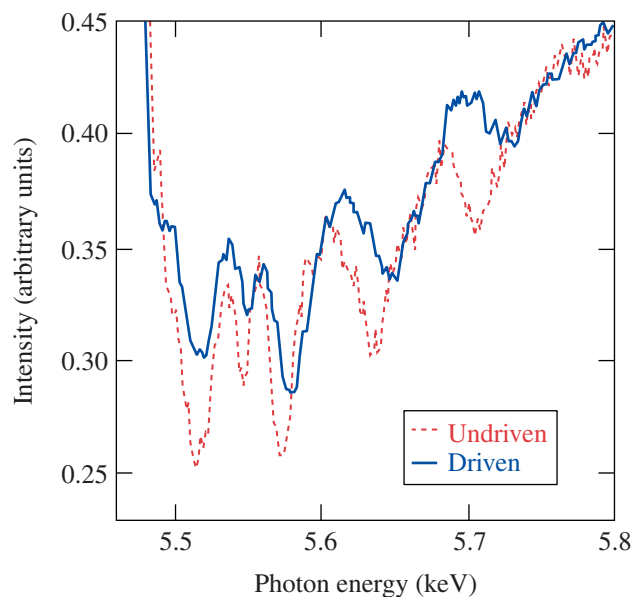
Fitting FEFF spectra to the measured EXAFS of a driven target at 20 ns (i.e., before the impact of the expanding reservoir on the vanadium sample). This serves to determine the preheat due to radiation from the laser-deposition region, 130 K in this case.

the laser intensity required for achieving the same pressure is about ten times smaller than in the case of ICE. Nevertheless, the heating due to compression alone is considerably lower in the case of ICE.

### 5. EXAFS Measurement of Compression and Temperature

EXAFS measurements of the vanadium were made around peak compression. Figure 111.40 shows the raw measured spectra for undriven and driven ICE vanadium targets [(before extracting the  $\chi(k)$  function)]. In the undriven case only the backlighter target was irradiated; the driven case refers to a target with a heat shield, a 300- $\mu\text{m}$  vacuum gap, irradiated at 17  $\text{TW}/\text{cm}^2$ . Comparison of the EXAFS modulations above the vanadium K edge for the two spectra clearly shows the effect of compression: (a) a higher density, as evidenced by the lengthening of the EXAFS modulation period, and (b) heating, as evidenced by the faster damping of the oscillations with increasing photon energy. The driven spectrum of Fig. 111.40 was analyzed with the FEFF EXAFS code. The best fit, shown in Fig. 111.41, yields the conditions within the vanadium at the time 39 ns (with respect to firing the drive-laser beams). The best fit corresponds to a compression of 15% (i.e., a density of 7  $\text{g}/\text{cm}^3$ ) and a temperature of 720 K.

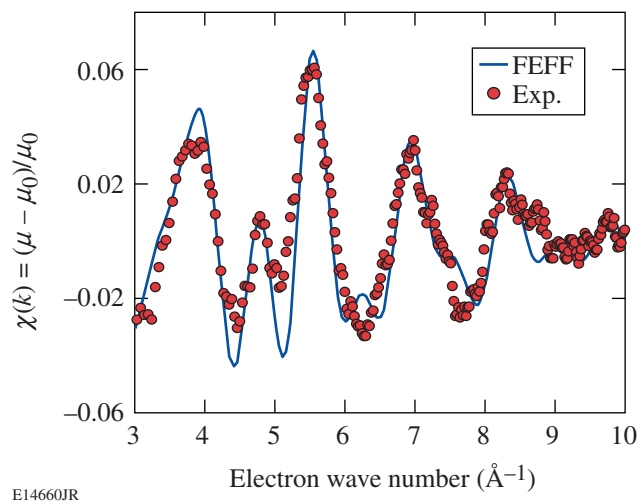
As explained in the **Introduction** (p. 167), the FEFF fit yields the parameters  $R$  and  $\sigma^2$ ;  $R$  (the nearest-neighbor distance) yields the density, whereas the temperature is derived



E15770JR

Figure 111.40

Measured spectra for undriven and driven ICE vanadium targets (before extracting the  $\chi$  function). Comparison of the EXAFS modulations above the vanadium K edge for the two spectra clearly shows the effect of compression, namely, the lengthening of the modulation period, and the effect of heating, namely, the faster damping with increasing photon energy.

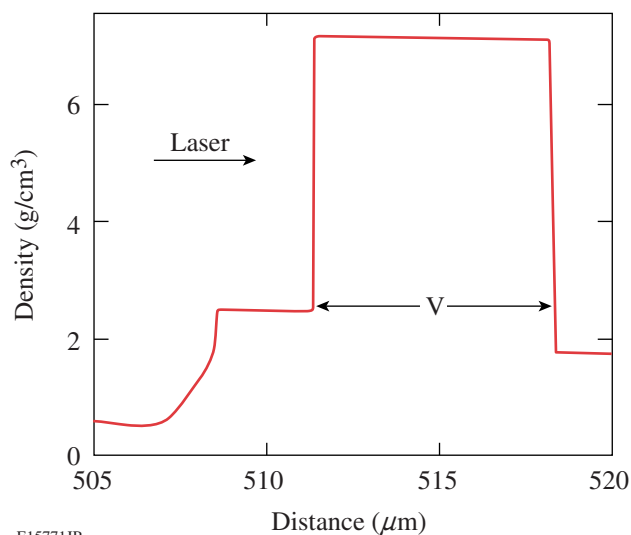


E14660JR

Figure 111.41

EXAFS measurement of ICE compression: fitting FEFF spectrum to the measured EXAFS for the case of an ICE target irradiation at  $\sim 17 \text{ TW}/\text{cm}^2$ . The fitting parameters yield a compression of 15% and a temperature of 720 K. Only  $\sim 90 \text{ K}$  is the increase due to compression; the rest is preheat. This is a demonstration that laser-driven ICE can achieve a similar compression at a lower temperature than in shock compression.

from  $\sigma^2$  and the density. The corresponding *LASNEX* simulation of the vanadium density for a 300- $\mu\text{m}$ -vacuum-gap target, with heat shield, at 39 ns is shown in Fig. 111.42, showing a uniform profile. The time 39 ns [which is slightly past peak compression, see Fig. 111.36(a)] was chosen because then the compression profile becomes uniform. The measured compression value is in excellent agreement with *LASNEX*. As seen above, of the total temperature rise from room temperature,  $\Delta T \sim 200$  K is the increase due to radiation from the backlighter and  $\Delta T \sim 130$  K is the increase due to radiation from the laser-absorption region. Thus, only  $\sim 90$  K is the increase due to compression. This result can be compared with the EXAFS measurement of shock compression of vanadium,<sup>8</sup> where the same compression was accompanied by a temperature rise of  $\Delta T = 770$  K. Thus, *laser-driven ICE can achieve a similar compression at a lower temperature than in shock compression*. At higher drive pressures this advantage of ICE will increase because although preheat by radiation from the laser-absorption region will be higher, the main preheat (due to the backlighter) need not increase.



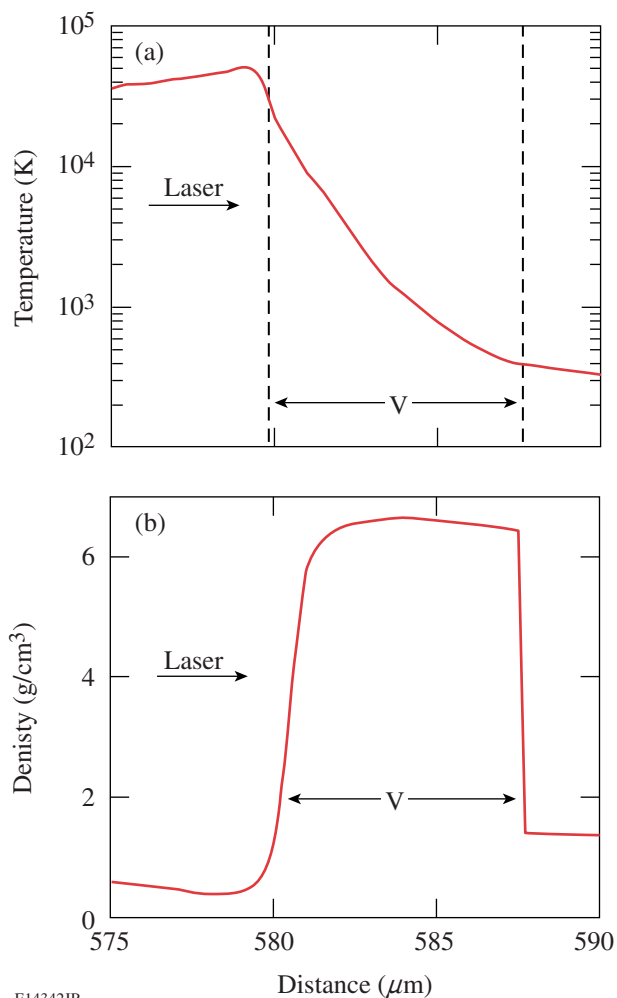
E15771JR

Figure 111.42

*LASNEX* simulation of the vanadium (V) density for a target with a heat shield, 300- $\mu\text{m}$  vacuum gap, at 39 ns. By the time the pressure starts to fall the density becomes uniform. The density ( $\sim 7$  g/cm<sup>3</sup>) corresponds to a compression of 1.15, in very good agreement with the measured value (Fig. 111.41).

We turn now to the case of an ICE target without a heat shield. As discussed above, the severe heating of the vanadium front surface creates a strong temperature gradient that makes the EXAFS analysis more complicated and less reliable. The value of such target shots is mostly in demonstrating that without a heat shield such severe heating indeed takes place. Fig-

ure 111.43 shows the relevant *LASNEX*-simulated temperature and density profiles for a 400- $\mu\text{m}$ -vacuum-gap target without a heat shield, at 37 ns. Heating from the plasma impact is seen to be severe. The density profile shows, as explained above, a lower density than in the case of a target with a heat shield (Fig. 111.42):  $\sim 6.5$  g/cm<sup>3</sup> (compression of 8%) as compared with  $\sim 7$  g/cm<sup>3</sup> (compression of 15%). We use these profiles to calculate the expected EXAFS spectra, shown in Fig. 111.44(a). For various depths within the vanadium, EXAFS spectra are calculated by the FEFF code, using the local density and temperature values given by *LASNEX*. Three examples of such spectra are shown, as well as the spatial average. The



E14342JR

Figure 111.43

*LASNEX*-simulated temperature (a) and density (b) profiles for a 400- $\mu\text{m}$ -vacuum-gap target without a heat shield, at 37 ns. Heating from the plasma impact is seen to be severe, resulting in a lower density (or compression). The profiles are used to calculate the expected EXAFS spectrum [Fig. 111.44(a)] by averaging over the spatially resolved EXAFS spectra.

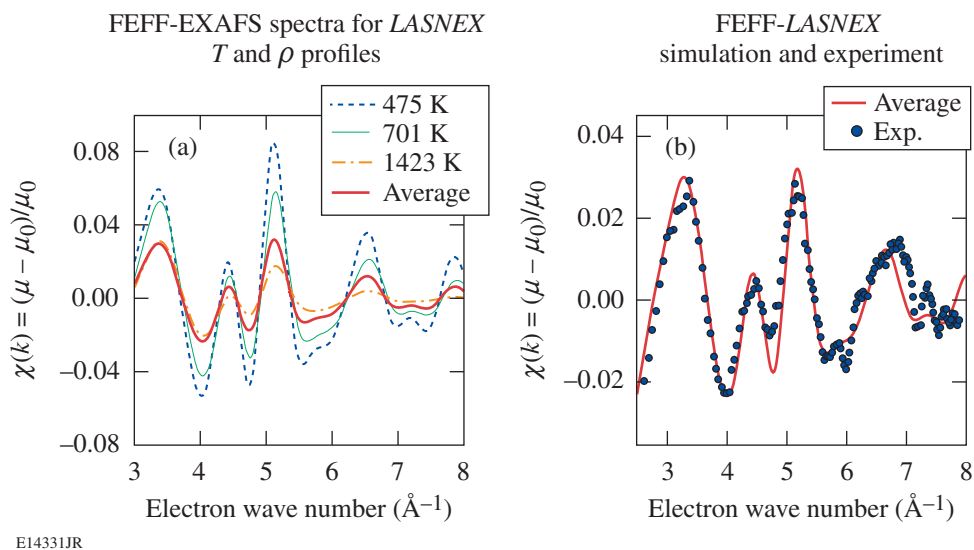
regions of higher temperatures contribute very little to the average. Effectively, the average is over the region where the temperature is less than  $\sim 1000$  K. The main effect of the high temperature is to lower the amplitude of the average spectrum. This is because the secular absorption  $\mu_0(k)$ , appearing in the denominator of  $\chi(k)$ , is independent of temperature and thus corresponds to absorption throughout the vanadium thickness. Since the amplitude of the average spectrum in Fig. 111.44(a) is smaller than that in Fig. 111.41 (the case with a heat shield) by a factor of  $\sim 2.5$ , the front  $\sim 60\%$  of the vanadium thickness has temperatures much higher than  $\sim 1000$  K; this agrees with the computed temperature profile in Fig. 111.43(a). Thus, *the impact heating and its suppression by the heat shield is demonstrated*. Figure 111.44(b) shows a comparison of the average spectrum from (a) and the corresponding experimental spectrum. Unlike in Figs. 111.38, 111.39, and 111.41 where FEFF profiles were adjusted to fit the data, here the FEFF profiles are fixed by the *LASNEX*-calculated parameters.

However, some adjustment had to be made in the frequency of the calculated EXAFS (adding 4% compression) to fit the data, but, even so, the fit is poor. This is due to the difficulty in correctly simulating EXAFS in a steep temperature gradient. Nevertheless, the main goal of such target shots was realized: the low amplitude of the spectrum in Fig. 111.44(b) as com-

pared with that in Fig. 111.41 is clear evidence of significant sample heating when a heat shield is not used.

## Conclusions

In summary, EXAFS measurements in isentropic compression experiments show details not accessible by VISAR measurements. In particular, the sample temperature has been measured. To determine the temperature rise due to the compression, the preheat was determined separately and subtracted out. This preheat is due to three sources: radiation from the laser-deposition region, radiation from the backlighter, and heat conduction from the front surface of the target. In the present experiment the preheat was higher than the heating due to the compression. In future experiments at higher compressions, however, the reverse may be true. The experiments showed that when a heat shield is not present, significant heating occurs within a few microns of the surface. The shock generated by the heat shield has only a small effect on the main compression wave; a heat shield made of a material of high sound speed (such as diamond) may greatly reduce this shock. The experiments also showed that a nonuniform compression occurs at irradiances higher than  $\sim 20$  TW/cm<sup>2</sup> (or pressures higher than  $\sim 0.6$  Mbar); the more-uniform irradiation of a hohlraum excited by the laser beams may reduce this effect.



E14331JR

Figure 111.44

EXAFS analysis for the nonuniform case of an ICE target without a heat shield. (a) For various depths within the vanadium, EXAFS spectra are calculated by the FEFF code, for the density and temperature values given by *LASNEX* (Fig. 111.43). Three examples of such spectra are shown, as well as the spatial average. (b) Comparison of the average spectrum from (a), with slight adjustments, and the corresponding experimental spectrum. The low amplitude of the spectrum in Fig. 111.44(b) as compared with that in Fig. 111.41 is evidence for significant sample heating when a heat shield is not used.

## ACKNOWLEDGMENT

This work was supported by the U.S. Department of Energy Office of Inertial Confinement Fusion under Cooperative Agreement No. DE-FC52-92SF19460, the University of Rochester, and the New York State Energy Research and Development Authority. The support of DOE does not constitute an endorsement by DOE of the views expressed in this article. Portions of this work were performed under the auspices of the U. S. Department of Energy by the University of California, Lawrence Livermore National Laboratory (LLNL) under Contract No. W-7405-Eng-48. Additional support was provided by LDRD project 04-ERD-071 at LLNL.

## REFERENCES

1. B. A. Remington, G. Bazan, J. Belak, E. Bringa, M. Caturla, J. D. Colvin, M. J. Edwards, S. G. Glendinning, D. S. Ivanov, B. Kad, D. H. Kalantar, M. Kumar, B. F. Lasinski, K. T. Lorenz, J. M. McNaney, D. D. Meyerhofer, M. A. Meyers, S. M. Pollaine, D. Rowley, M. Schneider, J. S. Stölken, J. S. Wark, S. V. Weber, W. G. Wolfer, B. Yaakobi, and L. V. Zhigilei, *Metall. Mater. Trans. A* **35A**, 2587 (2004).
2. T. R. Boehly, R. S. Craxton, T. H. Hinterman, J. H. Kelly, T. J. Kessler, S. A. Kumpan, S. A. Letzring, R. L. McCrory, S. F. B. Morse, W. Seka, S. Skupsky, J. M. Soures, and C. P. Verdon, *Rev. Sci. Instrum.* **66**, 508 (1995).
3. P. A. Lee *et al.*, *Rev. Mod. Phys.* **53**, 769 (1981).
4. C. Dai *et al.*, *J. Phys. D: Appl. Phys.* **34**, 3064 (2001).
5. J. Edwards *et al.*, *Phys. Rev. Lett.* **92**, 075002 (2004).
6. K. T. Lorenz *et al.*, *Phys. Plasmas* **12**, 056309 (2005).
7. K. T. Lorenz *et al.*, *High Energy Density Phys.* **2**, 113 (2006).
8. R. F. Smith *et al.*, *Astrophys. Space Sci.* **307**, 269 (2007).
9. B. Yaakobi, D. D. Meyerhofer, T. R. Boehly, J. J. Rehr, B. A. Remington, P. G. Allen, S. M. Pollaine, and R. C. Albers, *Phys. Plasmas* **11**, 2688 (2004).
10. B. Yaakobi, T. R. Boehly, D. D. Meyerhofer, T. J. B. Collins, B. A. Remington, P. G. Allen, S. M. Pollaine, H. E. Lorenzana, and J. H. Eggert, *Phys. Plasmas* **12**, 092703 (2005).
11. J. J. Rehr, R. C. Albers, and S. I. Zabinsky, *Phys. Rev. Lett.* **69**, 3397 (1992).
12. E. Sevillano, H. Meuth, and J. J. Rehr, *Phys. Rev. B* **20**, 4908 (1979).
13. R. M. More *et al.*, *Phys. Fluids* **31**, 3059 (1988).
14. G. R. Gathers, *J. Appl. Phys.* **59**, 3291 (1986).
15. G. J. Stretz and L. H. MacFarland, in *Shock Compression of Condensed Matter—1999*, edited by M. D. Furnish, L. C. Chhabildas, and R. S. Hixson, AIP Conf. Proc. 505 (American Institute of Physics, New York, 2000), pp. 201–204.
16. P. M. Celliers *et al.*, *Appl. Phys. Lett.* **73**, 1320 (1998).
17. D. B. Hayes, Sandia National Laboratory, Albuquerque, NM, SAND2001-1440, NTIS Order No. DE2001-783087 (2001); D. B. Hayes *et al.*, *J. Appl. Phys.* **96**, 5520 (2004).
18. G. B. Zimmerman and W. L. Kruer, *Comments Plasma Phys. Control. Fusion* **2**, 51 (1975).
19. T. J. Kessler, Y. Lin, J. J. Armstrong, and B. Velazquez, in *Laser Coherence Control: Technology and Applications*, edited by H. T. Powell and T. J. Kessler (SPIE, Bellingham, WA, 1993), Vol. 1870, pp. 95–104.
20. J. G. Wouchuk and R. Carretero, *Phys. Plasmas* **10**, 4237 (2003).

---

# The Effect of Resonance Absorption in OMEGA Direct-Drive Designs and Experiments

## Introduction

Ignition of thermonuclear fuel (DT mixture) requires a fuel areal density  $\geq 0.3 \text{ g/cm}^2$  and a hot-spot temperature  $\geq 10 \text{ keV}$  (Refs. 1 and 2). Such conditions are predicted to be achieved in direct-drive inertial confinement fusion (ICF) designs, in which a cryogenic spherical DT-ice-shell target is imploded using direct illumination by intense laser beams.<sup>3–7</sup> High energy gain in direct-drive ICF designs is achieved by optimizing the laser pulse shape and target dimensions.<sup>1,8,9</sup>

Physical understanding of laser–plasma coupling is required for accurate numerical modeling of high-gain, direct-drive ICF designs. These designs are based on precise timing of laser-driven shocks, which determine the target adiabat (defined as a ratio of the fuel pressure to the Fermi-degenerate pressure).<sup>10,11</sup> The shock strength depends crucially on mechanisms of laser light absorption. A theoretical and experimental investigation of laser absorption, focusing on the effect of resonance absorption for typical conditions in the direct-drive experiments on the OMEGA Laser System,<sup>12</sup> is the subject of this article.

Resonance absorption of electromagnetic waves in an unmagnetized, inhomogeneous plasma has been of considerable interest for a long time.<sup>13–25</sup> In this process, a  $p$ -polarized electromagnetic wave, i.e., a wave that has a nonzero electric field component along the electron-density gradient  $\nabla n_0$ , propagates from low to high densities and approaches the critical surface with an electron density  $n_0 = n_{cr}$ , where the laser frequency  $\omega$  matches the local electron plasma frequency  $\omega_{pe} = 4\pi n_0 e^2 / m_e$ . Here,  $e$  and  $m_e$  are the electron charge and mass, respectively. During this propagation, the wave is partially reflected from the turning point, defined by the condition  $\omega_{pe} = \omega \cdot \cos\theta$ , where  $\theta$  is the angle between the vacuum wave vector  $\mathbf{k}$  and the density gradient, and the small part of the wave energy tunnels to the critical density and excites the resonance plasma oscillations. These oscillations can be damped by various mechanisms, including electron–ion collisional damping and excitation of Langmuir waves. A one-dimensional model of resonance absorption in linear density profiles has been the subject of numerous analytical and numerical investigations.

Forslund *et al.*<sup>19</sup> solved numerically the wave equation for the electric field  $\mathbf{E}$  and found the absorption fraction of electromagnetic waves as a function of  $q \equiv (kL)^{2/3} / \sin^2\theta$ , where  $L$  is the density scale length. This result was confirmed later by the simulations of Pert<sup>21</sup> and Means *et al.*,<sup>22</sup> who employed different methods. All of these numerical results agree well with analytic results obtained by Omel’chenko and Stepanov,<sup>16</sup> Speziale and Catto,<sup>20</sup> and Tang<sup>17</sup> for limited ranges of  $q$ . An analytic expression for the absorption fraction in the whole range of  $q$  was obtained by Hinkel–Lipsker *et al.*<sup>23</sup> in the limit of small thermal and collisional effects. Later, the same authors<sup>24</sup> found analytic solutions of the problem in the case of parabolic density profiles. In our current numerical study, we do not restrict ourselves by linear or parabolic density profiles using density profiles obtained in hydrodynamic simulations. A recent study by Xu *et al.*<sup>25</sup> concentrated on modifications in resonance absorption caused by the relativistic effect and pondermotive force.

Direct-drive experiments conducted on OMEGA are routinely simulated using the 1-D hydrodynamic code *LILAC*.<sup>26</sup> The standard laser-absorption algorithm in *LILAC* is the ray-trace algorithm with ion–electron collisional absorption (inverse bremsstrahlung). An optional semi-analytic model of resonance absorption<sup>27</sup> can be used in conjunction with the ray-trace algorithm. An advantage of this semi-analytic model is its simplicity, whereas a disadvantage is its insufficient accuracy: it typically overestimates the resonance absorption by a factor of  $\sim 2$  (Ref. 27). In this study, to more accurately investigate resonance absorption, the ray-trace algorithm of laser absorption in *LILAC* is replaced by a new algorithm based on the numerical solution of a wave equation in planar geometry.

This article addresses the following issues: (1) The wave equation describing the steady-state structure of electromagnetic and Langmuir wave components in inhomogeneous plasma is presented, and the numerical method in the planar geometry is described. (2) The results of numerical simulations of the resonance absorption in OMEGA plasmas are presented in the case of both planar and spherical geometries. (3) The

results of planar reflection light experiments on OMEGA are presented and compared with simulations, and a design of planar shock-timing experiments is considered. (4) The main results are discussed and summarized in the final section.

### Resonance Absorption in the Fluid Approximation

We consider an electromagnetic wave of frequency  $\omega$  propagated in vacuum, which obliquely irradiates a slab of warm, unmagnetized plasma. Properties of the slab are assumed to vary with a characteristic scale length  $\gg c/\omega$ . Neglecting ion and low-frequency electron motions, one can describe a high-frequency electron motion caused by the electromagnetic wave using the linearized momentum equation

$$\frac{\partial \mathbf{u}_e}{\partial t} = -\frac{1}{m_e n_0} \nabla P_e - \frac{e}{m_e} \mathbf{E} - \nu \mathbf{u}_e, \quad (1)$$

where  $\mathbf{u}_e$  is the velocity and  $P_e$  is the pressure of electrons,  $\mathbf{E}$  is the electric field, and  $\nu$  is the damping rate. Assuming a polytropic equation of state (e.g., Ref. 28),  $P_e \propto n^3$ , where  $n$  is the electron density, and a time variation of all perturbed quantities  $\propto e^{-i\omega t}$ , and combining Eq. (1) with the Poisson equation  $\nabla \cdot \mathbf{E} = -4\pi en$ , we derive the expression for the current density

$$\mathbf{j} = -en_0 \mathbf{u}_e = i \frac{\omega_{pe}^2 \mathbf{E}}{4\pi(\omega + i\nu_{em})} - i \frac{3v_e^2 \nabla(\nabla \cdot \mathbf{E})}{4\pi(\omega + i\nu_w)}, \quad (2)$$

where  $v_e^2 = T_e/m_e$  is the electron thermal velocity square and  $T_e$  is the electron temperature. In Eq. (2), two different damping rates  $\nu_{em}$  and  $\nu_w$  have been introduced instead of the single damping rate  $\nu$  in Eq. (1) (see Ref. 19). The rate  $\nu_{em}$  corresponds to the electromagnetic and  $\nu_w$  to the Langmuir wave components represented by the first and second terms on the right-hand side of Eq. (2), respectively. The electric field  $\mathbf{E}$  obeys Maxwell's equations, which can be reduced to the steady-state wave equation

$$\nabla^2 \mathbf{E} - \nabla(\nabla \cdot \mathbf{E}) + \frac{\omega^2}{c^2} \left( \mathbf{E} + i \frac{4\pi}{\omega} \mathbf{j} \right) = 0, \quad (3)$$

where  $\mathbf{j}$  is defined by Eq. (2). Solving Eq. (3) with respect to  $\mathbf{E}$ , one can calculate the laser-absorption rate  $Q = \mathbf{j} \cdot \mathbf{E}$ . With the help of Eq. (2),  $Q$  can be expressed in the following form:

$$Q = Q_{em} + Q_w$$

$$= \nu_{em} \frac{\omega_{pe}^2}{\omega^2 + \nu_{em}^2} \frac{\mathbf{E}^2}{8\pi} + \nu_w \frac{3v_e^2}{\omega^2 + \nu_w^2} \frac{(\nabla \cdot \mathbf{E})^2}{8\pi}. \quad (4)$$

This form allows one to distinguish the different contributions to laser absorption: the electromagnetic  $Q_{em}$  and Langmuir wave  $Q_w$  components. The damping rate  $\nu_{em}$  is determined by the collisional damping,  $\nu_{em} = \nu_{ei}$  (Ref. 2). The damping rate  $\nu_w$ , in addition to collisional damping, must include damping due to kinetic effects, which describe dissipation of Langmuir waves at  $k\lambda_D \gtrsim 1$ , where  $k$  is the wave number and  $\lambda_D$  is the Debye length. This gives  $\nu_w = \nu_{ei} + \nu_L$ , where

$$\nu_L = \left( \frac{27\pi}{8} \right)^{1/2} \frac{\omega_{pe}^2 \omega^2}{(\omega^2 - \omega_{pe}^2)^{3/2}} e^{-\frac{3}{2} \frac{\omega^2}{\omega^2 - \omega_{pe}^2}} \quad (5)$$

is the Landau damping rate.<sup>29</sup>

We consider planar geometry and introduce the cartesian coordinates  $(x, y, z)$  with the  $z$  axis perpendicular to the plane of the plasma slab. The slab is uniform in the  $x$  and  $y$  directions and nonuniform in the  $z$  direction. The vacuum wave vector  $\mathbf{k}$  of the incident plane electromagnetic wave is located in the  $y$ - $z$  plane and inclined at an angle  $\theta$  with the  $z$  axis. In these coordinates, the  $s$ -polarized electromagnetic wave is described by a solution  $E_x$  of the  $x$  component of Eq. (3). This solution is completely independent of a solution for the  $p$ -polarized wave described by  $E_y$  and  $E_z$ , which obey the coupled  $y$  and  $z$  components of Eq. (3). Assuming an independence of the field of the  $x$  coordinate and periodic dependence on the  $y$  coordinate,  $\propto e^{ik_y y}$ , where  $k_y = (\omega/c) \sin\theta$ , the corresponding components of Eq. (3) can be reduced to second-order ordinary differential equations in the following form: for the  $s$ -polarized wave,

$$\frac{d^2 E_x}{dz^2} + \frac{\omega^2}{c^2} (\epsilon - \sin^2 \theta) E_x = 0, \quad (6)$$

and for the  $p$ -polarized wave,

$$\frac{d^2 E_y}{dz^2} - ik_y (1 - \eta) \frac{dE_z}{dz} + \frac{\omega^2}{c^2} (\epsilon - \eta \sin^2 \theta) E_y = 0, \quad (7)$$

$$\eta \frac{d^2 E_z}{dz^2} - ik_y(1 - \eta) \frac{dE_y}{dz} + \frac{\omega^2}{c^2} (\epsilon - \sin^2 \theta) E_z = 0, \quad (8)$$

where we use the notations

$$\epsilon = 1 - \frac{\omega_{pe}^2}{\omega(\omega + i\nu_{em})} \quad \text{and} \quad \eta = \frac{3v_e^2}{\omega(\omega + i\nu_w)} \frac{\omega^2}{c^2}.$$

These differential equations are solved using the standard finite-difference numerical technique, which requires the solution of linear matrix equations. The matrix equations have a band diagonal form and can be efficiently solved by the LU decomposition method.<sup>30</sup> We assume vacuum boundary conditions for the incident and reflected electromagnetic waves at the outer edge of the plasma corona. For example, these conditions for the *s*-polarized wave are derived by using a vacuum solution in the form  $E_x = Ae^{ik_z z} + Be^{-ik_z z}$ , where  $k_z = (\omega/c) \cos \theta$ , and the complex coefficients *A* and *B* to be determined matching this solution and its first derivative with the corresponding numerical solution at the outer edge. Similarly, other solutions of the electric field,  $E_y$  and  $E_z$ , are considered in the case of the *p*-polarized wave. Knowing the field components, one can calculate the laser-absorption rate using Eq. (4) as the energy source in a 1-D hydrodynamic code.

### Resonance Absorption in Typical OMEGA Plasmas

The 60-beam, 30-kJ OMEGA Laser System<sup>12</sup> is used to study the physics of implosions by conducting spherical and planar experiments with millimeter-scale targets. OMEGA operates at a laser wavelength of  $\lambda = 351$  nm and peak intensities varying from  $10^{14}$  to  $10^{15}$  W/cm<sup>2</sup> with a typical pulse rise time  $\sim 100$  ps and a pulse duration  $\sim 1$  to 3 ns. The pulse can be shaped to optimize target performance.<sup>10,11</sup>

In this section we investigate numerically the effects of resonance absorption for plasma conditions relevant to direct-drive OMEGA experiments. Currently, plastic (CH) material is used as an ablator in most applications;<sup>7</sup> therefore, we concentrate our analysis on CH plasma. All numerical results reported hereafter are obtained by employing the flux-limited Spitzer–Härm thermal-conduction model.<sup>26,31</sup> If not explicitly mentioned, simulations assume a flux-limiter value  $f_{lim} = 0.06$ , and all of our numerical results include the Langdon effect.<sup>32</sup> Note that other more-sophisticated thermal-conduction models can be used, including the models based on the solution of the Fokker–Planck equation<sup>33</sup> and different nonlocal electron transport treatments<sup>34,35</sup> We found, however, that the effect

of resonance absorption is not very sensitive to the particular choice of the thermal-conduction model.

The method of laser-absorption simulation described in the previous section was developed in planar geometry, where the incident light can be properly separated on the *s*- and *p*-polarized components. In spherical geometry, such a separation is not possible and the exact solution of the problem is more complicated. Instead of exactly solving the problem in spherical geometry, an approximate approach can be used to estimate laser absorption with the resonance effect. In the following two subsections we consider first the case of planar geometry, in which the effect of resonance absorption is calculated using the exact method; we then consider the case of spherical geometry, applying the planar-geometry approximation.

#### 1. Planar Geometry

Figure 11.45 shows an example of a simulated electric field in a plasma developed during irradiation of a thick CH foil by a single *p*-polarized OMEGA laser beam with an angle of incidence  $\theta = 23.2^\circ$ . This angle is typically used in planar OMEGA experiments and close to the angle at which resonance absorption is most effective (see the definition of this angle below). The drive laser pulse [Fig. 11.45(a)] is taken from the actual experiment and has a square shape with about 1-ns duration, an average intensity  $I \approx 5 \times 10^{14}$  W/cm<sup>2</sup>, and an initial rise time  $\approx 100$  ps. The intensity modulation seen in Fig. 11.45(a) is due to the effect of smoothing by spectral dispersion.<sup>36</sup> The solutions shown in Fig. 11.45(b) correspond to the time when the pulse intensity reaches the average value at  $t = t_0$ . The distribution of electron density  $n_0$  [shown by the thick line in Fig. 11.45(b)] is obtained using a *LILAC* simulation. The incident laser light propagates from right to left. The electron temperature  $T_e \approx 1$  keV at the critical surface, which is defined by the condition

$$n_0 = n_{cr} \equiv \frac{m_e \omega^2}{4\pi e^2} \approx 9 \times 10^{21} \left( \frac{351 \text{ nm}}{\lambda} \right)^2 \text{ cm}^{-3}. \quad (9)$$

The value of  $T_e$  varies insignificantly on the spatial interval displayed in Fig. 11.45(b). The solution shown by the thin solid line is obtained including all terms in Eq. (1). This solution shows some increase in the electric field near the critical surface and, at the same time, shows a resonant excitation of Langmuir waves. These waves can be clearly seen in Fig. 11.45(b) as the short-wavelength structures at  $z \approx 64 \mu\text{m}$ , whereas the long-wavelength structures at  $z > 64 \mu\text{m}$  correspond to electromagnetic waves. The Langmuir

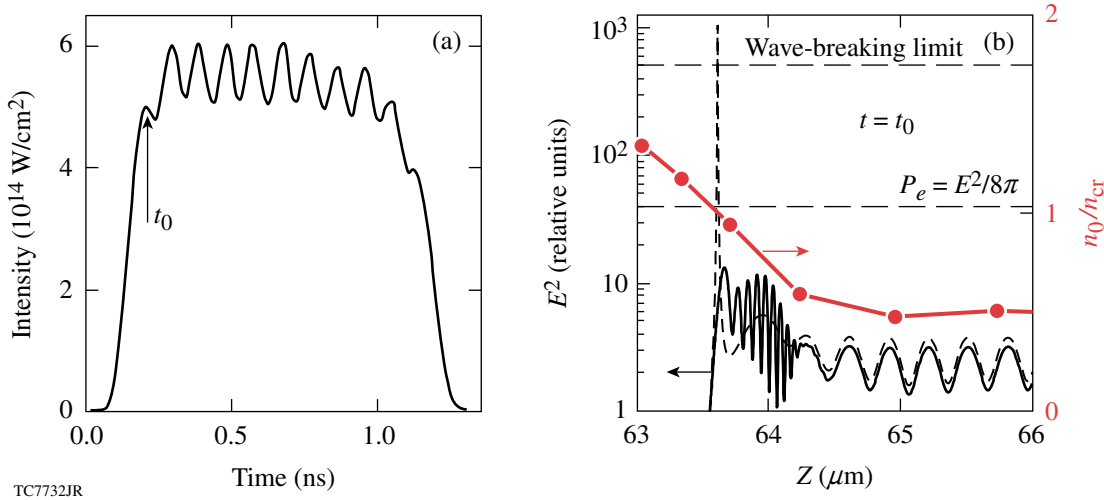


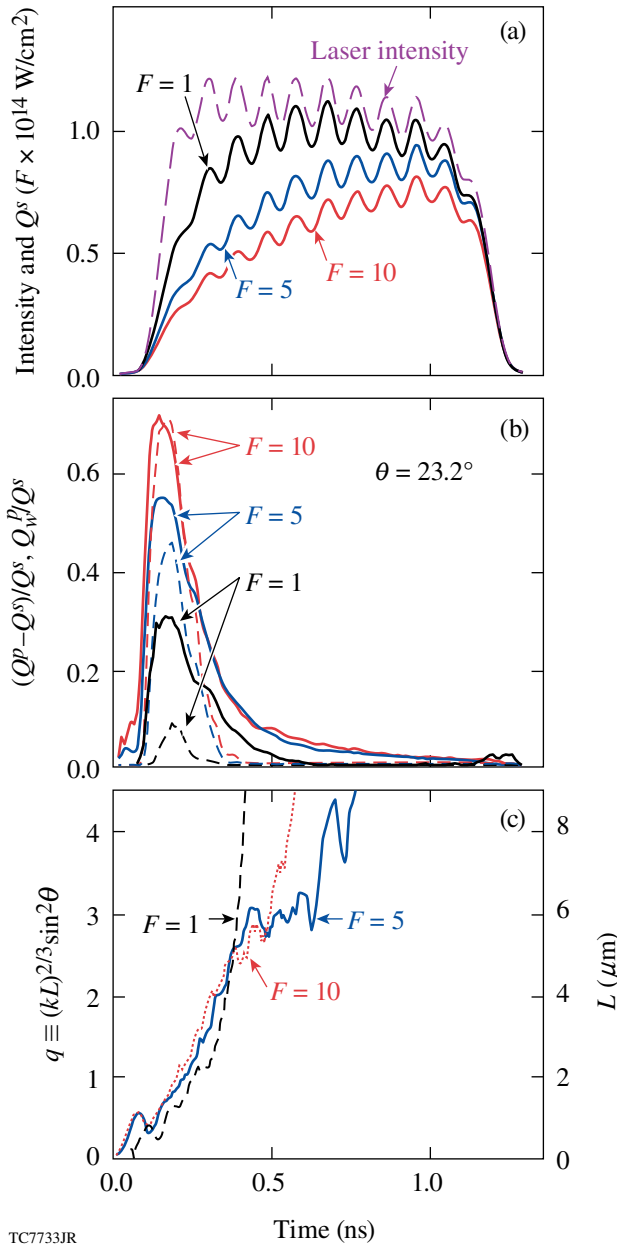
Figure 111.45

Example distribution of the electric field in a CH plasma near the critical surface,  $n_0 = n_{cr}$ . (a) The drive laser pulse irradiated a thick planar CH target at  $\theta = 23.2^\circ$ ; the vertical arrow shows time  $t_0$  and laser intensity for solutions presented in plot (b). (b) Distributions of the electron density  $n_0$  and squared amplitude of the electric field  $E^2 = E_y^2 + E_z^2$ . Laser light with  $p$ -polarization propagates from right to left. The distribution of  $n_0$  (thick solid line) is obtained using a 1-D LILAC simulation. The electron temperature near the critical surface is  $\approx 1$  keV. The thin solid and short-dashed lines show the distribution of  $E^2$  obtained with and without the pressure term in Eq. (1), respectively. The two horizontal dashed lines represent the estimates of the wave-breaking and thermal pressure limits for  $E^2$ .

waves propagate from the critical surface to the right, toward the lower electron density, and decay due to Landau damping at  $n_0 \lesssim 0.6 n_{cr}$  (the “wave-decay” region). Landau damping results in a conversion of the energy stored in Langmuir waves into hot electrons with  $T_h \approx 5$  keV, where the latter temperature is estimated using the phase velocity of Langmuir waves in the wave-decay region. Heating of the plasma [see Eq. (4)] occurs due to both collisional and Landau damping and is localized mainly between the critical surface and the wave-decay region. A typical electron temperature in the hot corona is about 1 to 2 keV, which is 2 to 5 times lower than our estimate of  $T_h$ . This could result in a deviation of the electron distribution function from Maxwellian and nonlocal effects in the energy deposition. In our simulations, however, we neglect such nonlocal effects and assume only the local energy deposition into thermal electrons. For comparison, the solution without excitation of Langmuir waves is shown by the short-dashed line in Fig. 111.45(b). This solution, obtained using Eq. (1) without the pressure term (the cold plasma limit), has a distinctive resonance peak in the electric field at the critical surface. Note that the resonant field in the latter case exceeds the limits for the field corresponding to the electron pressure  $P_e$  and wave-breaking threshold<sup>37</sup> [represented by the lower and upper horizontal dashed lines in Fig. 111.45(b), respectively].

Two important conclusions regarding plasma conditions in direct-drive OMEGA experiments result from the considered example: First, the resonant electric field in a typical OMEGA plasma is significantly below the wave-breaking limit. Second, the electromagnetic pressure corresponding to this field is typically below the electron pressure, which means that the ponderomotive force is weak and can be neglected. These conclusions justify the omission of the nonlinear convection term  $(\mathbf{u}_e \nabla) \mathbf{u}_e$  in Eq. (1).

Next, we study the time evolution of the resonance absorption and its dependence on laser intensity and incident angle. The resonance absorption in a simulation can be quantified by comparing the absorption rates for  $s$ - and  $p$ -polarized laser beams ( $Q^s$  and  $Q^p$ , respectively) since  $Q^p$  includes the effect of resonance absorption and  $Q^s$  does not. Figure 111.46 compares these absorption rates and also presents  $Q_w^p$ , which is the contribution to the absorption rate due to the resonant excitation of Langmuir waves [see Eq. (4)], calculated for the case of thick ( $>200$   $\mu$ m) CH foils irradiated by a 1-ns square pulse at  $\theta = 23.2^\circ$ . Three different average beam intensities have been considered:  $10^{14}$ ,  $5 \times 10^{14}$ , and  $10^{15}$  W/cm $^2$ . Figure 111.46(a) shows the laser pulse shape and absorption rates  $Q^s$  for these three cases. Figure 111.46(b) shows the relative difference  $(Q^p - Q^s)/Q^s$  (solid lines), which characterizes the contribu-



TC7733JR

Figure 111.46

Simulated evolution of the laser-absorption rate for single,  $s$ - and  $p$ -polarized, 1-ns OMEGA laser beams irradiating a thick planar CH target at  $\theta = 23.2^\circ$ . Three different average laser intensities are considered:  $10^{14}$ ,  $5 \times 10^{14}$ , and  $10^{15}$  W/cm $^2$ , which are indicated by the corresponding values of the scaling factor  $F = 1, 5$ , and  $10$ , respectively. (a) Drive-laser pulse (long-dashed line) and absorption rates  $Q^s$  (solid lines) for the  $s$ -polarized beams. These rates do not include the effect of resonance absorption. (b) The relative differences between the absorption rates for  $p$ - and  $s$ -polarized beams  $(Q^p - Q^s)/Q^s$  (solid lines), which demonstrate the effect of resonance absorption in the  $p$ -polarized beams, and the relative absorption rates  $Q_w^p/Q^s$  due to the resonant excitation of Langmuir waves (dashed lines). (c) Evolution of  $q \equiv (kL)^{2/3} \sin^2\theta$  and the density scale length  $L$  at the critical surface. The resonance absorption is important as soon as  $0.1 < q < 2$  (Ref. 19).

tion of resonance absorption to the total laser absorption, and the ratio  $Q_w^p/Q^s$  (dashed lines). The results show that the effect of resonance absorption is important only in the initial 200- to 300-ps period of the laser pulse. This time dependence can be explained by the inverse dependence of resonance absorption on the density scale length  $L$  near the critical surface. Figure 111.46(c) shows the evolution of  $L$  and the dimensionless quantity  $q \equiv (kL)^{2/3} \sin^2\theta$ , where  $k$  is the vacuum wave number of laser light. The resonance absorption can be efficient if  $0.1 \leq q \leq 2$  (Ref. 19). The density scale length is relatively short,  $L \approx 1$  to  $2 \mu\text{m}$  (so  $q < 2$ ), during the rise of laser power. At a later time, at maximum laser power, the length becomes long enough,  $L > 5 \mu\text{m}$  ( $q > 2$ ), to quench the resonance absorption. Another effect seen in Fig. 111.46(b) is that the resonance absorption, including absorption via Langmuir waves, is more significant for higher laser intensities. In particular, the resonance mechanism dominates over inverse bremsstrahlung at the beginning of the laser pulse for pulses with peak intensity  $\geq 5 \times 10^{14}$  W/cm $^2$ . The dependence of resonance absorption on the intensity can be attributed to increased temperature near the critical surface in the case of higher laser intensities.<sup>19</sup>

The angular dependence of resonance absorption is demonstrated in Fig. 111.47, where the results of simulations are shown for a 100-ps laser pulse. For such a short pulse, the contribution of resonance absorption to the total absorption is more prominent and can be more easily measured experimentally (see Fig. 111.46). A laser pulse with a peak intensity of  $5 \times 10^{14}$  W/cm $^2$  is shown by the long-dashed line in Fig. 111.47(a). In the same figure, example absorption rates in the case of  $p$ - and  $s$ -polarized laser beams (thick and thin lines, respectively) and resonant excitation of Langmuir waves in the  $p$ -polarized beam (short-dashed line) are shown for  $\theta = 17^\circ$ . Figure 111.47(b) plots the angular dependence of absorption fractions in the case of  $p$ - and  $s$ -polarized beams and resonant excitation of Langmuir waves, using the same notations as in Fig. 111.47(a). Here, the absorption fraction is defined as the ratio of the corresponding time-integrated absorption rate per unit surface to the time-integrated laser intensity on target. The difference between the absorption fractions for  $p$ - and  $s$ -polarized beams illustrates the relative effect of resonance absorption. This effect peaks at  $\theta \approx 17^\circ$  and corresponds to about a 30% increase in total absorption in comparison with the case of  $s$ -polarized beams. The energy absorbed due to the resonant excitation of Langmuir waves also peaks at  $\theta \approx 17^\circ$ , where the contribution of this energy to the total absorption energy is about 50%.

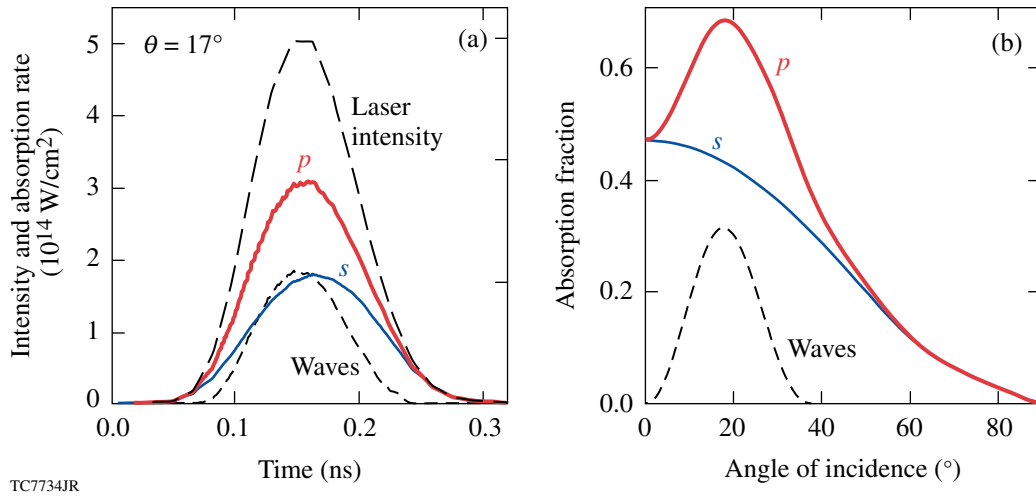


Figure 111.47

Simulated absorption rate and angular dependence of absorption fraction for single,  $s$ - or  $p$ -polarized, 100-ps OMEGA laser beams irradiating a thick planar CH target. (a) Drive-laser pulse with a peak intensity of  $5 \times 10^{14} \text{ W/cm}^2$  (long-dashed line); the absorption rate for the  $p$ - and  $s$ -polarized beams (thick and thin solid lines, respectively), and the absorption rate due to the resonant excitation of Langmuir waves (short-dashed line). All of these rates are calculated assuming  $\theta = 17^\circ$ . (b) Time-integrated absorption fractions as functions of  $\theta$  in the same cases considered in (a). The effect of resonance absorption is represented by the difference in absorption rates and absorption fractions for the  $p$ - and  $s$ -polarized beams. This effect produces the maximum absorption fraction at  $\theta \approx 17^\circ$ .

## 2. Spherical Geometry

In this section, we use an approximate approach to estimate the laser absorption, including the resonance effect, in spherical implosions. We apply the planar method to a small surface element of a spherical target. Such an element is irradiated by the laser light distributed over a range of incident angles  $\theta$  from  $0^\circ$  to  $90^\circ$ . The total absorption rate for a target can be estimated by integrating the absorption rates for a given surface element over  $\theta$  from all angles in the hemisphere that cover the surface element and integrating the result over the entire target surface. This approach can be justified if the thickness of the absorption region is much smaller than the target radius. Such a condition typically occurs during the first few hundred picoseconds in direct-drive OMEGA implosions.

The intensity profile  $I(r)$  across an individual OMEGA laser beam can be approximated by the super-Gaussian<sup>38</sup>  $I(r) = I_0 e^{-(r/r_0)^n}$ , where  $I_0$  is the center beam intensity,  $r$  is the distance from the beam's central axis,  $r_0$  is the beam radius, and  $n$  is the super-Gaussian index. Assuming spherically symmetric illumination of a target of radius  $R$ , it is straightforward to obtain the angular-dependent laser intensity at each point of the target surface,  $I(\theta) = I_0 e^{-(\sin\theta \cdot R/r_0)^n}$ . Then, the intensity on target is

$$\bar{I} = 2\pi \int_0^{\pi/2} I(\theta) \cos\theta \sin\theta d\theta. \quad (10)$$

The angular distribution  $I(\theta)$  is used in the modified planar method in *LILAC* to numerically estimate the laser-absorption rate  $Q$  in spherical implosions. To account for a mixed polarization of laser light from many randomly polarized OMEGA laser beams (up to 13 beams can irradiate a given small surface element), the method assumes an equal mixture of  $s$ - and  $p$ -polarized lights. The corresponding absorption rate is denoted as  $Q^{s,p}$ . The absorption rate calculated using only the  $s$ -polarized light,  $Q^s$ , does not include the effect of resonance absorption and is used for comparison. Note that, with respect to the assumed laser-absorption mechanisms,  $Q^s$  is similar to the absorption rate calculated using the spherical ray-trace method.<sup>26</sup>

Figure 111.48 shows an example of simulated laser-absorption rates in the spherical implosion of a CH target driven by a 12.4-kJ, 1-ns square OMEGA laser pulse. In this example, the target radius  $R = 430 \mu\text{m}$ , and the beam parameters  $r_0 = 352 \mu\text{m}$  and  $n = 4.12$ . The drive-laser pulse (long-dashed line) and calculated evolution of the absorption rates  $Q^s$  (solid lines) and  $Q^{s,p}$  (short-dashed lines) for two values of the flux limiter  $f_{\text{lim}} = 0.06$  and  $0.1$  are shown in Fig. 111.48(a). The reduced values of  $Q^s$  and  $Q^{s,p}$  for smaller  $f_{\text{lim}}$  can be explained by an increased coronal temperature and, as a result, the less-efficient inverse bremsstrahlung absorption. Figure 111.48(b) shows the evolution of the relative difference  $(Q^{s,p} - Q^s)/Q^s$  (solid lines),

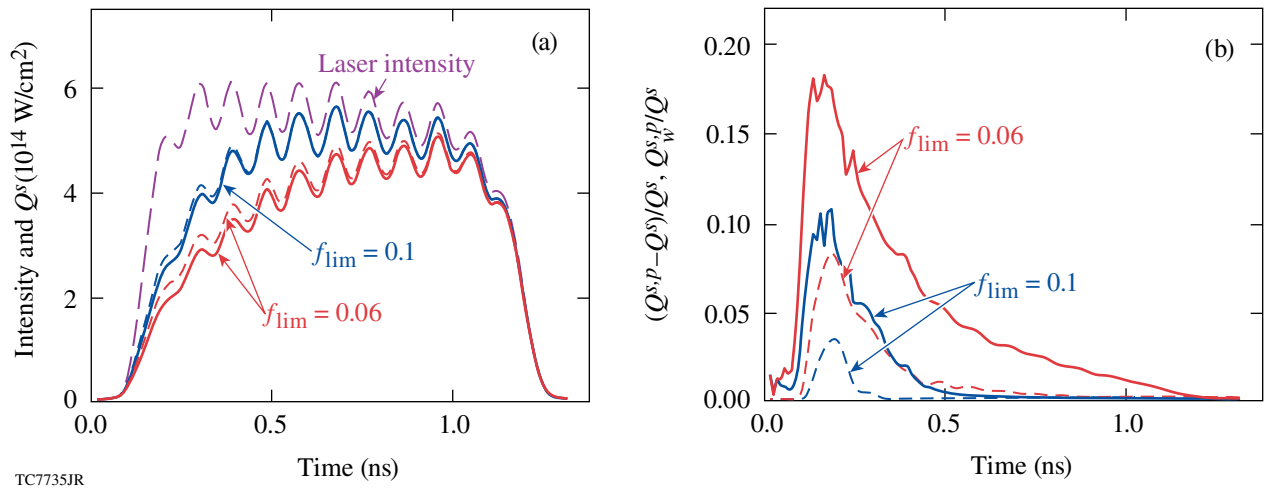


Figure 111.48

Simulated laser-absorption rates for two values of the flux limiter  $f_{lim}$  in the spherical implosion of a CH target driven by a 12.4-kJ, 1-ns OMEGA laser pulse. The approximate method to simulate the laser absorption in spherical implosions is discussed in the text. (a) Drive-laser pulse (long-dashed line) and absorption rates  $Q^s$  (solid lines) and  $Q^{s,p}$  (short-dashed lines), for the  $s$ -polarized and mix-polarized ( $s$  and  $p$ ) lights, respectively. The rate  $Q^s$  does not include the effect of resonant absorption, but  $Q^{s,p}$  does. (b) The relative difference of absorption rates  $(Q^{s,p} - Q^s)/Q^s$  (solid lines) and the relative absorption rates  $Q_w^{s,p}/Q^s$  due to the resonant excitation of Langmuir waves (dashed lines).

which represents the relative effect of resonance absorption, and the ratio  $Q_w^{s,p}/Q^s$  (dashed lines), where  $Q_w^{s,p}$  represents a part of  $Q^{s,p}$  due to the resonant excitation of Langmuir waves. Similar to the planar case (see Fig. 111.46), resonance absorption in spherical targets has a maximum effect at the beginning of the laser pulse, during the first 200 to 400 ps. Also, the resonantly excited Langmuir waves give a noticeable contribution to the total absorption only at the beginning of the laser pulse. The resonance absorption is reduced with an increase in  $f_{lim}$ . This reduction can be explained by an increase in the density scale length near the critical surface with an increase in  $f_{lim}$ . Based on the numerical results presented in Fig. 111.48(a), the effect of resonance absorption can be modeled with the standard laser ray-trace absorption method<sup>26</sup> by adjusting the flux limiter to a higher value (e.g., from the typical  $f_{lim} = 0.06$  to 0.08) during the first  $\sim 200$  ps of the pulse.

The dependence of resonance absorption on laser intensity in spherical implosions is demonstrated in Fig. 111.49 in the case of a 100-ps laser pulse. The pulse shape with a peak intensity of  $5 \times 10^{14}$  W/cm $^2$  (long-dashed line) and calculated absorption rates  $Q^{s,p}$ ,  $Q^s$ , and  $Q_w^{s,p}$  (thick solid, thin solid, and short-dashed lines, respectively) are shown in Fig. 111.49(a). The total absorption fractions calculated using these rates, integrated over the pulse duration, are shown in Fig. 111.49(b) [using the same notations as in Fig. 111.49(a)] as functions of the peak laser intensity. Note that the relative effect of resonant

absorption has a weak dependence on the intensity. Specifically, this effect varies from about 13% to 20% for an intensity varied from  $10^{14}$  to  $10^{15}$  W/cm $^2$ . The contribution of Langmuir waves to the total laser absorption varies from about 2% to 15% for the same range of intensity. Example absorption fractions in spherical implosion experiments on OMEGA employed  $\sim 100$ -ps drive pulses are shown in Fig. 111.49(b) by solid circles.

### Planar Experiments

Two series of planar direct-drive experiments on OMEGA have been proposed to verify the model of resonance absorption presented in **Resonance Absorption in the Fluid Approximation** (p. 180): reflection-light experiments and shock-timing experiments. Both series are based on similar experimental designs employing a single OMEGA laser beam, either  $s$ - or  $p$ -polarized, which irradiates a CH foil. The experiments are designed for beams with  $\theta = 23.2^\circ$ , which is one of the allowed values of  $\theta$ , determined by the construction of the OMEGA target chamber, and close to the angle of the maximum effect of resonance absorption in OMEGA plasmas (see Fig. 111.47). The goal of these experiments is to demonstrate the relative effect of a resonance absorption mechanism by comparing reflection light and shock timing for the case of  $s$ - and  $p$ -polarized laser beams. In this section, the results of the reflection-light experiments are presented and compared with simulations, and the effect of resonance absorption in the proposed shock-timing experimental design is discussed.

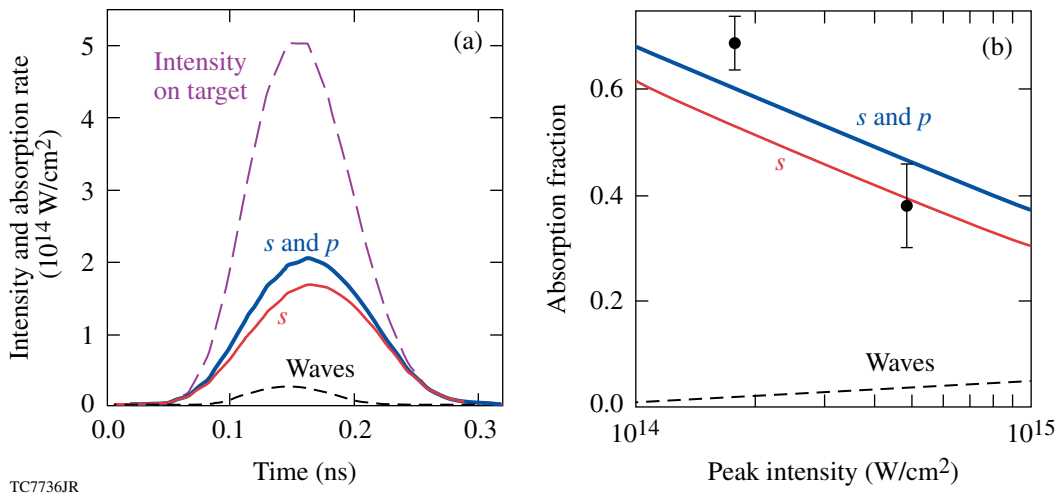


Figure 111.49

Simulated absorption rates and dependence of absorption fractions on the peak laser intensity in spherical implosions of a CH target driven by a 100-ps OMEGA laser pulse. The approximate method to simulate the laser absorption in spherical implosions is discussed in the text. (a) Drive-laser pulse (long-dashed curve); absorption rates calculated using an equal mixture of *s*- and *p*-polarized lights (thick solid line), and using only the *s*-polarized light (thin solid line); absorption rate due to the resonant excitation of Langmuir waves (short-dashed line). (b) Absorption fraction as a function of peak laser intensity for the same cases considered in (a) and in implosion experiments (solid circles), which include a mixture of *s*- and *p*-polarized lights. The effect of resonance absorption is represented by the difference in absorption rates and absorption fractions for the lights with mixed polarization and *s*-polarization.

The setup for the reflection-light experiments is shown schematically in Fig. 111.50. In these experiments, a 200-ps laser beam with an energy of 55 J ( $\pm 5\%$ ) is propagated from port 23 [see Figs. 111.50(a) and 111.50(b)] toward a target and focused into a spot  $\sim 500 \mu\text{m}$  in diameter, resulting in an intensity  $\approx 1.2 \times 10^{14} \text{ W/cm}^2$ . The beam is smoothed in space and time by the spectral dispersion technique<sup>39</sup> and distributed phase plates.<sup>40</sup> The light reflected and scattered from the target is collected by three calorimeters located in ports 25, 17, and 30. The calorimeter in port 25 collects the specularly reflected light, whereas the other two calorimeters, in ports 17 and 30, collect the scattered light at about  $23^\circ$  from the direction to port 25. The calorimeter in port 17 is located on the target normal.

Table 111.V shows the beam energy along with the energy collected by the three calorimeters in two experiments with single *s*- and *p*-polarized OMEGA laser beams. In agreement with theory, which predicts smaller light reflection from the *p*-polarized beam, the energy reflected from the *s*-polarized beam exceeds the energy reflected from the *p*-polarized beam (both energies collected in port 25). Quantitatively, the experiments show a larger difference in these energies: the corresponding energy ratio is 2.5 versus 1.8 obtained in simulations. Figure 111.51 shows time-resolved reflected power in the experiments and simulations, where the simulation data (thin solid lines) are given in  $\text{W/cm}^2$  and the experimental data

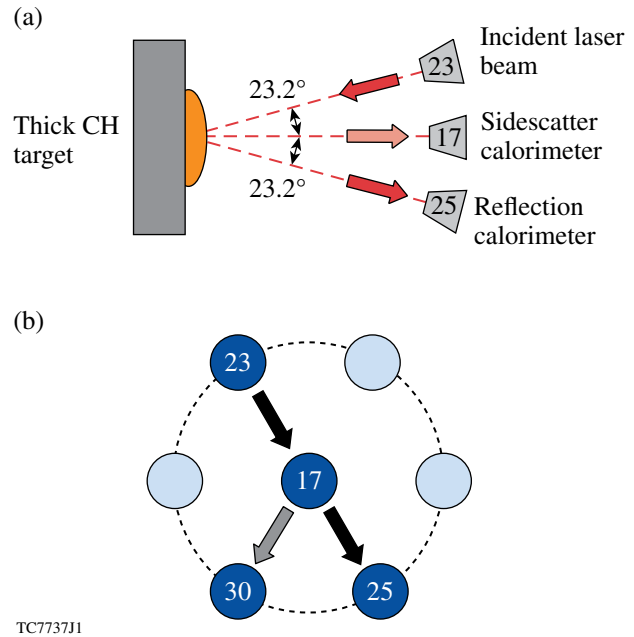


Figure 111.50

(a) Experimental setup for the reflection-light measurements, using single laser beams of *s*- or *p*-polarization. Port 17 is on the direction of target normal. (b) View of the OMEGA ports used in the experiment. Port 30 is not depicted in (a).

Table 111.V: Reflection- and scattered-light measurements. The experimental setup is illustrated in Fig. 111.50.

Beam polarization	Beam energy (J)	Collected Energy (J)		
		Port 25	Port 30	Port 17
<i>s</i>	52.5	1.59	0.15	0.14
<i>p</i>	57.1	0.63	0.17	0.22

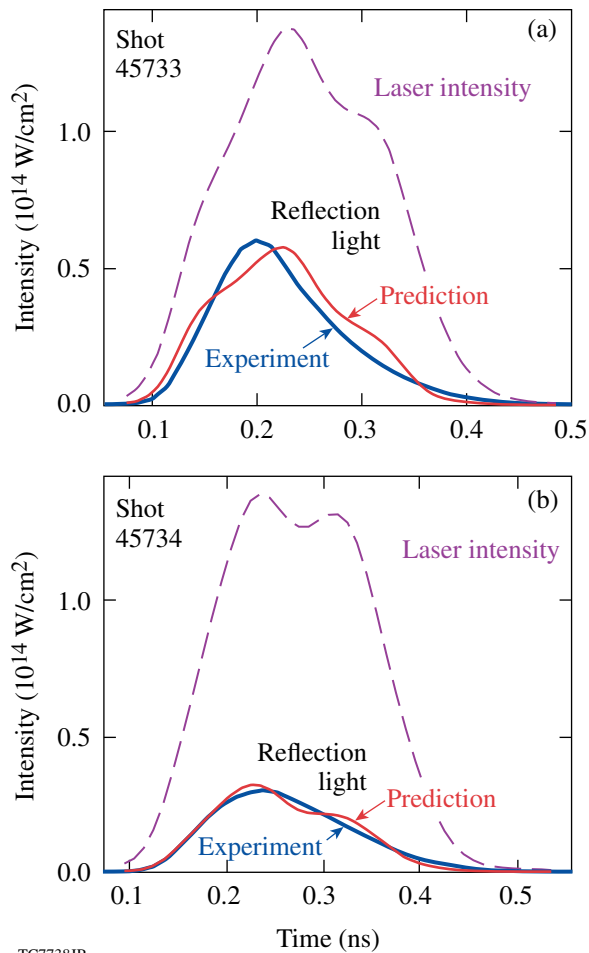


Figure 111.51 Time-resolved measured (thick solid lines) and simulated (thin solid lines) intensities of reflection light in the experiments illustrated in Fig. 111.50. The cases of (a) *s*-polarized and (b) *p*-polarized beams are shown. The incident laser intensities (in W/cm<sup>2</sup>) are shown by the dashed lines. The simulated reflection data are presented in W/cm<sup>2</sup>, whereas the experimental data are given in arbitrary normalizations.

(thick solid lines) use arbitrary normalizations. Note a good agreement of time profiles of the experimental and simulated energy fluxes in both cases of *s*- and *p*-polarized beams.

The reflection experiments revealed significant sidescatter of laser light in both cases of *s*- and *p*-polarized beams. Due to this scatter, the measured reflection energies are about an order of magnitude smaller than the values predicted in simulations. An estimate using the amount of energy scattered in ports 17 and 30 (see Table 111.V) and assuming a uniform scatter suggests that the total scattered energy exceeds the reflection energy by at least a factor of 20. A possible explanation for this scatter is the development of laser-induced perturbations of the reflection surface in plasma corona. These perturbations, or nonuniformities, can have spatial scales comparable to the laser wavelength and cause significant sidescatter of laser light if the amplitude of perturbations is large enough. The 1-D model of resonance absorption used in this article cannot consider perturbations in the transverse directions to the target normal and, therefore, cannot simulate such a scatter.

The early-time enhancement of laser absorption due to the resonance mechanism can affect the velocities of shocks originating at initial stages of implosions. A change in these velocities can be important for high-gain, direct-drive implosion designs that utilize adiabat-shaping techniques.<sup>10,11</sup> Shock-timing experiments, somewhat analogous to the shock-compressibility experiments,<sup>41</sup> can be suitable for the study of the effect of resonance absorption on shock properties.

The shock-timing experimental design uses a setup similar to that used in the reflection-light experiments (see Fig. 111.50). The measured quantity in this design is the velocity of shocks driven by the laser beams with different polarization. The effect of resonance absorption is estimated by comparing the shock-breakout times in finite-thickness targets in experiments with *s*- and *p*-polarized beams. On OMEGA, the shock-breakout time can be measured to an accuracy of about 50 ps by using two independent techniques: one that employs a velocity interferometer system for any reflector (VISAR),<sup>42,43</sup> and another that utilizes temporal records of the shock-front self-emission (600 to 1000 nm) acquired using an imaging streak camera.<sup>44</sup>

Figure 111.52 shows simulated time-dependent travel distances for two shocks driven by *s*- and *p*-polarized laser beams in thick CH targets. The simulations assume a 100-ps laser pulse, similar to one shown in Fig. 111.47(a), but with a peak intensity of 10<sup>14</sup> W/cm<sup>2</sup>. For a fixed travel distance, which corresponds to an assumed target thickness in experiments, the

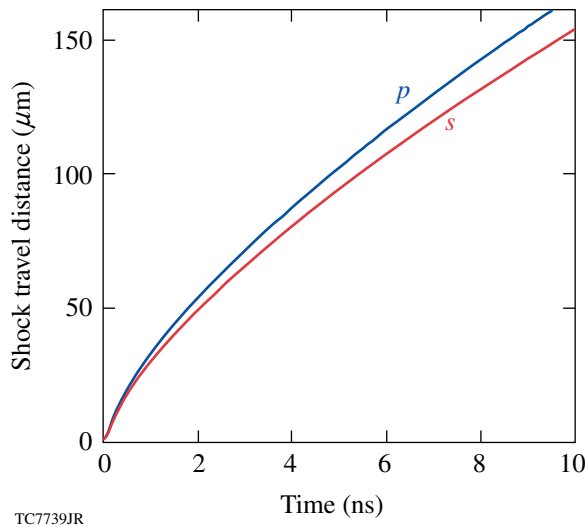


Figure 111.52

Simulated time dependence of the travel distance of shocks driven by single 100-ps OMEGA laser beams of different polarizations in thick CH foils. The beams have a peak intensity of  $10^{14}$  W/cm<sup>2</sup> and  $\theta = 23.2^\circ$ . Two cases of *s*- and *p*-polarized beams (marked by “*s*” and “*p*”, respectively) are considered.

difference  $\Delta t$  between the propagation time of the two shocks corresponds to the difference of experimentally measured breakout time in the case of *s*- and *p*-polarized beams. The value  $\Delta t$  exceeds the experimental accuracy limit of 50 ps for targets thicker than 30  $\mu\text{m}$ , and  $\Delta t$  is in the well-detectable range of several hundred picoseconds for target thicknesses  $\geq 100$   $\mu\text{m}$ . Specifically, one gets  $\Delta t \approx 800$  ps for a 125- $\mu\text{m}$ -thick target.

### Discussion and Conclusions

The effect of resonance absorption in a CH plasma has been investigated theoretically and experimentally for the physical conditions relevant to direct-drive ICF experiments with a 351-nm laser and intensities in the range of  $10^{14}$  to  $10^{15}$  W/cm<sup>2</sup>. It has been shown that nonlinear effects, such as pondermotive force and wave breaking, are not important; therefore, the linear theory of resonance absorption has been used in the 1-D hydrodynamic code *LILAC* to construct numerical models. The resonant excitation of Langmuir waves at the critical surface is an important mechanism that contributes to resonance absorption and dominates inverse bremsstrahlung absorption in the case of laser intensities  $\geq 5 \times 10^{14}$  W/cm<sup>2</sup> and angles of incidence of laser beams in the optimum range,  $10^\circ \leq \theta \leq 30^\circ$ . The decay of Langmuir waves caused by Landau damping results in a release of wave energy in the form of hot electrons with temperature  $\approx 5$  keV, which is larger by a factor

of 2 to 5 than the electron temperature in hot corona, where  $T_e \approx 1$  to 2 keV. This could lead to a deviation of the electron distribution function from Maxwellian in hot corona if the energy released in hot electrons is relatively large. In implosion experiments on OMEGA, however, this energy is predicted to be relatively low [less than 15% of the total absorbed energy (see the short-dashed lines in Fig. 111.49)], so that the coronal plasma there is expected to be nearly Maxwellian.

On OMEGA, resonance absorption has a maximum effect during a rapid increase in laser power, typically  $\sim 100$  ps. Simulations show that the resonance absorption in a 1-ns square laser pulse can be important only during the first 200 to 300 ps. At this initial period, the density scale length in plasma near the critical surface is relatively short,  $\sim 1$  to 2  $\mu\text{m}$ , resulting in enhanced resonance absorption. At later times, when the laser power reaches its maximum, the density scale length increases to more than 5  $\mu\text{m}$ , causing significant reduction in resonance absorption. In short laser pulses, or pickets,  $\sim 100$  ps, the resonance absorption has a maximum relative effect, the value of which depends on the intensity and angle of incidence of the laser. In the case of spherical implosions, the predicted relative effect of resonance absorption varies from about 13% to 20% for intensities between  $10^{14}$  and  $10^{15}$  W/cm<sup>2</sup>.

We suggest, based on our numerical results, that the resonance absorption in spherical implosions can be modeled with the standard laser ray-trace method,<sup>26</sup> using a time-variable flux limiter, the value of which is increased by  $\sim 30\%$  during the first  $\sim 200$  ps of the laser pulse.

Planar reflection-light experiments have been conducted on OMEGA to verify the theoretical predictions of resonance absorption. These experiments used CH foils irradiated by single *s*- and *p*-polarized laser beams with an angle of incidence  $\theta = 23.2^\circ$  and showed the reflection energy's clear dependence on polarization, in good quantitative agreement with simulation results. The experiments also revealed significant sidescatter of laser light, which reduces the amount of reflection energy by about an order of magnitude in comparison with simulations. This sidescatter, affecting both *s*- and *p*-polarized lights, can be explained by laser-induced perturbations in the reflection surface of plasma corona. The effect of these perturbations cannot be accounted for in the simplified 1-D approach used in this study. We expect that the surface perturbations could reduce the difference between reflected *s*- and *p*-polarized laser lights predicted in simulations because of the introduction of additional polarization components (mixed *s*- and *p*-polarized lights) in the incident laser beams.

Another OMEGA planar, direct-drive experiment that could demonstrate the effect of resonance absorption in laser-driven shocks has been designed and simulated. This design employs CH foils irradiated by single *s*- or *p*-polarized laser beams that initiate shocks with different velocities. The effect of resonance absorption is inferred by comparing the shock-breakout time at the target's rear surface in the case of *s*- and *p*-polarized beams. Assuming a 100-ps laser pulse with a peak intensity of  $10^{14}$  W/cm<sup>2</sup>, the simulations predict a time difference of shock breakout in the well-detectable range of several hundred picoseconds for a target thickness of about 100  $\mu$ m.

#### ACKNOWLEDGMENT

This work was supported by the U.S. Department of Energy (DOE) Office of Inertial Confinement Fusion under Cooperative Agreement No. DE-FC52-92SF19460, the University of Rochester, the New York State Energy Research and Development Authority.

#### REFERENCES

1. J. D. Lindl, *Inertial Confinement Fusion: The Quest for Ignition and Energy Gain Using Indirect Drive* (Springer-Verlag, New York, 1998), pp. 39–52.
2. S. Atzeni and J. Meyer-ter-Vehn, *The Physics of Inertial Fusion: Beam Plasma Interaction, Hydrodynamics, Hot Dense Matter*, International Series of Monographs on Physics (Clarendon Press, Oxford, 2004), pp. 38–41 and 366.
3. R. L. McCrory, J. M. Soures, C. P. Verdon, F. J. Marshall, S. A. Letzring, S. Skupsky, T. J. Kessler, R. L. Kremens, J. P. Knauer, H. Kim, J. Delettrez, R. L. Keck, and D. K. Bradley, *Nature* **335**, 225 (1988).
4. S. E. Bodner, D. G. Colombant, J. H. Gardner, R. H. Lehmburg, S. P. Obenschain, L. Phillips, A. J. Schmitt, J. D. Sethian, R. L. McCrory, W. Seka, C. P. Verdon, J. P. Knauer, B. B. Afeyan, and H. T. Powell, *Phys. Plasmas* **5**, 1901 (1998).
5. P. W. McKenty, V. N. Goncharov, R. P. J. Town, S. Skupsky, R. Betti, and R. L. McCrory, *Phys. Plasmas* **8**, 2315 (2001).
6. P. W. McKenty, T. C. Sangster, M. Alexander, R. Betti, R. S. Craxton, J. A. Delettrez, L. Elasky, R. Epstein, A. Frank, V. Yu. Glebov, V. N. Goncharov, D. R. Harding, S. Jin, J. P. Knauer, R. L. Keck, S. J. Loucks, L. D. Lund, R. L. McCrory, F. J. Marshall, D. D. Meyerhofer, S. P. Regan, P. B. Radha, S. Roberts, W. Seka, S. Skupsky, V. A. Smalyuk, J. M. Soures, K. A. Thorp, M. Wozniak, J. A. Frenje, C. K. Li, R. D. Petrasso, F. H. Séguin, K. A. Fletcher, S. Padalino, C. Freeman, N. Izumi, J. A. Koch, R. A. Lerche, M. J. Moran, T. W. Phillips, G. J. Schmid, and C. Sorce, *Phys. Plasmas* **11**, 2790 (2004).
7. R. L. McCrory, S. P. Regan, S. J. Loucks, D. D. Meyerhofer, S. Skupsky, R. Betti, T. R. Boehly, R. S. Craxton, T. J. B. Collins, J. A. Delettrez, D. Edgell, R. Epstein, K. A. Fletcher, C. Freeman, J. A. Frenje, V. Yu. Glebov, V. N. Goncharov, D. R. Harding, I. V. Igumenshchev, R. L. Keck, J. D. Kilkenny, J. P. Knauer, C. K. Li, J. Marcianti, J. A. Marozas, F. J. Marshall, A. V. Maximov, P. W. McKenty, J. Myatt, S. Padalino, R. D. Petrasso, P. B. Radha, T. C. Sangster, F. H. Séguin, W. Seka, V. A. Smalyuk, J. M. Soures, C. Stoeckl, B. Yaakobi, and J. D. Zuegel, *Nucl. Fusion* **45**, S283 (2005).
8. M. C. Herrmann, M. Tabak, and J. D. Lindl, *Nucl. Fusion* **41**, 99 (2001).
9. R. Betti, K. Anderson, V. N. Goncharov, R. L. McCrory, D. D. Meyerhofer, S. Skupsky, and R. P. J. Town, *Phys. Plasmas* **9**, 2277 (2002).
10. V. N. Goncharov, J. P. Knauer, P. W. McKenty, P. B. Radha, T. C. Sangster, S. Skupsky, R. Betti, R. L. McCrory, and D. D. Meyerhofer, *Phys. Plasmas* **10**, 1906 (2003).
11. K. Anderson and R. Betti, *Phys. Plasmas* **10**, 4448 (2003).
12. T. R. Boehly, D. L. Brown, R. S. Craxton, R. L. Keck, J. P. Knauer, J. H. Kelly, T. J. Kessler, S. A. Kumpan, S. J. Loucks, S. A. Letzring, F. J. Marshall, R. L. McCrory, S. F. B. Morse, W. Seka, J. M. Soures, and C. P. Verdon, *Opt. Commun.* **133**, 495 (1997).
13. N. G. Denisov, *Sov. Phys.-JETP* **4**, 544 (1957).
14. P. Hirsch and J. Shmoys, *Radio Sci. J. Res. NBS/USNC-URSI* **69D**, 521 (1965).
15. A. D. Piliya, *Sov. Phys.-Tech. Phys.* **11**, 609 (1966).
16. A. Ya. Omel'chenko and K. N. Stepanov, *Ukr. Fiz. Zh.* **12**, 1396 (1967).
17. T. Tang, *Radio Sci.* **5**, 111 (1970).
18. V. L. Ginzburg, *The Propagation of Electromagnetic Waves in Plasmas* (Pergamon Press, New York, 1970), pp. 319–438.
19. D. W. Forslund *et al.*, *Phys. Rev. A* **11**, 679 (1975).
20. T. Speziale and P. J. Catto, *Phys. Fluids* **20**, 990 (1977).
21. G. J. Pert, *Phys. Plasmas* **20**, 175 (1978).
22. R. W. Means *et al.*, *Phys. Fluids* **24**, 2197 (1981).
23. D. E. Hinkel-Lipsker, B. D. Fried, and G. J. Morales, *Phys. Fluids B* **4**, 559 (1992).
24. D. E. Hinkel-Lipsker, B. D. Fried, and G. J. Morales, *Phys. Fluids B* **4**, 1772 (1992); D. E. Hinkel-Lipsker, B. D. Fried, and G. J. Morales, *Phys. Fluids B* **5**, 1746 (1993).
25. H. Xu *et al.*, *Phys. Plasmas* **13**, 123301 (2006).
26. J. Delettrez, R. Epstein, M. C. Richardson, P. A. Jaanimagi, and B. L. Henke, *Phys. Rev. A* **36**, 3926 (1987); J. Delettrez, *Can. J. Phys.* **64**, 932 (1986).
27. W. L. Kruer, *The Physics of Laser-Plasma Interactions*, *Frontiers in Physics*, Vol. 73, edited by D. Pines (Addison-Wesley, Redwood City, CA, 1988), Chap. 4, pp. 39–43.
28. F. F. Chen, *Introduction to Plasma Physics and Controlled Fusion*, 2nd ed., Vol. 1 (Plenum Press, New York, 1984), p. 87.

29. E. M. Lifshitz and L. P. Pitaevskii, *Physical Kinetics*, 1st ed., Course of Theoretical Physics, Vol. 10 (Pergamon Press, Oxford, 1981), pp. 124–127.
30. W. H. Press *et al.*, *Numerical Recipes in FORTRAN: The Art of Scientific Computing*, 2nd ed. (Cambridge University Press, Cambridge, England, 1992), pp. 34–38.
31. L. Spitzer, Jr. and R. Härm, *Phys. Rev.* **89**, 977 (1953).
32. A. B. Langdon, *Phys. Rev. Lett.* **44**, 575 (1980).
33. A. Sunahara, J. A. Delettrez, C. Stoeckl, R. W. Short, and S. Skupsky, *Phys. Rev. Lett.* **91**, 095003 (2003).
34. G. P. Schurtz, Ph. D. Nicolaï, and M. Busquet, *Phys. Plasmas* **7**, 4238 (2000).
35. V. N. Goncharov, O. V. Gotchev, E. Vianello, T. R. Boehly, J. P. Knauer, P. W. McKenty, P. B. Radha, S. P. Regan, T. C. Sangster, S. Skupsky, V. A. Smalyuk, R. Betti, R. L. McCrory, D. D. Meyerhofer, and C. Cherfils-Clérouin, *Phys. Plasmas* **13**, 012702 (2006).
36. S. Skupsky, R. W. Short, T. Kessler, R. S. Craxton, S. Letzring, and J. M. Soures, *J. Appl. Phys.* **66**, 3456 (1989).
37. T. P. Coffey, *Phys. Fluids* **14**, 1402 (1971).
38. S. P. Regan, J. A. Marozas, R. S. Craxton, J. H. Kelly, W. R. Donaldson, P. A. Jaanimagi, D. Jacobs-Perkins, R. L. Keck, T. J. Kessler, D. D. Meyerhofer, T. C. Sangster, W. Seka, V. A. Smalyuk, S. Skupsky, and J. D. Zuegel, *J. Opt. Soc. Am. B* **22**, 998 (2005).
39. S. Skupsky and R. S. Craxton, *Phys. Plasmas* **6**, 2157 (1999).
40. Y. Lin, T. J. Kessler, and G. N. Lawrence, *Opt. Lett.* **21**, 1703 (1996).
41. T. R. Boehly, E. Vianello, J. E. Miller, R. S. Craxton, T. J. B. Collins, V. N. Goncharov, I. V. Igumenshchev, D. D. Meyerhofer, D. G. Hicks, P. M. Celliers, and G. W. Collins, *Phys. Plasmas* **13**, 056303 (2006).
42. L. M. Barker and R. E. Hollenbach, *J. Appl. Phys.* **43**, 4669 (1972).
43. P. M. Celliers, D. K. Bradley, G. W. Collins, D. G. Hicks, T. R. Boehly, and W. J. Armstrong, *Rev. Sci. Instrum.* **75**, 4916 (2004).
44. J. E. Miller, T. R. Boehly, E. Vianello, W. J. Armstrong, C. Sorce, W. Theobald, D. D. Meyerhofer, D. G. Hicks, J. H. Eggert, and P. M. Celliers, *Bull. Am. Phys. Soc.* **50**, 60 (2005); J. A. Oertel *et al.*, *Rev. Sci. Instrum.* **70**, 803 (1999).

# Diagnosing Direct-Drive, Shock-Heated, and Compressed Plastic Planar Foils with Noncollective Spectrally Resolved X-Ray Scattering

## Introduction

The achievement of energy gain with a direct-drive inertial confinement fusion (ICF) ignition target requires an accurate prediction of the shock-heated and compressed conditions in the main fuel layer.<sup>1</sup> A direct-drive ICF target for hot-spot ignition consists of a spherical cryogenic main fuel layer of deuterium and tritium surrounded by a thin plastic layer.<sup>1–3</sup> Intense laser beams uniformly irradiate the target and launch a shock wave through the main fuel layer. The pressure in the shock-heated shell determines the implosion performance of the target. The laser pulse for a direct-drive implosion consists of a low-intensity foot and high-intensity main drive. The low-intensity foot launches a relatively weak shock to isentropically compress the target, and the main drive sends a compression wave that implodes the target to form a central hot spot with sufficient fuel areal density and temperature to ignite the target. The entropy of the main fuel layer or shell adiabat  $\alpha$  is defined as the ratio of the pressure in the main fuel layer to the Fermi-degenerate pressure. It is a critical parameter in ICF because it is related to the minimum laser drive energy needed for ignition and the growth rate of the Rayleigh–Taylor (RT) hydrodynamic instability.<sup>4,5</sup> The RT instability distorts the uniformity of the implosion, reduces the target compression, and could prevent hot-spot formation.<sup>6</sup> Therefore, the successful target design for a stable, high-performance ICF implosion creates an adiabat in the shell that strikes a balance between the target stability and the laser-energy requirements.

The shock-heated shell in direct-drive ICF is predicted to have plasma conditions in the warm dense matter (WDM) regime.<sup>7</sup> The coupling parameter<sup>8</sup>  $\Gamma$  and ratio of Fermi temperature to electron temperature  $\Theta$  characterize plasmas in  $T_e$ – $n_e$  space. The electron–electron coupling parameter  $\Gamma_{ee}$  is the ratio of Coulomb potential between free electrons to the average kinetic energy of the free electrons:

$$\Gamma_{ee} = \frac{e^2}{dk_B T_e}, \quad (1)$$

where  $d = (3/4\pi n_e)^{1/3}$  is the average interparticle spacing. When a plasma is strongly coupled ( $\Gamma_{ee} \gg 1$ ), the Coulomb interac-

tions between particles determine the physical properties of the plasma. When  $\Gamma_{ee} \ll 1$ , plasma behaves as an ideal gas and the interparticle coupling is insignificant. Similar considerations can be made with regards to the electron–ion and ion–ion coupling parameters.<sup>8</sup> In an ICF implosion, the shock-heated shell becomes a partially or fully degenerate plasma. The degree of degeneracy is described as

$$\Theta = T_F/T_e, \quad (2)$$

where  $T_F$  is the Fermi temperature [ $T_F = \hbar^2(3\pi^2 n_e)^{2/3}/2m_e k_B$ ,  $k_B$  is the Boltzmann constant]. In degenerate plasmas, the electron energy depends only on  $n_e$ , and the coupling constant is defined as the ratio between the potential and Fermi energy ( $\Gamma_{ee} = e^2/dE_F$ ). Figure 111.53 shows  $T_e$ – $n_e$  space characterized by the electron coupling parameter,  $\Gamma_{ee}$ ; the ratio of the  $T_e$  and  $T_F$ ,  $\Theta(T_F/T_e)$ ; the average interparticle spacing  $d = (3/4\pi n_e)^{1/3}$ ; and the Debye length  $\lambda_D$ . The plane is divided by the lines  $\Theta = 1$ ,  $\Gamma_{ee} = 1$ , and  $d = \lambda_D$  into regions where Fermi-degenerate, strongly coupled, Fermi-degenerate and strongly coupled, weakly coupled, and ideal plasmas exist. As shown in Fig. 111.53, the predicted conditions for the direct-drive experiments (see triangle symbols) lie in the WDM regime on the boundary between Fermi-degenerate, strongly coupled, and weakly coupled plasmas.

Diagnosing WDM is challenging because the temperature of the plasma is too low ( $\sim 10$  eV) for it to emit x rays and dense plasmas above the critical density cannot be probed with optical lasers for Thomson-scattering measurements.<sup>9</sup> Two viable techniques exist to diagnose these plasmas: spectrally resolved x-ray scattering<sup>10</sup> and time-resolved x-ray absorption spectroscopy.<sup>11</sup> X-ray absorption spectroscopy measurements provide time-resolved local measurements of the plasma conditions in the shock-heated foil; they require, however, a buried mid-Z tracer layer such as Al. The Al  $1s$ – $2p$  absorption spectroscopy was used to diagnose similar plasma conditions in a direct-drive, shock-heated CH planar foil by using a point-source Sm backlighter.<sup>12</sup> The spectrally resolved x-ray scattering does not require a tracer layer; it requires, however, a large volume of shock-heated matter to scatter a sufficient number of x rays,

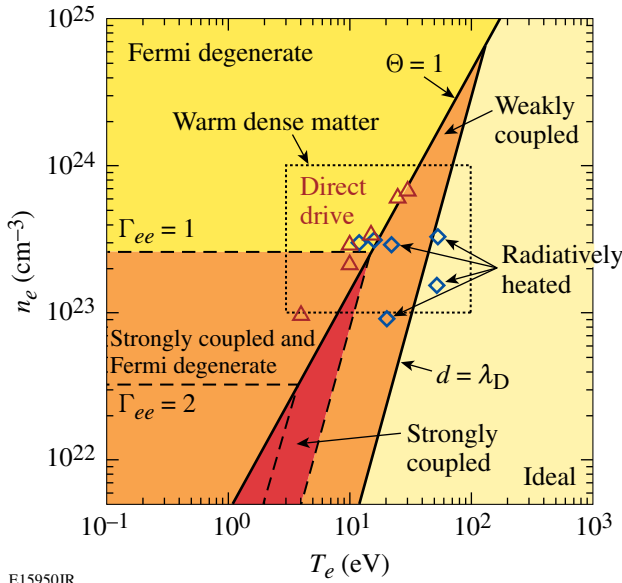


Figure 111.53

$T_e$ - $n_e$  space characterized by the electron coupling parameter  $\Gamma_{ee}$ : the ratio of the Fermi temperature  $T_F$  and the electron temperature  $T_e$ ,  $\Theta (= T_F/T_e)$ ; the average interparticle spacing  $d [= (3/4\pi n_e)^{1/3}]$ ; and Debye length  $\lambda_D$ . The plane is divided by the lines  $\Theta = 1$ ,  $\Gamma_{ee} = 1$ , and  $d = \lambda_D$  into regions where Fermi-degenerate, strongly coupled, Fermi-degenerate and strongly coupled, weakly coupled, and ideal plasmas exist. Predicted conditions of direct-drive, shock-heated experiments are shown as triangle symbols. Plasma conditions of radiatively heated targets inferred with noncollective and collective spectrally resolved x-ray scattering are shown as the diamond symbols.

limiting its spatial resolution. Noncollective spectrally resolved x-ray scattering experiments reported in the literature have characterized the plasma conditions of an isochorically heated Be cylinder, a carbon foam, and a CH gas bag.<sup>13</sup> Recently, collective scattering was observed from an isochorically heated Be cylinder and was used to infer the electron density.<sup>14</sup> In principle, when collective scattering is used in conjunction with noncollective scattering, the spatially averaged quantities of electron density, electron temperature, and ionization can be diagnosed. The radiatively heated plasmas conditions are shown as the diamond symbols in Fig. 111.53.

Diagnosing plasmas that have conditions comparable to those in the shock-heated main fuel layer of a direct-drive ICF ignition target is the central focus of this article. For the first time, noncollective, spectrally resolved x-ray scattering is used to probe the plasma conditions in direct-drive, shock-heated planar plastic foils. Compared to x-ray scattering measurements from isochorically heated targets, direct-drive targets present new experimental challenges associated with the smaller physical dimensions of the target and gradients in the plasma conditions, as well as target compression and acceleration during the

scattering measurements. The scattering volumes and hence the scattered x-ray signal level of direct-drive targets are at least an order of magnitude smaller compared to the radiatively heated targets. Some direct-drive scenarios shape the adiabat in the target, which would require a spatially resolved and spectrally resolved x-ray scattering diagnostic. The direct-drive coronal plasma is in close proximity to the scattering volume and creates a major source of unwanted background x-ray continuum, which must be shielded from the detector. However, the target trajectory moves the coronal plasma into the field of view of the detector during the scattering measurement. Plastic foils are surrogates for cryogenic fuel layers. These results, required for ICF ignition, provided an opportunity to study the shell conditions of a direct-drive ICF imploded target without the cost and complexity of cryogenic hardware. The spectral line shapes of the elastic Rayleigh and the inelastic Compton components are fit to infer the electron temperature  $T_e$  and ionization  $Z$ : the Doppler-broadened Compton feature is sensitive to  $T_e$  for  $T_e$  greater than the Fermi temperature  $T_F$ , and the ratio of the Rayleigh and the Compton components is sensitive to  $Z$ .

The following sections of this article (1) describe spectrally resolved x-ray scattering; (2) present the experimental setup and simulations from the 1-D hydrodynamics code; (3) present the experimental results and compare them with the predicted plasma conditions; and (4) discuss the future use of spectrally resolved x-ray scattering to infer the plasma conditions in the main fuel layer of a direct-drive inertial confinement fusion target.

### Spectrally Resolved X-Ray Scattering

Scattering processes are classified as collective or noncollective based on the scattering parameter, defined as

$$\alpha_{\text{scatter}} = \frac{1}{k\lambda_D} = \frac{1.08 \times 10^{-4} \cdot \lambda_0(\text{cm})}{\sin(\theta/2)} \left[ \frac{n_e(\text{cm}^{-3})}{T_{\text{eff}}(\text{eV})} \right]^{1/2}, \quad (3)$$

where  $\theta$  is the scattering angle,  $k$  is the wave number of scattered x rays [ $k = 4\pi/\lambda_0 \cdot \sin(\theta/2)$ ],  $\lambda_0$  is the probe wavelength, and  $\lambda_D$  is the Debye length calculated with the effective temperature<sup>15</sup>  $T_{\text{eff}}$ , which is defined as  $T_{\text{eff}} = \sqrt{T_e^2 + T_q^2}$ , where  $T_q = T_F/(1.33 - 0.18\sqrt{r_s})$  with  $r_s = d/a_B$  ( $a_B$  is the Bohr radius).<sup>16</sup> The characteristic plasma length in the scattering parameter,  $\lambda_D$ , in Eq. (3) is replaced by the Thomas-Fermi screening length

$$\lambda_{\text{TF}} (= \sqrt{2\epsilon_0 E_F / 3n_e e^2})$$

for Fermi-degenerate plasma, and by the interparticle spacing  $d$  for strongly coupled plasma. With the use of the effective

temperature, the scattering parameter between ideal, strongly coupled, and Fermi-degenerate regimes is smoothly interpolated. For noncollective scattering ( $\alpha_{\text{scatter}} < 1$ ), x rays are scattered by individual electrons. As a result, the red wing of the Compton component in the scattered spectrum reflects the free electron velocity distribution function,<sup>17</sup> and the Doppler-broadened spectrum is sensitive to  $T_e$  for  $T_e > T_F$ . When  $T_e < T_F$ , the electron distribution becomes a Fermi distribution and its spectral shape is only weakly sensitive to the electron density. All of the scattering investigated in this article is noncollective. In the case of  $\alpha_{\text{scatter}} > 1$ , the incident x-ray photons interact with a collective electron cloud; in particular, collective scattering is of interest for electron-density measurements.<sup>14,18</sup>

Detailed calculations of the modeled x-ray scattering spectra presented here can be found in Refs. 13, 19, 20, and 21. A brief description of the model is given in this section. Spectrally resolved x-ray scattering can be modeled with the total dynamic structure factor in the differential scattering cross section. As derived by Chihara,<sup>22,23</sup> the total dynamic structure factor and the free-electron correlation function are written as

$$S(k, \omega) = |f_1(k) + q(k)|^2 S_{ii}(k, \omega) + Z_f S_{ee}^0(k, \omega) + Z_b \int \tilde{s}_{ce}(k, \omega - \omega') S_s(k, \omega') d\omega', \quad (4)$$

$$S_{ee}^0(k, \omega) = - \frac{\hbar}{1 - \exp(-\hbar \omega / k_B T_e)} \frac{\epsilon_0 k^2}{\pi e^2 n_e} \text{Im} \left[ \frac{1}{\epsilon(k, \omega)} \right]. \quad (5)$$

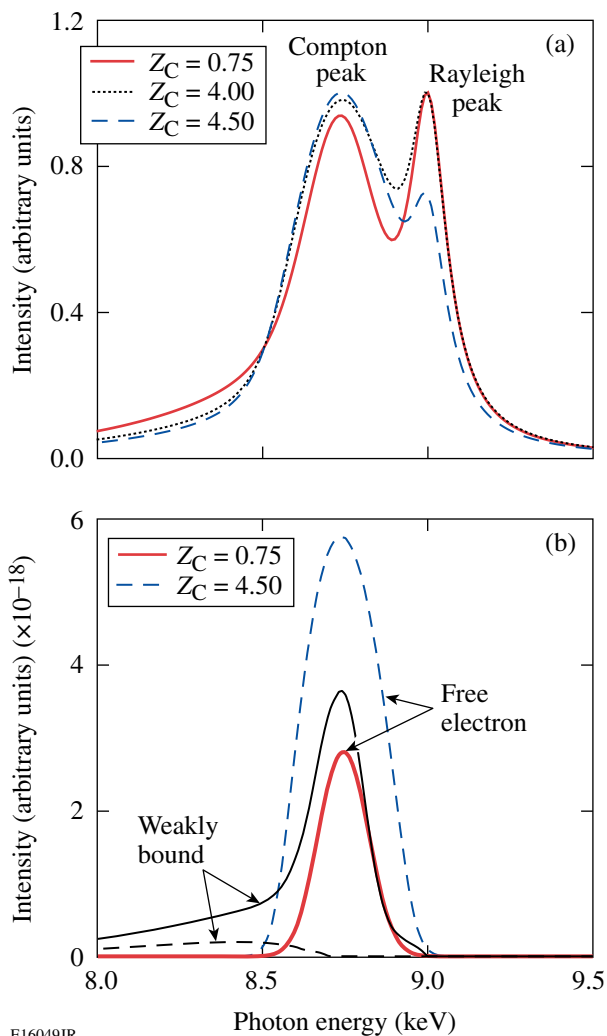
Although Eq. (4) is valid only for a single-ion component plasma, the model for the experiment under consideration includes the scattering contribution from all ion species as well as their mutual correlations as described by Gregori *et al.*<sup>13</sup> The first term on the right-hand side of Eq. (4) corresponds to the elastic Rayleigh-scattering component.  $f_1(k)$  is the ionic form factor for bound electrons and  $q(k)$  is the Fourier transform of the free-electron cloud surrounding the ion.  $S_{ii}(k, \omega)$  is the ion–ion dynamic structure factor, which describes the degree of ion–ion correlations.

In Eq. (4)  $Z_f$  and  $Z_b$  are the number of free (or valence) electrons and bound electrons, respectively. The number of electrons associated with each atom,  $Z_A$ , is the sum of  $Z_f$  and  $Z_b$ .  $Z_f$  represents electrons that are not bound to any single atom or ion including valence, delocalized, or conduction electrons. These electrons are all described in terms of plane-wave or Bloch wave functions. From a hydrodynamic perspective the useful

quantity to compare with numerical modeling is the number of free electrons or the average ionization  $Z$ , not  $Z_f$ . From the discussion above,  $Z_f$  differs from  $Z$  because it includes valence states together with kinematically free electrons. For the case of cold (undriven) plastic foil targets,  $Z_f$  is just the number of valence electrons and has no relation to  $Z$ . On the other hand, as soon as the temperature in the plastic foil is raised by the laser interaction, atomic bonds are broken and the underlying lattice responsible for the formation of the valence band is destroyed. In this case  $Z_f$  can be identified with  $Z$  and direct comparison with simulations is possible. The second term in Eq. (4) thus represents scatterings from either free or valence electrons that move independently from the ions. As shown in Eq. (5), their corresponding electron–electron correlation function  $S_{ee}^0(k, \omega)$  can be obtained through the fluctuation–dissipation theorem<sup>24</sup> in terms of the electron dielectric response function derived using the random phase approximation (RPA).<sup>25,26</sup> The RPA is accurate without any local field corrections in our noncollective scattering experiment. While the RPA is rigorously valid for kinematically free electrons, valence electrons can also be described in a similar way.<sup>27</sup> Extension to a finite band gap is also possible, but its effect is small for the conditions of this experiment.<sup>19</sup> The last term of Eq. (4) contributes to inelastic scattering from core electrons. Differently from valence and free electrons, electrons bound to localized levels in the L or K shells are treated as hydrogenic states in terms of a modified impulse approximation,<sup>28</sup> which was shown to reproduce well experimental x-ray scattering data from shock-compressed Al plasmas;<sup>29</sup> these are the bound electrons included in  $Z_b$ . This term becomes important when L-shell bound electrons are involved in the scattering process, which is the case for a carbon-hydrogen plasma, created by the laser-induced ionization of a CH ( $C_8H_8$ ) planar target. The average number of free (or valence) electrons for CH is given by

$$Z_f = \frac{Z_C + Z_H}{2} = \frac{(6 - Z_b)_C + (1 - Z_b)_H}{2}, \quad (6)$$

where  $Z_C$  and  $Z_H$  are the number of delocalized electrons in carbon and hydrogen, respectively. Figure 111.54 shows the modeled scattered spectra for CH foils using Eq. (4). Figure 111.54(a) shows the calculated total spectra including free electrons, weakly bound electrons, and tightly bound electrons. Figure 111.54(b) shows the contributions of inelastic scatterings from free electrons and weakly bound electrons to the Compton component. All spectra are calculated with an x-ray probe of 9.0-keV Zn He $_{\alpha}$ , a 130° scattering angle, and a Compton downshifted energy of 260 eV. The Compton down-



E16049JR

Figure 111.54

(a) Calculated total scattered spectra including ion, free-electron, and bound-free components for  $Z_C = 0.75$ ,  $Z_C = 4$ , and  $Z_C = 4.5$ . All spectra are normalized to the larger of either the Rayleigh or Compton peak. (b) Contributions of inelastic scatterings from free electrons and weakly bound electrons to the Compton component for  $Z_C = 0.75$  and  $Z_C = 4.5$ . The  $T_e$  and  $\rho$  are fixed to be 10 eV and 4.96 g/cm<sup>3</sup>.

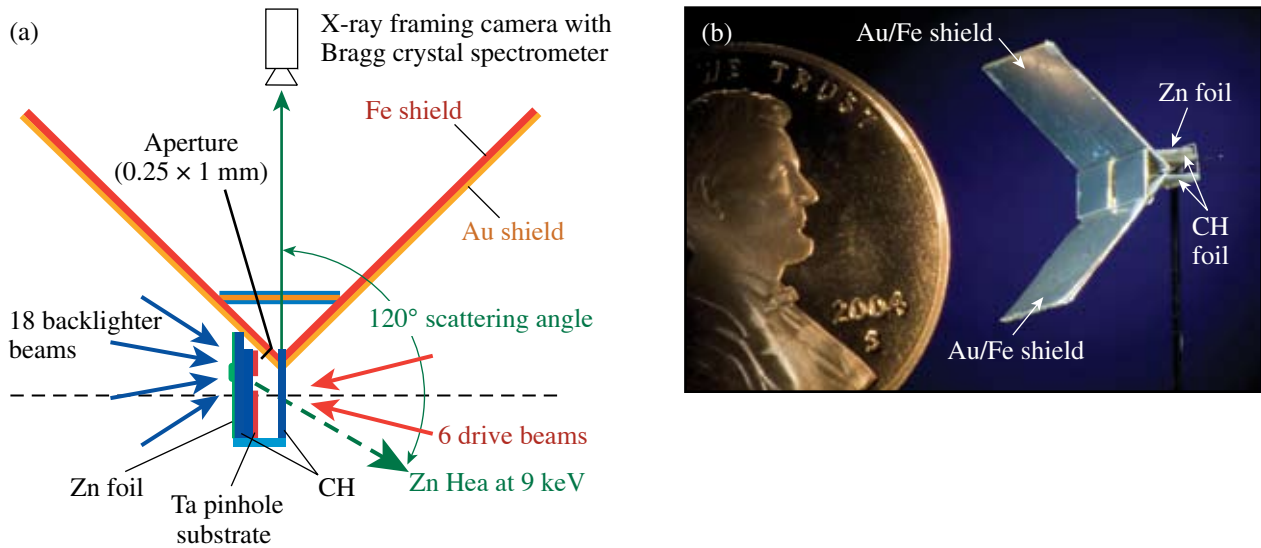
shifted energy is consistent with a 130° scattering angle, which is within the experimental tolerance of the 120° design. The calculated spectra, including all three terms in Eq. (4) for  $Z_C = 0.75$ ,  $Z_C = 4.0$ , and  $Z_C = 4.5$ , are shown in Fig. 111.54(a). In all cases discussed here  $Z_H = 1$  is set. The ratio of the Compton and Rayleigh peaks are comparable for  $Z_C = 0.75$  and  $Z_C = 4.0$ . This is because of the contribution of the scatterings from weakly bound electrons to the Compton component at low  $Z_C$ . Figure 111.54(b) shows that the contributions from the free and weakly bound electrons to the Compton component for  $Z_C =$

0.75 and  $Z_C = 4.5$ , with  $T_e = 10$  eV and  $\rho = 4.96$  g/cm<sup>3</sup>. For  $Z_C = 0.75$ , the contribution of the scattering from weakly bound electrons is slightly higher than that from the free electrons and the total intensity of the Compton peak is comparable to the Rayleigh, as shown in Fig. 111.54(a). As  $Z_C$  is increased, the Compton component is dominated by the scattering from free electrons while the ratio of the two peaks is comparable for  $Z_C = 4$ . Therefore, low ionizations of shocked CH foils (i.e.,  $Z < 2$ ) cannot be accurately diagnosed with this technique. Once a carbon K-shell electron is ionized ( $Z_C > 4$ ), the ratio of the Compton and Rayleigh peak significantly changes for CH, as shown in Fig. 111.54(a).

## Experiment

Spectrally resolved x-ray scattering experiments were performed with 90° and 120° scattering angles. The error in the exact determination of the scattering angle is estimated as  $\pm 10^\circ$ . The experimental configuration for the 120° scattering geometry is shown in Fig. 111.55(a), with a photograph of the target shown in Fig. 111.55(b). The target consists of a large Au/Fe light shield, a Zn backlighter foil, a CH drive foil, and a Ta pinhole substrate. Up to six overlapped beams smoothed with phase plates (SG8)<sup>30</sup> were used to drive a 125- $\mu$ m-thick planar CH target with a uniform intensity in an  $\sim 0.5$ -mm laser spot of  $1 \times 10^{14}$  W/cm<sup>2</sup>. Eighteen additional tightly focused beams ( $\sim 100$ - $\mu$ m spot) irradiated the Zn foil with an overlapped intensity of  $\sim 10^{16}$  W/cm<sup>2</sup> and generated a point-source backlighter of Zn He $_{\alpha}$  emission at 9.0 keV. The 0.5-mm-thick CH foil positioned between the Zn foil and the Ta pinhole substrate blocked x rays with photon energies less than  $\sim 4$  keV with minimal attenuation to the Zn K-shell emission. This prevented the Zn backlighter from radiatively heating the target. The Ta pinhole substrate with a 400- $\mu$ m-diam aperture restricted the backlighter illumination of the CH drive foil to the portion of the target that was uniformly shock heated. The scattering angle was reduced to 90° by adjusting the locations of the aperture and the focal position of the backlighter beams.

Most of the Zn He $_{\alpha}$  emission propagates through the drive foil; however, a small fraction of the x rays are scattered. X rays scattered at 90° or 120° were dispersed with a Bragg crystal spectrometer and recorded with an x-ray framing camera<sup>31</sup> outfitted with a charge-coupled-device (CCD) camera. A highly oriented pyrolytic graphite (HOPG)<sup>32</sup> crystal with a 2d spacing of 6.7 Å was used in the mosaic focusing mode<sup>33</sup> to provide high reflectivity of the scattered x-ray spectrum.<sup>34</sup> The Au/Fe shields reduced the measured background x-ray continuum levels by blocking the direct lines of sight to the Zn and CH coronal plasmas.

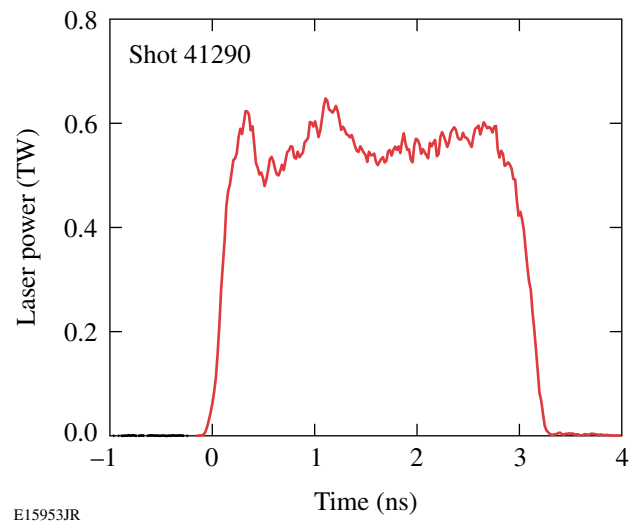


E15952JR

Figure 111.55

(a) Target design of the noncollective spectrally resolved x-ray scattering experiment on OMEGA using a  $120^\circ$  scattering geometry; (b) a photograph of an x-ray scattering target compared in size to a penny.

The strategy of the experiment was to drive a shock wave through the CH foil and to scatter the  $\text{Zn He}_\alpha$  x rays from the uniformly compressed portion of the shock-heated CH around the time that the shock breaks out of the rear side of the target (i.e., the side opposite the laser-irradiated side). Two drive conditions were examined: undriven (i.e., cold, uncompressed CH foil) and an  $\alpha = 3$  drive. The measured time history of the laser power for the  $\alpha = 3$  drive is presented in Fig. 111.56. The plasma conditions of directly driven CH foils were simulated with the 1-D hydrodynamics code *LILAC*. A detailed description of *LILAC* can be found elsewhere<sup>35</sup> with the main features of the code described in this section. Laser absorption is calculated using a ray-trace algorithm that models inverse bremsstrahlung. Transport of radiation is modeled through multigroup diffusion with the Los Alamos National Laboratory Astrophysical Tables<sup>36</sup> or an average ion model providing the opacities. The *SESAME* tables are used to model the equation of state. *LILAC* uses a flux-limited<sup>37</sup> Spitzer–Härm<sup>38</sup> electron thermal-conduction model. This drive is predicted to create a 15-Mbar shock-wave pressure. Figure 111.57 shows the spatial profile of the predicted plasma conditions created with an  $\alpha = 3$  drive around the time the shock breaks out the rear side of the target. A single shock is launched by the  $\alpha = 3$  drive and breaks out the rear side of the target at 2.7 ns. The measurement was made around the shock-breakout time. The plasma conditions in the CH at the time of shock breakout are predicted to be fairly uniform. For the  $\alpha = 3$  drive, the foil is predicted to be heated to  $T_e = 12$  eV with an average ionization



E15953JR

Figure 111.56

The measured laser pulse for the  $\alpha = 3$  drive (shot 41290).

$Z = 0.95$ . As shown in Fig. 111.58, there is little difference in the predicted x-ray scattered spectra from the CH foil targets for undriven and  $\alpha = 3$  drive cases. The plasma condition for an undriven case is  $T_e = 0.1$  eV and  $Z_C = 0.1$ . The ion temperature is predicted to be equal to the electron temperature for all of the drive cases under consideration. The spatially integrated, time-resolved spectra were collected over a 500-ps integration time, which is short compared to the hydrodynamic time scales of the experiment.

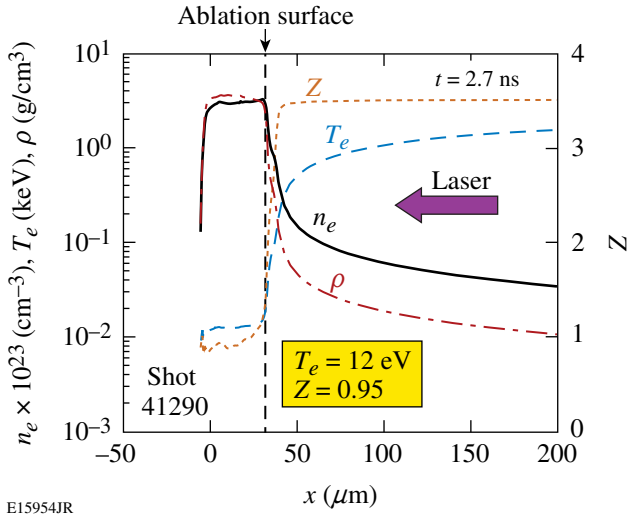


Figure 111.57  
Predictions from the 1-D hydrodynamics code *LILAC* of the spatial profiles of electron temperature ( $T_e$ ), electron density ( $n_e$ ), average ionization ( $Z$ ), and mass density ( $\rho$ ) for laser-irradiated CH foil targets with  $\alpha = 3$  drive.

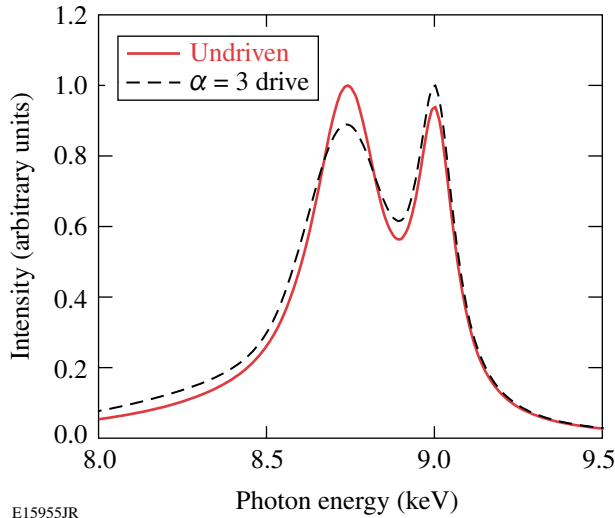


Figure 111.58  
Predicted x-ray scattered spectra for undriven and  $\alpha = 3$  driven CH foils.

The total number of the detected photons per nanosecond,  $N_{\text{det}}$ , was estimated for the x-ray scattering experiment. It is given by

$$N_{\text{det}} = \left( \frac{E_L}{h\nu} \eta_L \frac{1}{\tau_L} \right) \left( \frac{\Omega_{\text{pinhole}}}{4\pi} \right) \eta_{\text{CH}} \times \left[ \frac{n_e \sigma_{T^x}}{(1 + \alpha_{\text{scatter}})^2} \right] \left( \frac{\Omega_{\text{detector}}}{4\pi} R_{\text{crystal}} \eta_d \right), \quad (7)$$

where  $E_L$  is the laser energy,  $\tau_L$  is the laser pulse duration,  $\eta_L$  is the conversion efficiency from the laser energy into the 9.0-keV x rays,  $\eta_{\text{CH}}$  is the attenuation due to 500  $\mu\text{m}$  of CH,  $n_e$  is the electron density,  $x$  is the thickness of the compressed target,  $\Omega_{\text{pinhole}}$  and  $\Omega_{\text{detector}}$  are the solid angles limited by the pinhole diameter and crystal size,  $R_{\text{crystal}}$  is the integrated reflectivity of the crystal, and  $\eta_{\text{CH}}$  is the efficiency inside the detector, including the MCP efficiency and filter transmission. Using  $E_L = 280 \text{ J} \times 18$  beams in the 3-ns pulse,  $h\nu = 9.0 \text{ keV}$ ,  $\eta_L$  is assumed to be  $\sim 0.1\%$ ,  $\Omega_{\text{pinhole}}/4\pi = 0.04$ ,  $\eta_{\text{CH}} = 85\%$ ,  $n_e = 1.5 \times 10^{23} \text{ cm}^{-3}$ ,  $x = 40 \mu\text{m}$  for a shock-compressed target with the  $\alpha = 3$  drive,  $\alpha_{\text{scatter}} = 0.2$  for the  $120^\circ$  scattering geometry,  $\Omega_{\text{detector}}/4\pi = 5.7 \times 10^{-3}$ ,  $R_{\text{crystal}} = 2 \times 10^{-3}$ , and  $\eta_d = 1\%$ . Using Eq. (7),  $N_{\text{det}}$  is estimated to be  $\sim 1500$  photons/ns. Since the integration time was 500 ps and the spectrum was dispersed over the  $\sim 90$  spectrally resolved bins ( $\sim 10 \text{ eV/bin}$ ), the estimated ratio of the signal due to photon statistics is 8.2, which is consistent with the measured signal-to-noise ratio of 8.

## Results and Discussion

X-ray spectra detected at  $90^\circ$  and  $120^\circ$  scattering angles were recorded for an undriven CH foil. Figure 111.59(a) shows the measured spectra from undriven CH foils in  $90^\circ$  and  $120^\circ$  scattering geometries, as well as the signal from a control target whose drive foil has a 1-mm-diam thru-hole in the center of the foil. Figure 111.59(b) shows a microscope image of the control target. The purpose of the control shot was to experimentally confirm that the measured x rays were scattered from the intended target. The lack of signal measured for this shot indicates that x rays are scattering from the intended portion of the nominal drive foil (i.e., without a thru-hole), and scattering from other unintended sources is negligible. The Compton peaks of measured spectra with  $90^\circ$  and  $120^\circ$  scattering angles are consistent with the calculated Compton downshifted energies of  $E_C = \hbar^2 k^2 / 2m_e = 158 \text{ eV}$  and  $238 \text{ eV}$ , respectively. In this article, all of the x-ray scattering measurements from the driven foils were taken with the  $120^\circ$  scattering angle; however, measurements from two different scattering angles would be beneficial to determine the accuracy of the experimentally determined values of  $T_e$  and  $Z_f$ .

The spectra of x rays detected at a  $120^\circ$  scattering angle are presented in Fig. 111.60(a) for the CH targets and in Fig. 111.60(b) for the Br-doped CH targets for the two drive conditions under consideration (i.e., undriven and  $\alpha = 3$  drive). The Br-dopant concentration level in the CH foil was 2% atomic in the bulk of the target, but no Br was in the ablator portion of the target. All of the spectra in Fig. 111.60 are normalized to the larger peak of the Rayleigh or Compton feature. The location

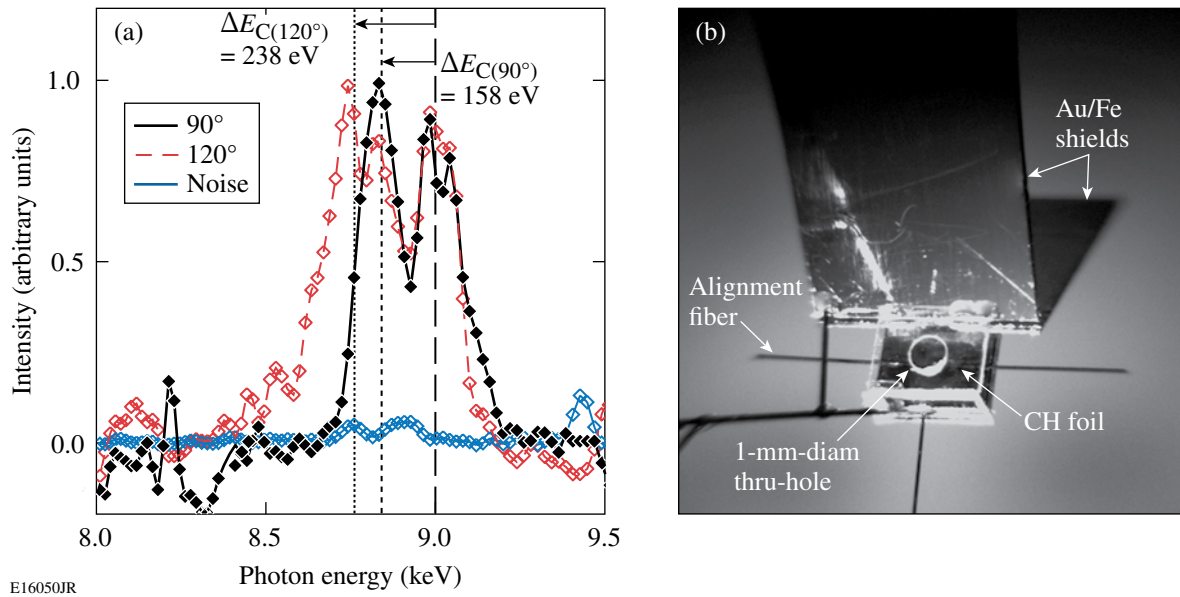


Figure 111.59

(a) Measured x-ray spectra scattered from undriven CH targets with  $90^\circ$  and  $120^\circ$  scattering geometries are compared with the noise level. The dotted and dashed vertical lines show the Compton downshifted energy of 158 eV/238 eV for the  $90^\circ/120^\circ$  scattering angles. (b) A microscope image of the control target with a 1-mm-diam thru-hole in the center of the CH foil.

of line emissions of  $\text{Zn He}_\alpha$  at 9.0 keV and  $\text{Zn Ly}_\alpha$  at 9.3 keV is indicated with vertical dotted lines in the figure. A comparison of the spectra scattered from the CH targets shows little difference between the driven and undriven targets. A detailed analysis of the measured spectra with models is presented in Figs. 111.61(a) and 111.61(b). A similar comparison for the x-ray spectra from the Br-doped CH shows significant changes in the heights of the Compton feature.  $\text{Zn Ly}_\alpha$  line emission contributes to the blue wings of the measured Rayleigh features. For the quantitative analysis, the measured spectra were fit with models to infer  $T_e$  and  $Z_b$  for each ion in the plasma as described in Eq. (6). The modeled spectra were calculated as described in **Spectrally Resolved X-Ray Scattering** (p. 192), and a best fit to the measured spectra was obtained using a least-squares-fitting routine that varied  $T_e$  and the  $Z_b$ 's.

The experimental scattered spectrum from the cold, undriven target is compared with three modeled spectra in Fig. 111.61(a). All of the modeled spectra have solid densities ( $\rho = 1.24 \text{ g/cm}^3$ ) and low electron temperatures ( $T_e = 0.1 \text{ eV}$ ) to indicate that no ionization in CH has occurred, but the  $Z_C$  is varied from 0.1 to 4. The lowest  $Z_C$  agrees with the experimental result as expected in cold CH; however, the models are not very sensitive to  $Z_C$  for  $Z_C < 2$ , suggesting that valence electrons in cold CH could scatter x rays like free electrons. In order to investigate the  $T_e$  sensitivity in the case of driven CH,

$Z_f$  was set to 2.5 (corresponding to  $Z_C = 4$  and  $Z_H = 1$  delocalized electrons) shown in Fig. 111.61(b). As mentioned before, in this case all of the carbon bonds are destroyed and  $Z_f$  does indeed represent the average ionization state in the plasma. In addition to scattering from valence electrons, scattering from the remaining bound electrons into L and K shells must be included, with the respective ionization levels corrected for continuum lowering.<sup>39</sup> In Fig. 111.61(b), the measured spectrum of the CH foil for the  $\alpha = 3$  drive is compared with the modeled spectra for three electron temperatures:  $T_e = 1, 10,$  and  $20 \text{ eV}$  with  $Z_C = 4$ . The mass density used in the models is four times solid density ( $\rho = 4.96 \text{ g/cm}^3$ ), as suggested by *LILAC* simulations. Since the measured spectrum from the driven CH is bounded by the models with  $T_e = 1 \text{ eV}$  and  $T_e = 20 \text{ eV}$ , an upper limit of  $T_e = 20 \text{ eV}$  is inferred for the  $\alpha = 3$  drive. As described in Fig. 111.54(b), the ratios of the Compton and Rayleigh peaks are comparable when  $Z_C < 4$  in a driven CH. Therefore, the inferred  $Z$  in this experiment is an upper limit of  $Z \sim 2$ . The predicted spectra show that the width of the Compton peak is not very sensitive to the electron temperature because  $T_e$  is comparable to the Fermi temperature  $T_F = 16 \text{ eV}$  from the hydro calculation ( $n_e \sim 3 \times 10^{23} \text{ cm}^{-3}$  and  $Z \sim 1$ ). It is also noted that for the compressed case with  $\alpha = 3$ , the electron density is  $n_e \sim 3 \times 10^{23} \text{ cm}^{-3}$ , which lowers the continuum by  $\sim 20 \text{ eV}$  (Ref. 20); thus a fraction of the L-shell electrons should be indeed delocalized.

Trace amounts of Br in the CH foil (i.e., 2% atomic concentration) increase the sensitivity of the spectrally resolved x-ray spectra to changes in the electron temperature. The experimental spectra scattered from CHBr targets are presented in Fig. 111.62 for the two drives under consideration, along with the fitted spectra. A comparison of the scattered x-ray spectra from

the undriven CHBr target [see Fig. 111.62(a)] with the undriven CH target [see Fig. 111.61(a)] reveals that the Br dopant enhances the ratio of the Rayleigh peak to the Compton peak. This is a consequence of the increased number of tightly bound electrons in the CHBr foil. The models for scattered spectra of CHBr foils include the scattering contributions from all ionic species as

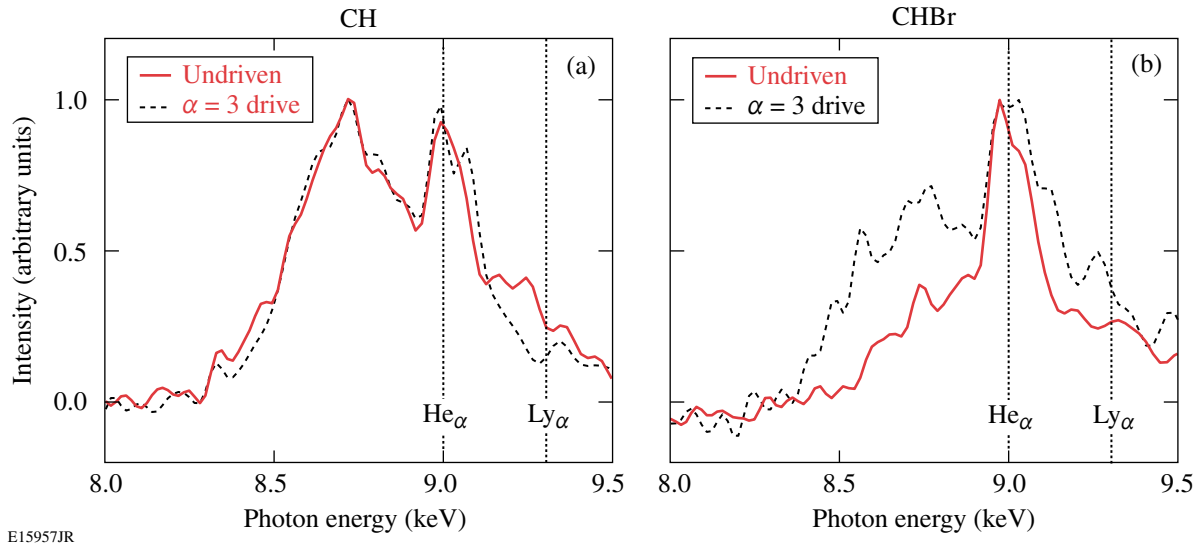


Figure 111.60

(a) Measured x-ray spectra scattered from (a) CH and (b) CHBr targets with the following drive conditions: undriven and  $\alpha = 3$  drive. Spectra are normalized at the Rayleigh peak. The spectral location of Zn  $He_\alpha$  at 9.0 keV and Zn  $Ly_\alpha$  at 9.3 keV is indicated with vertical dotted lines.

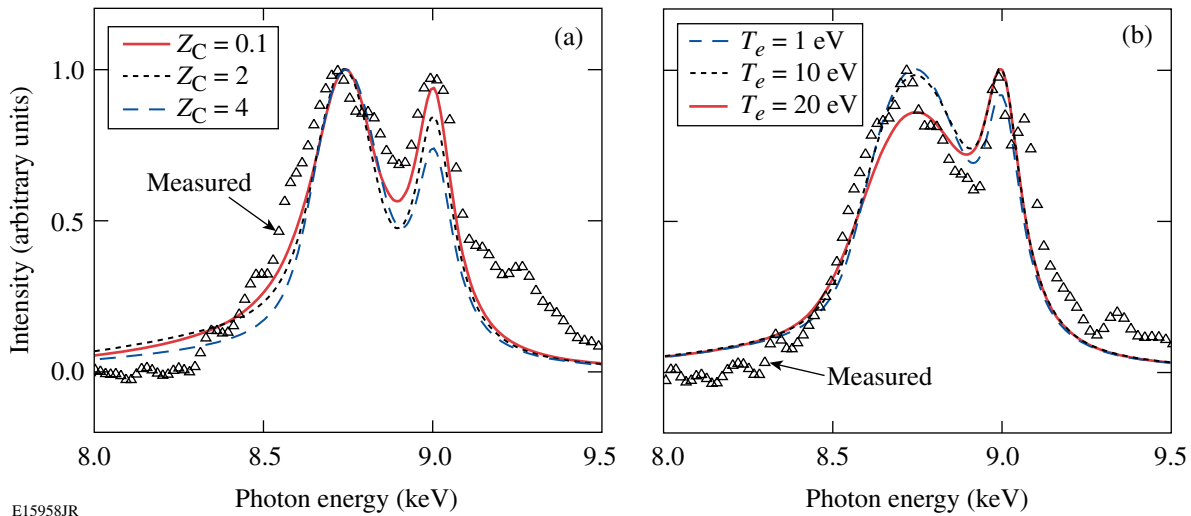
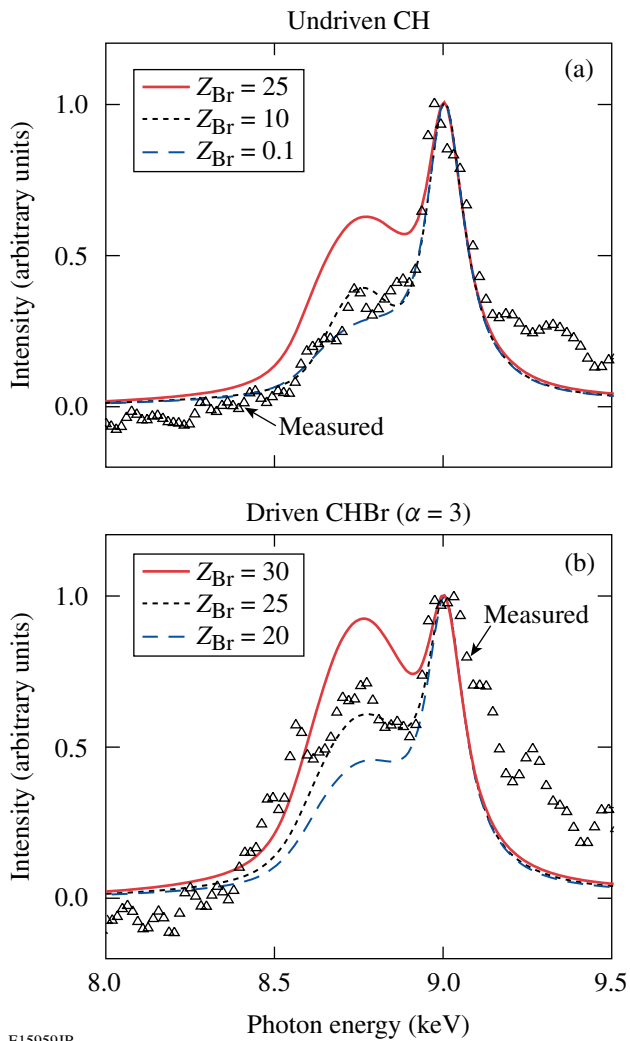


Figure 111.61

(a) Measured spectrum from the undriven CH target compared with modeled spectra for  $Z_C = 0.1$ ,  $Z_C = 2$ , and  $Z_C = 4$  with  $T_e = 0.1$  eV. (b) Measured spectrum for the  $\alpha = 3$  drive compared with modeled spectra of  $T_e = 1, 10,$  and  $20$  eV, and  $Z_C = 4$ .



E15959JR

Figure 111.62

Measured x-ray spectra scattered from CHBr targets for (a) undriven and (b)  $\alpha = 3$  drive are compared with modeled spectra varying  $Z_{\text{Br}}$ . The inferred parameters are  $T_e = 0.1$  eV and  $Z_f = 2.6$  for undriven and  $T_e = 10$  eV and  $Z_f = 2.9$  for the  $\alpha = 3$  drive.  $Z_C = 4$  was set for both undriven and driven cases.

well as their mutual correlations. In addition, the attenuation of the scattered x rays due to the path length in the CHBr foil is included in the modeled scattered spectra. The electron temperatures inferred from the spectral fitting for the undriven and  $\alpha = 3$  drive are  $T_e = 0.1$  eV and  $T_e = 10$  eV, respectively, which are similar to the observations for the pure CH foils. Adding the Br dopant increases the sensitivity of the x-ray scattering to changes in  $Z$ . As shown in Fig. 111.60(b), the height of the Compton feature is increased for the driven target, in contrast to the results with the CH target shown in Fig. 111.60(a). The density is assumed to be solid density for undriven and four

times solid density for  $\alpha = 3$  drive. The undriven case has  $Z_{\text{Br}} = 10$ ,  $Z_C = 4$ , and  $Z_H = 1$ ; the  $\alpha = 3$  drive has  $Z_{\text{Br}} = 25$ ,  $Z_C = 4$ , and  $Z_H = 1$ . The ratio of the Rayleigh peak to the Compton peak is primarily dependent on  $Z_{\text{Br}}$ . It is observed that  $Z_{\text{Br}}$  increases for the driven CHBr foil, while  $Z_C$  is not very sensitive to the  $\alpha = 3$  drive. For the undriven case, little differences are seen between  $Z_{\text{Br}} = 0.1$  and  $Z_{\text{Br}} = 10$ , while  $Z_{\text{Br}}$  needs to be increased close to  $Z_{\text{Br}} = 25$  to match the model to data for the driven case. Since the binding energy of 257 eV for a 3-s M-shell electron of a neutral bromine atom is comparable to the Compton downshifted energy of  $\sim 240$  eV, electrons of a bromine ion in the M and N shell (25 electrons) can be ionized with the Zn He $_{\alpha}$  x rays. Due to the high electron densities in the compressed plasma, continuum lowering is likely to be responsible for the large number of delocalized electrons in bromine. Those electrons belong to extended M and N shells for which electron bonding to the ion core may be heavily screened in the dense plasma. The values of  $Z_f$  inferred from the spectral fitting are  $Z_f = 2.6$  and  $Z_f = 2.9$  for the undriven and  $\alpha = 3$  drive, respectively.

The electron temperatures predicted with *LILAC* for the shocked CH and CHBr targets ( $T_e = 12$  eV) are comparable with the measured results ( $T_e = 10$  to 20 eV) for a drive intensity of  $1 \times 10^{14}$  W/cm $^2$ ; however, an experimental accuracy for  $T_e$  of 10% to 20% is needed to validate the simulations from the hydrodynamics codes. Attempts were made to increase the electron temperature in the direct-drive target by increasing the laser drive intensity to  $\sim 10^{15}$  W/cm $^2$ . However, the x-ray background levels measured for higher drive intensities were found to overwhelm the scattered x-ray spectrum.

### Future Application

The main objective of this research is to develop techniques to probe the plasma conditions in the DT shell of a direct-drive implosion target during the laser irradiation to diagnose the shell adiabat. X-ray scattering is an attractive option for this application since it is noninvasive. The experimental results presented here demonstrate that it is possible to infer the spatially averaged electron temperature of a nearly Fermi-degenerate, direct-drive, shock-heated, and compressed CH foil. The complications arising from the L-shell electrons of carbon associated to a structural phase transition from the solid state to plasma will not be present in the fully ionized hydrogen isotope plasma comprising the shell of the ICF target. Consequently, a straightforward interpretation of the spatially averaged quantities of electron temperature and average ionization in the shell of a DT ICF implosion target is expected from the noncollective x-ray scattering. Predicted x-ray-scattering spectra from

an imploding cryogenic capsule in hohlraum are discussed in Ref. 40. The recent observations of plasmons in warm dense matter<sup>14</sup> show that it is possible to infer the electron density from the collective, forward x-ray scattering. Therefore, a combination of collective and noncollective x-ray scattering should provide the capability to diagnose the spatially averaged quantities of electron density, electron temperature, and the average ionization of a direct-drive DT cryogenic implosion target.

## Conclusion

The electron temperature ( $T_e$ ) and average ionization ( $Z$ ) of nearly Fermi-degenerate, direct-drive, shock-heated, and compressed CH planar foils were investigated for the first time using noncollective spectrally resolved x-ray scattering on the OMEGA Laser System. CH and Br-doped CH foils were driven with six beams, having an overlapped intensity of  $1 \times 10^{14}$  W/cm<sup>2</sup> and generating 15-Mbar pressure in the foil. An examination of the scattered x-ray spectra reveals an upper limit of  $Z \sim 2$ , and  $T_e = 20$  eV is inferred from the spectral line shapes of the elastic Rayleigh and inelastic Compton components. The electron temperatures predicted with *LILAC* ( $T_e = 12$  eV) were found to be comparable with the measured results ( $T_e = 10$  to 20 eV). Low average ionizations (i.e.,  $Z < 2$ ) cannot be accurately diagnosed in this experiment due to the difficulties in distinguishing delocalized valence or free electrons. Trace amounts of Br in the CH foil (i.e., 2% atomic concentration) were shown to increase the sensitivity of the noncollective, spectrally resolved x-ray scattering to changes in the average ionization. A combination of noncollective and collective spectrally resolved x-ray scattering looks like a promising diagnostic technique to probe the spatially averaged plasma conditions in the DT shell of a direct-drive implosion target during the laser irradiation to diagnose the shell adiabat.

## ACKNOWLEDGMENT

The authors are grateful to the LLE Target Fabrication Group, especially Mark Bonino and Dave Turner, for their expertise in constructing the spectrally resolved x-ray scattering targets, as well as Laser Facility Manager Keith Thorp and the OMEGA operations crew for providing the highly reproducible laser performance. This work was supported by the U.S. Department of Energy Office of Inertial Confinement Fusion under Cooperative Agreement No. DE-FC52-92SF19460, the University of Rochester, and the New York State Energy Research and Development Authority. The support of DOE does not constitute an endorsement by DOE of the views expressed in this article.

## REFERENCES

1. J. Nuckolls *et al.*, *Nature* **239**, 139 (1972); J. D. Lindl, R. L. McCrory, and E. M. Campbell, *Phys. Today* **45**, 32 (1992); R. L. McCrory, J. M. Soures, C. P. Verdon, F. J. Marshall, S. A. Letzring, S. Skupsky, T. J. Kessler, R. L. Kremens, J. P. Knauer, H. Kim, J. Delettrez, R. L. Keck, and D. K. Bradley, *Nature* **335**, 225 (1988); R. L. McCrory, S. P. Regan, S. J. Loucks, D. D. Meyerhofer, S. Skupsky, R. Betti, T. R. Boehly, R. S. Craxton, T. J. B. Collins, J. A. Delettrez, D. Edgell, R. Epstein, K. A. Fletcher, C. Freeman, J. A. Frenje, V. Yu. Glebov, V. N. Goncharov, D. R. Harding, I. V. Igumenshchev, R. L. Keck, J. D. Kilkenny, J. P. Knauer, C. K. Li, J. Marciante, J. A. Marozas, F. J. Marshall, A. V. Maximov, P. W. McKenty, J. Myatt, S. Padalino, R. D. Petrasso, P. B. Radha, T. C. Sangster, F. H. Séguin, W. Seka, V. A. Smalyuk, J. M. Soures, C. Stoeckl, B. Yaakobi, and J. D. Zuegel, *Nucl. Fusion* **45**, S283 (2005).
2. P. W. McKenty, V. N. Goncharov, R. P. J. Town, S. Skupsky, R. Betti, and R. L. McCrory, *Phys. Plasmas* **8**, 2315 (2001).
3. P. W. McKenty, T. C. Sangster, M. Alexander, R. Betti, R. S. Craxton, J. A. Delettrez, L. Elasky, R. Epstein, A. Frank, V. Yu. Glebov, V. N. Goncharov, D. R. Harding, S. Jin, J. P. Knauer, R. L. Keck, S. J. Loucks, L. D. Lund, R. L. McCrory, F. J. Marshall, D. D. Meyerhofer, S. P. Regan, P. B. Radha, S. Roberts, W. Seka, S. Skupsky, V. A. Smalyuk, J. M. Soures, K. A. Thorp, M. Wozniak, J. A. Frenje, C. K. Li, R. D. Petrasso, F. H. Séguin, K. A. Fletcher, S. Padalino, C. Freeman, N. Izumi, J. A. Koch, R. A. Lerche, M. J. Moran, T. W. Phillips, G. J. Schmid, and C. Sorce, *Phys. Plasmas* **11**, 2790 (2004).
4. M. C. Herrmann, M. Tabak, and J. D. Lindl, *Phys. Plasmas* **8**, 2296 (2001).
5. R. Betti, K. Anderson, V. N. Goncharov, R. L. McCrory, D. D. Meyerhofer, S. Skupsky, and R. P. J. Town, *Phys. Plasmas* **9**, 2277 (2002).
6. S. P. Regan, J. A. Delettrez, V. N. Goncharov, F. J. Marshall, J. M. Soures, V. A. Smalyuk, P. B. Radha, B. Yaakobi, R. Epstein, V. Yu. Glebov, P. A. Jaanimagi, D. D. Meyerhofer, T. C. Sangster, W. Seka, S. Skupsky, C. Stoeckl, D. A. Haynes, Jr., J. A. Frenje, C. K. Li, R. D. Petrasso, and F. H. Séguin, *Phys. Rev. Lett.* **92**, 185002 (2004).
7. National Research Council (U.S.) Committee on High Energy Density Plasma Physics, *Frontiers in High Energy Density Physics: The X-Games of Contemporary Science* (National Academies Press, Washington, DC, 2003).
8. S. Ichimaru, *Rev. Mod. Phys.* **54**, 1017 (1982).
9. S. H. Glenzer *et al.*, *Phys. Plasmas* **6**, 2117 (1999).
10. S. H. Glenzer *et al.*, *Phys. Rev. Lett.* **90**, 175002 (2003); O. L. Landen *et al.*, *J. Quant. Spectrosc. Radiat. Transf.* **71**, 465 (2001).
11. T. R. Boehly, J. A. Delettrez, J. P. Knauer, D. D. Meyerhofer, B. Yaakobi, R. P. J. Town, and D. Hoarty, *Phys. Rev. Lett.* **87**, 145003 (2001); D. J. Hoarty *et al.*, *J. Quant. Spectrosc. Radiat. Transf.* **99**, 283 (2006).
12. H. Sawada, S. P. Regan, R. Epstein, D. Li, V. Goncharov, P. B. Radha, D. D. Meyerhofer, T. R. Boehly, V. A. Smalyuk, T. C. Sangster, B. Yaakobi, and R. C. Mancini, "Investigation of Direct-Drive Shock-Heating Using X-Ray Absorption Spectroscopy," to be submitted to *Physics of Plasmas*.
13. G. Gregori, S. H. Glenzer, H. K. Chung, D. H. Froula, R. W. Lee, N. B. Meezan, J. D. Moody, C. Niemann, O. L. Landen, B. Holst, R. Redmer, S. P. Regan, and H. Sawada, *J. Quant. Spectrosc. Radiat. Transf.* **99**, 225 (2006).

14. S. H. Glenzer *et al.*, Phys. Rev. Lett. **98**, 065002 (2007).
15. M. W. C. Dharma-wardana and F. Perrot, Phys. Rev. Lett. **84**, 959 (2000).
16. F. Perrot and M. W. C. Dharma-wardana, Phys. Rev. B **62**, 16,536 (2000).
17. J. Sheffield, *Plasma Scattering of Electromagnetic Radiation* (Academic Press, New York, 1975).
18. M. K. Urry *et al.*, J. Quant. Spectrosc. Radiat. Transf. **99**, 636 (2006).
19. G. Gregori, S. H. Glenzer, and O. L. Landen, Phys. Rev. E **74**, 026402 (2006).
20. G. Gregori *et al.*, Phys. Plasmas **11**, 2754 (2004).
21. G. Gregori, S. H. Glenzer, and O. L. Landen, J. Phys. A, Math. Gen. **36**, 5971 (2003).
22. J. Chihara, J. Phys. F, Met. Phys. **17**, 295 (1987).
23. J. Chihara, J. Phys., Condens. Matter **12**, 231 (2000).
24. R. Kubo, J. Phys. Soc. Jpn. **12**, 570 (1957).
25. D. Pines and D. Bohm, Phys. Rev. **85**, 338 (1952).
26. D. Pines and P. Nozieres, *Theory of Quantum Liquids*, Advanced Book Classics (Addison-Wesley, Reading, MA, 1989).
27. P. Nozières and D. Pines, Phys. Rev. **113**, 1254 (1959).
28. M. Schumacher, F. Smend, and I. Borchert, J. Phys. B, At. Mol. Phys. **8**, 1428 (1975).
29. D. Riley *et al.*, Laser Part. Beams **25**, 1 (2007).
30. S. P. Regan, J. A. Marozas, J. H. Kelly, T. R. Boehly, W. R. Donaldson, P. A. Jaanimagi, R. L. Keck, T. J. Kessler, D. D. Meyerhofer, W. Seka, S. Skupsky, and V. A. Smalyuk, J. Opt. Soc. Am. B **17**, 1483 (2000).
31. C. J. Pawley and A. V. Deniz, Rev. Sci. Instrum. **71**, 1286 (2000); R. E. Turner *et al.*, Rev. Sci. Instrum. **72**, 706 (2001).
32. A. Pak *et al.*, Rev. Sci. Instrum. **75**, 3747 (2004).
33. B. Yaakobi and A. J. Burek, IEEE J. Quantum Electron. **QE-19**, 1841 (1983).
34. F. J. Marshall and J. A. Oertel, Rev. Sci. Instrum. **68**, 735 (1997).
35. J. Delettrez, R. Epstein, M. C. Richardson, P. A. Jaanimagi, and B. L. Henke, Phys. Rev. A **36**, 3926 (1987); J. Delettrez, Can. J. Phys. **64**, 932 (1986).
36. W. F. Huebner *et al.*, Los Alamos National Laboratory, Los Alamos, NM, Report LA-6760-M (1977).
37. R. C. Malone, R. L. McCrory, and R. L. Morse, Phys. Rev. Lett. **34**, 721 (1975).
38. L. Spitzer, Jr. and R. Härm, Phys. Rev. **89**, 977 (1953).
39. J. A. Bearden and A. F. Burr, Rev. Mod. Phys. **39**, 125 (1967).
40. A. L. Kritcher *et al.*, High Energy Density Phys. **3**, 156 (2007).



---

# Publications and Conference Presentations

---

## Publications

---

- V. Bagnoud, J. D. Zuegel, N. Forget, and C. Le Blanc, "High-Dynamic-Range Temporal Measurements of Short Pulses Amplified by OPCPA," *Opt. Exp.* **15**, 5504 (2007).
- R. Betti, C. D. Zhou, K. S. Anderson, J. L. Perkins, W. Theobald, and A. A. Solodov, "Shock Ignition of Thermonuclear Fuel with High Areal Density," *Phys. Rev. Lett.* **98**, 155001 (2007).
- P. Brijesh, T. J. Kessler, J. D. Zuegel, and D. D. Meyerhofer, "Demonstration of a Horseshoe-Shaped Longitudinal Focal Profile," *J. Opt. Soc. Am. B* **24**, 1 (2007).
- T. J. B. Collins, J. A. Marozas, R. Betti, D. R. Harding, P. W. McKenty, P. B. Radha, S. Skupsky, V. N. Goncharov, J. P. Knauer, and R. L. McCrory, "One-Megajoule, Wetted-Foam Target-Design Performance for the National Ignition Facility," *Phys. Plasmas* **14**, 056308 (2007) (invited).
- J. E. DeGroot, A. E. Marino, J. P. Wilson, A. L. Bishop, and S. D. Jacobs, "Material Removal Rate Model for Magneto-rheological Finishing (MRF) of Optical Glasses with Nano-diamond MR Fluid," in *Optifab 2007: Technical Digest*, SPIE Technical Digest (SPIE, Bellingham, WA, 2007), Vol. TD04, pp. TF040F.
- C. Dorrer and J. D. Zuegel, "Design and Analysis of Binary Beam Shapers Using Error Diffusion," *J. Opt. Soc. Am. B* **24**, 1268 (2007).
- C. Dorrer and J. D. Zuegel, "Optical Testing Using the Transport-of-Intensity Equation," *Opt. Express* **15**, 7165 (2007).
- D. H. Edgell, R. S. Craxton, L. M. Elasky, D. R. Harding, S. J. Verbridge, M. D. Wittman, and W. Seka, "Three-Dimensional Characterization of Spherical Cryogenic Targets Using Ray-Trace Analysis of Multiple Shadowgraph Views," *Fusion Sci. Technol.* **51**, 717 (2007).
- K. A. Fletcher, B. Apker, S. Hammond, J. Punaro, F. J. Marshall, J. Laine, and R. Forties, "Detection of Charged Particles with Charge Injection Devices," *Rev. Sci. Instrum.* **78**, 063301 (2007).
- G. Gol'tsman, O. Minaeva, A. Korneev, M. Tarkhov, I. Rubstova, A. Divochiy, I. Milostnaya, G. Chulkova, N. Kaurova, B. Voronov, D. Pan, J. Kitaygorsky, A. Cross, A. Pearlman, I. Komissarov, W. Slys, M. Wegrzecki, P. Grabiec, and R. Sobolewski, "Middle-Infrared to Visible-Light Ultrafast Superconducting Single-Photon Detectors," *IEEE Trans. Appl. Supercond.* **17**, 246 (2007).
- W. Guan and J. R. Marciante, "Single-Polarisation, Single-Frequency, 2 cm Ytterbium-Doped Fibre Laser," *Electron. Lett.* **43**, 558 (2007).
- J. Honig, J. Halpin, D. Browning, J. Crane, R. Hackel, M. Henesian, J. Peterson, D. Ravizza, T. Wennberg, H. Rieger, and J. Marciante, "Diode-Pumped Nd:YAG Laser with 38 W Average Power and User-Selectable, Flat-in-Time Subnanosecond Pulses," *Appl. Opt.* **46**, 3269 (2007).
- S. D. Jacobs, "Manipulating Mechanics and Chemistry in Precision Optics Finishing," *Sci. Technol. Adv. Mater.* **8**, 153 (2007).
- A. Jukna, I. Barbov, G. Jung, A. Abrutis, S. S. Banerjee, X. Li, D. Wang, and R. Sobolewski, "Noise Evidence for Intermittent Channeled Vortex Motion in Laser-Processed YBaCuO Thin Films," in *Noise and Fluctuations in Circuits, Devices, and Materials*, edited by M. Macucci, L. K. J. Vandamme, C. Ciofi, and M. B. Weissman (SPIE, Bellingham, WA, 2007), Vol. 6600, pp. 66001C.
- M. Khafizov, X. Li, Y. Cui, X. X. Xi, and R. Sobolewski, "Mechanism of Light Detection in Current-Biased Superconducting MgB<sub>2</sub> Microbridges," *IEEE Trans. Appl. Supercond.* **17**, 2867 (2007).
- J. Kitaygorsky, I. Komissarov, A. Jukna, D. Pan, O. Minaeva, N. Kaurova, A. Divochiy, A. Korneev, M. Tarkhov, B. Voronov, I. Milostnaya, G. Gol'tsman, and R. Sobolewski, "Dark Counts

in Nanostructured NbN Superconducting Single-Photon Detectors and Bridges,” *IEEE Trans. Appl. Supercond.* **17**, 275 (2007).

A. Korneev, O. Minaeva, A. Divochiy, A. Antipov, N. Kaurova, B. Seleznev, B. Voronov, G. Gol’tsman, D. Pan, J. Kitaygorsky, W. Slysz, and R. Sobolewski, “Ultrafast and High Quantum Efficiency Large-Area Superconducting Single-Photon Detectors,” in *Photon Counting Applications, Quantum Optics, and Quantum Cryptography*, edited by I. Prochazka, A. L. Migdall, A. Pauchard, M. Dusek, M. S. Hillery, and W. P. Schleich (SPIE, Bellingham, WA, 2007), Vol. 6583, pp. 65830I.

G. A. Kyrala, D. C. Wilson, J. F. Benage, M. Gunderson, K. Klare, J. Frenje, R. Petrasso, W. Garbett, S. James, V. Glebov, and B. Yaakobi, “Effect of Higher  $z$  Dopants on Implosion Dynamics: X-Ray Spectroscopy,” *High Energy Density Phys.* **3**, 163 (2007).

X. Li, M. Khafizov, Š. Chromik, M. Valerianova, V. Štrbík, P. Odier, and R. Sobolewski, “Ultrafast Photoresponse Dynamics of Current-Biased Hg-Ba-Ca-Cu-O Superconducting Microbridges,” *IEEE Trans. Appl. Supercond.* **17**, 3648 (2007).

R. L. McCrory, “Highlights of the History of the University of Rochester,” in *Inertial Confinement Nuclear Fusion: A Historical Approach by Its Pioneers*, edited by G. Velarde and N. Carpintero-Santamaria (Foxwell & Davies (UK) Ltd., London, 2007), pp. 127–166.

R. L. McCrory, D. D. Meyerhofer, R. Betti, T. R. Boehly, R. S. Craxton, T. J. B. Collins, J. A. Delettrez, R. Epstein, V. Yu. Glebov, V. N. Goncharov, D. R. Harding, R. L. Keck, J. H. Kelly, J. P. Knauer, S. J. Loucks, L. D. Lund, J. A. Marozas, P. W. McKenty, F. J. Marshall, S. F. B. Morse, P. B. Radha, S. P. Regan, S. Roberts, W. Seka, S. Skupsky, V. A. Smalyuk, C. Sorce, C. Stoeckl, J. M. Soures, R. P. J. Town, B. Yaakobi, J. A. Frenje, C. K. Li, R. D. Petrasso, F. H. Séguin, K. Fletcher, S. Padalino, C. Freeman, and T. C. Sangster, “Direct-Drive Inertial Confinement Fusion Research at the Laboratory for Laser Energetics,” in *Current Trends in International Fusion Research—Proceedings of the Fourth Symposium*, edited by C. D. Orth and E. Panarella (NRC Research Press, Ottawa, Canada, 2007), pp. 367–386.

A. V. Okishev, C. Dorrer, V. I. Smirnov, L. B. Glebov, and J. D. Zuegel, “Spectral Filtering in a Diode-Pumped Nd:YLF Regenerative Amplifier Using a Volume Bragg Grating,” *Opt. Express* **15**, 8197 (2007).

D. Pan, W. Donaldson, and R. Sobolewski, “Femtosecond Laser-Pumped Source of Entangled Photons for Quantum Cryptography Applications,” in *Photon Counting Applications, Quantum Optics, and Quantum Cryptography*, edited by M. Dusek, M. S. Hillery, W. P. Schleich, A. L. Migdall, A. Pauchard, and I. Prochazka (SPIE, Bellingham, WA, 2007), Vol. 6583, pp. 65830K.

S. P. Regan, R. Epstein, V. N. Goncharov, I. V. Igumenshchev, D. Li, P. B. Radha, H. Sawada, W. Seka, T. R. Boehly, J. A. Delettrez, O. V. Gotchev, J. P. Knauer, J. A. Marozas, F. J. Marshall, R. L. McCrory, P. W. McKenty, D. D. Meyerhofer, T. C. Sangster, D. Shvarts, S. Skupsky, V. A. Smalyuk, B. Yaakobi, and R. C. Mancini, “Laser-Absorption, Mass Ablation Rate, and Shock Heating in Direct-Drive Inertial Confinement Fusion,” *Phys. Plasmas* **14**, 056305 (2007) (invited).

J. R. Rygg, J. A. Frenje, C. K. Li, F. H. Séguin, R. D. Petrasso, V. Yu. Glebov, D. D. Meyerhofer, T. C. Sangster, and C. Stoeckl, “Time-Dependent Nuclear Measurements of Mix in Inertial Confinement Fusion,” *Phys. Rev. Lett.* **98**, 215002 (2007).

T. C. Sangster, R. Betti, R. S. Craxton, J. A. Delettrez, D. H. Edgell, L. M. Elasky, V. Yu. Glebov, V. N. Goncharov, D. R. Harding, D. Jacobs-Perkins, R. Janezic, R. L. Keck, J. P. Knauer, S. J. Loucks, L. D. Lund, F. J. Marshall, R. L. McCrory, P. W. McKenty, D. D. Meyerhofer, P. B. Radha, S. P. Regan, W. Seka, W. T. Shmayda, S. Skupsky, V. A. Smalyuk, J. M. Soures, C. Stoeckl, B. Yaakobi, J. A. Frenje, C. K. Li, R. D. Petrasso, F. H. Séguin, J. D. Moody, J. A. Atherton, B. D. MacGowan, J. D. Kilkenny, T. P. Bernat, and D. S. Montgomery, “Cryogenic DT and D<sub>2</sub> Targets for Inertial Confinement Fusion,” *Phys. Plasmas* **14**, 058101 (2007) (invited tutorial).

W. Seka, P. Rechmann, J. D. B. Featherstone, and D. Fried, “Laser Ablation of Dental Hard Tissue,” *J. Laser Dent.* **15**, 61 (2007).

S. N. Shafir, J. C. Lambropoulos, and S. D. Jacobs, “Micromechanical Contributions to Material Removal and Surface Finish,” in *Optifab 2007: Technical Digest*, SPIE Technical Digest (SPIE, Bellingham, WA, 2007), Vol. TD04, pp. TF0407.

W. Slysz, M. Wegrzecki, J. Bar, P. Grabiec, M. Gorska, E. Reiger, S. Dorenbos, V. Zwiller, I. Milostnaya, O. Minaeva, A. Antipov, O. Okunev, A. Korneev, K. Smirnov, B. Voronov, N. Kaurova, G. N. Gol’tsman, J. Kitaygorsky, D. Pan, A. Pearlman, A. Cross, I. Komissarov, and R. Sobolewski,

“Fiber-Coupled NbN Superconducting Single-Photon Detectors for Quantum Correlation Measurements,” in *Photon Counting Applications, Quantum Optics, and Quantum Cryptography*, edited by I. Prochazka, A. L. Migdall, A. Pauchard, M. Dusek, M. S. Hillery, and W. P. Schleich (SPIE, Bellingham, WA, 2007), Vol. 6583, pp. 65830J.

A. A. Solodov, R. Betti, J. A. Delettrez, and C. D. Zhou, “Gain Curves and Hydrodynamic Simulations of Ignition and Burn for Direct-Drive Fast-Ignition Fusion Targets,” *Phys. Plasmas* **14**, 062701 (2007).

T. Taneda, G. P. Pepe, L. Parlato, A. A. Golubov, and R. Sobolewski, “Time-Resolved Carrier Dynamics and Electron-Phonon Coupling Strength in Proximized Weak

Ferromagnet/Superconductor Nanobilayers,” *Phys. Rev. B* **75**, 174507 (2007).

D. Wang, A. Cross, G. Guarino, S. Wu, R. Sobolewski, and A. Mycielski, “Time-Resolved Dynamics of Coherent Acoustic Phonons in CdMnTe Diluted-Magnetic Single Crystals,” *Appl. Phys. Lett.* **90**, 211905 (2007).

L. Welser-Sherrill, R. C. Mancini, J. A. Koch, N. Izumi, R. Tommasini, S. W. Haan, D. A. Haynes, I. E. Golovkin, J. A. Delettrez, F. J. Marshall, S. P. Regan, and V. A. Smalyuk, “Development of Spectroscopic Tools for the Determination of Temperature and Density Spatial Profiles in Implosion Cores,” *High Energy Density Phys.* **3**, 287 (2007).

### Forthcoming Publications

A. C.-A. Chen, J. U. Wallace, K. P. Klubek, M. B. Madaras, C. W. Tang, and S. H. Chen, “Effects of Emitter Layer’s Chemical Composition on the Efficiency of Organic Blue Light-Emitting Diodes,” to be published in *Chemistry of Materials*.

C. Dorrer, I. A. Begishev, A. V. Okishev, and J. D. Zuegel, “High-Contrast Ultrafast Optical Parametric Amplifier as a Front End of High-Power Laser Systems,” to be published in *Optics Letters*.

C. Dorrer, A. V. Okishev, I. A. Begishev, J. D. Zuegel, V. I. Smirnov, and L. B. Glebov, “Optical Parametric Chirped-Pulse-Amplification Contrast Enhancement by Regenerative Pump Spectral Filtering,” to be published in *Optics Letters*.

V. N. Goncharov, “Ablative Richtmyer–Meshkov Instability: Theory and Experimental Results,” to be published in the *Proceedings of Scottish Summer School*.

V. N. Goncharov, “Direct-Drive Inertial Fusion: Basic Concepts and Ignition Target Designing,” to be published in the *Proceedings of Scottish Summer School*.

H. Huang and T. Kessler, “Tiled-Grating Compressor with Uncompensated Dispersion for Near-Field-Intensity Smoothing,” to be published in *Optics Letters*.

I. V. Igumenshchev, V. N. Goncharov, W. Seka, D. H. Edgell, and T. R. Boehly, “The Effect of Resonance Absorption in

OMEGA Direct-Drive Designs and Experiments,” to be published in *Physics of Plasmas*.

I. Kang and C. Dorrer, “Method of Optical Pulse Characterization Using Sinusoidal Optical Phase Modulations,” to be published in *Optics Letters*.

J. R. Marciante, W. R. Donaldson, and R. G. Roides, “Averaging of Replicated Pulses for Enhanced Dynamic Range, Single-Shot Measurement of Nanosecond Optical Pulses,” to be published in *IEEE Photonics Technology Letters*.

J. Qiao, A. Kalb, M. J. Guardalben, G. King, D. Canning, R. Jungquist, and J. H. Kelly, “Large-Aperture Grating Tiling by Interferometry for Chirped-Pulse–Amplification Systems,” to be published in *Optics Express*.

E. Reiger, S. Dorenbos, V. Zwiller, A. Korneev, G. Chulkova, I. Milostnaya, O. Minaeva, G. Gol’tsman, W. Słysz, J. Kitaygorsky, D. Pan, A. Jukna, and R. Sobolewski, “Spectroscopy with Nanostructured Superconducting Single-Photon Sources,” to be published in *IEEE Journal of Selected Topics of Quantum Electronics*.

T. C. Sangster, R. L. McCrory, V. N. Goncharov, D. R. Harding, S. J. Loucks, P. W. McKenty, D. D. Meyerhofer, S. Skupsky, B. A. Hammel, J. D. Lindl, E. Moses, J. Atherton, G. B. Logan, S. Yu, J. D. Kilkenny, A. Nikroo, H. Wilken, K. Matzen, R. Leeper, R. Olsen, J. Porter, C. Barnes, J. C. Fernandez, D. Wilson, J. D. Sethian, and S. Obenschain, “Overview of

Inertial Fusion Research in the United States,” to be published in Nuclear Fusion.

S. N. Shafir, J. C. Lambropoulos, and S. D. Jacobs, “Subsurface Damage and Microstructure Development in Precision Microground Hard Ceramics Using Magnetorheological Finish ing Spots,” to be published in Applied Optics.

S. N. Shafir, J. C. Lambropoulos, and S. D. Jacobs, “Technical Note: Toward Magnetorheological Finishing of Magnetic Materials,” to be published in the Journal of Manufacturing Science and Engineering.

A. Simon, “Comment on ‘Magnetic Field Effects on Gas Discharge Plasmas’ [Phys. Plasmas **13**, 163511 (2006)],” to be published in Physics of Plasmas.

L. Sun and J. R. Marciante, “Filamentation Analysis in Large-Mode-Area Fiber Lasers,” to be published in the Journal of the Optical Society of America B.

S. Wu, P. Geiser, J. Jun, J. Karpinski, and R. Sobolewski, “Femtosecond Optical Generation and Detection of Coherent Acoustic Phonons in GaN Single Crystals,” to be published in Physical Review B.

C. D. Zhou and R. Betti, “Hydrodynamic Relations for Direct-Drive Fast-Ignition and Conventional Inertial Confinement Fusion Implosions,” to be published in Physics of Plasmas.

---

### Conferences Presentations

---

The following presentations were made at SPIE Europe: Optics and Optoelectronics, Prague, Czech Republic, 16–19 April 2007:

D. Pan, W. R. Donaldson, and R. Sobolewski, “Femtosecond Laser-Pumped Source of Entangled Photons for Quantum Cryptography Applications.”

R. Sobolewski, “Fiber-Coupled NbN Superconducting Single-Photon Detectors for Quantum Correlation Measurements.”

---

The following presentations were made at CLEO/QELS 2007, Baltimore, MD, 6–11 May 2007:

P. Brijesh, T. J. Kessler, J. D. Zuegel, and D. D. Meyerhofer, “Spatially Shaping the Longitudinal Focal Distribution into a Horseshoe-Shaped Profile.”

W. R. Donaldson, D. N. Maywar, and J. H. Kelly, “Measurement of the Self-Phase-Modulation-Induced Bandwidth in a 30-kJ-Class Laser-Amplifier System.”

C. Dorrer, “Pulse Shaping Using Binary Sequences Designed with Error Diffusion.”

C. Dorrer and J. D. Zuegel, “Characterization of High-Frequency Surface Modulation Using the Transport-of-Intensity Equation.”

J. R. Marciante, “Effectiveness of Radial Index Tailoring in Large-Mode-Area Fiber Lasers and Amplifiers.”

J. R. Marciante, “Gain Filtering for Single-Spatial-Mode Operation of Large-Mode-Area Fiber Amplifiers.”

J. Qiao, D. Canning, G. King, M. J. Guardalben, J. Price, A. Kalb, R. Jungquist, A. L. Rigatti, and J. H. Kelly, “Interferometric Tiling for Large-Aperture Gratings for Petawatt Laser Systems.”

---

The following presentations were made at Optifab 2007, Rochester, NY, 14–17 May 2007:

J. E. DeGroot, A. E. Marino, J. P. Wilson, A. L. Bishop, and S. D. Jacobs, “Material Removal Rate Model for Magnetorheological Finishing (MRF) of Optical Glasses with Nanodiamond MR Fluid.”

S. N. Shafir, J. C. Lambropoulos, and S. D. Jacobs, "Surface Finish and Subsurface Damage in Polycrystalline Optical Materials."

K. L. Marshall, K. Hasman, M. Leitch, G. Cox, T. Z. Kosci, A. Trajkovska-Petkoska, and S. D. Jacobs, "Doped Multi-layer Polymer Cholesteric-Liquid-Crystal (PCLC) Flakes: A Novel Electro-Optical Medium for Highly Reflective Color Flexible Displays," SID 2007 Symposium, Long Beach, CA, 20–25 May 2007.

K. L. Marshall, V. Rapson, Y. Zhang, G. Mitchell, and A. L. Rigatti, "Contaminant Resistant Sol-Gel Coatings for High Peak Power Laser Applications," Optical Interference Coatings (OSA-OIC), Tucson, AZ, 3–8 June 2007.

S. G. Lukishova, L. J. Bissell, S. K. H. Wei, A. W. Schmid, Z. Shi, H. Shin, R. Knox, P. Freivald, R. W. Boyd, C. R. Stroud, Jr., S.-H. Chen, and K. L. Marshall, "Room-Temperature Single Photon Sources with Fluorescent Emitters in Liquid Crystal Hosts," International Conference on Quantum Information, Rochester, NY, 13–15 June 2007.

The following presentations were made at the 15th APS Topical Conference on Shock Compression of Condensed Matter, Fairmont Orchard, HI, 24–29 June 2007:

T. R. Boehly, J. E. Miller, J. H. Eggert, D. G. Hicks, P. M. Celliers, D. D. Meyerhofer, and G. W. Collins, "Measurements of the Release of Alpha Quartz: A New Standard for Impedance-Match Experiments."

S. Brygoo, J. H. Eggert, P. Loubeyre, R. S. McWilliams, D. G. Hicks, P. M. Celliers, T. R. Boehly, R. Jeanloz, and G. W. Collins, "The Equation of State and Optical Conductivity of Warm Dense He and H<sub>2</sub>."

J. Eggert, D. Bradley, P. Celliers, G. Collins, D. Hicks, D. Braun, S. Prisbey, R. Smith, and T. Boehly, "Ramp Compression of Diamond to Over 1000 GPa."

D. Hicks, J. Eggert, P. Celliers, H.-S. Park, S. LePape, P. Patel, B. Maddox, G. Collins, T. Boehly, and B. Barbreil, "Measurement of Shock Wave Density Using Quantitative X-Ray Phase Contrast Imaging."

J. E. Miller, T. R. Boehly, D. D. Meyerhofer, J. H. Eggert, S. C. Wilks, J. H. Satcher, and J. F. Poco, "Equation-of-State Measurements in Ta<sub>2</sub>O<sub>5</sub> Aerogel."

The following presentations were made at the ITER-LMJ-NIF International Workshop, Cadarache, France, 27–29 June 2007:

V. Yu. Glebov, T. C. Sangster, C. Stoeckl, S. Roberts, M. Cruz, C. Mileham, M. J. Moran, R. A. Lerche, J. M. Mack, H. Herrmann, C. S. Young, J. L. Bourgade, O. Landreas, J. Raimbourg, G. A. Chandler, and K. Miller, "Environmental Challenges for the Nuclear Diagnostics on the NIF and LMJ."

W. T. Shmayda, "Tritium Management on OMEGA."

